

# NOVEL WALL DEFECTS IN LAMELLAR SOFT MATTER

Chowkampally Saichand

A thesis submitted to the Jawaharlal Nehru University  
for the degree of  
**Doctor of Philosophy**  
2022



Raman Research Institute  
Bengaluru 560080  
India



# Declaration

I, Chowkampally Saichand, declare that this thesis titled, “**NOVEL WALL DEFECTS IN LAMELLAR SOFT MATTER**”, is composed independently by me at Raman Research Institute, Bangalore, India, under the supervision of Prof. Arun Roy and Prof. Yashodhan Hatwalne except where due acknowledgement have been made. I further declared that it has not been previously included in a thesis, dissertation, or report submitted to this University or to any other institution for a degree, diploma or other qualifications. I also declare that I have run it through the **Turnitin** plagiarism software.

---

Prof. Arun Roy  
(Thesis Supervisor)

---

Chowkampally Saichand

---

Prof. Yashodhan Hatwalne  
(Thesis Co-supervisor)



# Certificate

This is to certify that the thesis entitled “**NOVEL WALL DEFECTS IN LAMELLAR SOFT MATTER**” submitted by Chowkampally Saichand for the award of the degree of DOCTOR OF PHILOSOPHY of Jawaharlal Nehru University is his original work. This has not been published or submitted to any other University for any other degree or diploma.

---

Prof. Tarun Souradeep

Director

Raman Research Institute

---

Prof. Arun Roy

(Thesis Supervisor)

---

Prof. Yashodhan Hatwalne

(Thesis Co-supervisor)



Dedicated to my parents and teachers



# Abstract

Two-dimensional soft materials such as flexible membranes offer an ideal testing ground for fundamental concepts involving order (symmetry), low-energy excitations, topological defects, and fluctuations. This thesis studies the interplay between geometry, topology, and elasticity in two-dimensional soft materials. Gaussian (intrinsic) curvature of membranes acts as a source of topological defects in orientational order [1, 2]. Conversely, topological defects tend to bend flat, deformable ordered membranes to reduce in-plane stresses. Positive and negative disclinations (vortices) prefer locally positive and negative Gaussian curvatures respectively. The interplay between Gaussian curvature and topological defects is strikingly illustrated by the Poincaré-Hopf index theorem. According to this theorem, a sphere with in-plane orientational order must have an isolated disclination or isolated disclinations with total index 2.

This thesis is structured as follows. In the first chapter we present a brief review of the elasticity theory of orientationally ordered fluid membranes, and the topology of disclinations in such membranes. This is followed by a brief discussion of the phenomenology of polymer crystallisation. The rest of the thesis is separated into two parts. In the first part (Chapters 2, 3, 4) we address the stability of singular, topological wall defects on spheres, catenoids, and helicoids. In the second part (Chapters 5, 6) we discuss the role of topological defects in determining the observed morphologies of polymer crystallites. The work presented in these parts is summarised below.

## **Part-I: Stability of singular, topological wall disclinations on curved membranes.**

In chapter 2, we study the topological, singular wall defects (of total index 2) on orientationally ordered spherical vesicles. Unlike soliton-type wall configurations, these wall defects are singular lines. However, wall defects are topologically unstable on two-dimensional surfaces [3]. Within the mean-field approximation, we show that singular, topological wall defects can be stabilized on a sphere because

of its Gaussian (intrinsic) curvature and not because of boundary conditions, externally imposed fields, or divergences in certain elastic constants. They are stable close to the order-disorder transition, over a finite range of a dimensionless parameter  $\eta$ . The parameter  $\eta$  is the ratio of basic free energy scales corresponding to the destruction of order in the defect cores to that of the elastic deformation outside the core. We attribute their stability to free-energetic considerations, which override those of topological stability. Remarkably, we find that for  $n$ -atic order, the lowest *elastic free-energy* configuration has  $2n$  walls of index  $1/n$  each, located such that the integral of Gaussian curvature of the sphere between any two successive walls is  $2\pi/n$  (division of Gaussian curvature).

We also study the stability of wall disclinations on catenoidal and helicoidal surfaces, which are negative Gaussian curvature surfaces. They are minimal surfaces that are isometric to each other; one can bend a catenoid into a portion of a helicoid without stretching. Although these surfaces are not subject to the Poincaré-Hopf theorem, we find that the ground state configuration possesses disclinations with total index  $-2$ . Similar to spherical membranes, wall disclinations (of total index  $-2$ ) on catenoids and helicoids are stable near the orientational order-disorder transition over a finite range of  $\eta$ . Chapter 3 focuses on point and wall disclinations and their interactions on catenoidal membranes of infinite extent (finite neck radius and infinite height). Furthermore, we investigate finite height effects on the stability of wall disclinations. We predict transitions between different defect configurations to defect-free configurations as a function of  $\eta$ . In Chapter 4, we discuss the isometric transformation between helicoid and catenoid. Using this transformation, we show that results for catenoidal membranes are easily mapped to helicoidal membranes. Thus, the results such as stability of wall disclinations, energetic of points, wall disclinations, and division of Gaussian curvature by the walls on the catenoid are applicable to the helicoid.

## **Part-II: Sector-, and tent morphologies of polymer crystallites.**

Polymer crystals (solution-grown, as well as melt-grown) are significantly different from atomic and molecular crystals because of their connectivity. This

is because polymers have long, interpenetrating chains. Interestingly, observed morphologies of polymer crystallites are lamellar. These display spherulitic, sectored, tent-like, or scroll structures. Microscopic formation of lamellae is well explained by the adjacent re-entry model — parts of polymer chains form rigid stem-like structures attached to adjacent stems by folds in the polymer chains [4]. These stems offer crystalline order by arranging on a lattice. Depending on growth conditions stems can align either along the lamellar normal, or at an angle with respect to it. Even though macroscopic structures such as tents are observed experimentally, there is no clear, theoretical understanding of their stability. In our work, we use concepts borrowed from liquid-crystal physics, and the physics of crystalline membranes to study the sector-, and especially the tent morphologies. To our knowledge, this is the first attempt at a detailed theoretical modelling that addresses the stability of the tent morphology.

In chapter 5, we briefly review the model discussed in [5], *and present an improved calculation to study the range of stability of the sector morphology*. The sectored morphology has intersecting wall defects (“solitons”) in the fold-field, with a disclination at the point of intersection of the walls (at the centre of the sector). Strong anisotropy in line tension entraps a disclination, and stabilises the sector morphology. Chapter 6 focuses on the stability of the tent morphology. We show that tents are buckled sectors. Bucking involves the bending of polymer lamellae. We discuss two possible modes by which polymer lamellae can bend. We construct “phase diagrams” in parameter space, indicating the ranges of stability of the sector- and tent configurations over a range of dimensionless, phenomenological parameters involving bending rigidity, and (isotropic-, and anisotropic) line tensions of polymer lamellae.

---

Prof. Arun Roy  
(Thesis Supervisor)

---

Chowkampally Saichand

---

Prof. Yashodhan Hatwalne  
(Thesis Co-supervisor)



# Acknowledgements

My PhD life in RRI has been a challenging but rewarding experience. It would not have been possible without the help of many people.

First, I express my sincere gratitude to my thesis supervisors, Prof. Yashodhan Hatwalne and Prof. Arun Roy, for their guidance and constant support in completing this thesis. I am fascinated by Yashodhan's immense knowledge, profound insight into the problems he works on and critical thinking. I thank him for trusting me and sharing his ideas and experience with me. I am also grateful to Arun for his advice and help in taking care of my thesis. Their encouragement and freedom for letting me work independently made this PhD experience fun and exciting.

I am grateful to Prof. Muthukumar for the excellent problem on the sector and tent morphologies of polymer crystals, which is a part of this thesis. I thank Prof. Raghunathan V A for his helpful discussions on the experimental aspects of my thesis problems. His suggestions in my advisory committee meetings are valuable in shaping this thesis. Also, I thank Prof. Andal Narayanan for being a part of my advisory committee and helping in the progress of this thesis. I thank other SCM faculty members for the coursework that taught me liquid crystal physics.

My academic activities wouldn't have been possible without the following people. I thank the RRI admin, the SAAC, Mrs Radha, and Mrs Vidya. Thanks to the SCM secretaries, Mr K Radhakrishna, Mrs Amudha and Mrs Chaithanya. Special thanks to Mrs Chaithanya, who helped me in my Paris visit and thesis submission process. I thank Mr Raja and Mr Murali for their help. The RRI library is one of the best libraries I have come across. I thank the library staff for their excellent services. Manju bro, you are a fantastic library staff to have. I thank the hostel staff, sports committee, canteen, and E&B for providing a beautiful and friendly environment.

I have beautiful moments with my friends in RRI. I thank Jaya Kumar, who is not just a friend but also my senior. He is a great friend to discuss any topic at any time. I have learnt a lot from the interactions with him. I thank Deepshika, Subhadip, Deepak, Vishnu and Swarnak for the lab discussions. My stay at RRI was a breeze, thanks to Adwaith, Arsalan, Bhagya, Nancy, Nishant,

Shilpa and Siva. I cherish our friendship and the fantastic time spent on academic and non-academic activities. Our discussions and arguments made me see things differently. Thanks to Swamy, Jaggu, Surya, Mari, Niranjana, Sreeja, Sumanth, Shikha, Tripti and Sapna Niranjana for the weekend trips, coffee, dinner, and movie sessions. I have been fortunate to have all your support. Sports at RRI used to be my refreshment activities in the evenings. I got opportunities to improve my skills in badminton, volleyball and cricket. Thanks to Anindya, Sreyas, Subodh, Ashutosh, Sharath, and Yateendran for their time at sports. Yateendran. It is my pleasure to have met you all.

Huge thanks to my sister Chandana, my mama and grandpa, my cousins Rajesh and Prasanna, and my fiancée Vijaya. Your kindness and constant support have given me the courage to go further.

Last but not least, thanks to my parents. None of this would have been possible without you. You always believed in me and stood by me when I needed you the most. To Amma and Appa, thanks a lot.

# Contents

<b>Declaration</b>	<b>i</b>
<b>Certificate</b>	<b>iii</b>
<b>Abstract</b>	<b>vii</b>
<b>Acknowledgements</b>	<b>xi</b>
<b>List of Figures</b>	<b>xvii</b>
<b>List of Algorithms</b>	<b>xxvi</b>
<b>1 Introduction</b>	<b>1</b>
1.1 Soft matter . . . . .	1
1.2 Order and Topological defects . . . . .	2
1.3 Curvature of a membrane . . . . .	6
1.4 Interplay between shape, order and topological defects . . . . .	8
1.5 Energetics and Euler-Lagrange equations of fluid membranes with in-plane order . . . . .	9
1.5.1 Frank free energy $F_\alpha$ . . . . .	11
1.5.2 Euler-Lagrange equations . . . . .	13
<b>I Stability of singular, topological wall disclinations on curved membranes</b>	<b>17</b>
<b>2 Wall disclinations on spheres</b>	<b>19</b>
2.1 Introduction . . . . .	19
2.2 Ginzburg-Landau theory . . . . .	21
2.2.1 Equations of equilibrium . . . . .	21

2.3	The elastic free energy . . . . .	23
2.3.1	The Coulomb gas model . . . . .	23
2.4	Vector order . . . . .	24
2.4.1	Antipodal configuration . . . . .	25
2.4.2	Equatorial wall disclination . . . . .	27
2.4.3	Two wall disclinations . . . . .	31
2.5	Nematic order . . . . .	34
2.5.1	Tetrahedral configuration . . . . .	34
2.5.2	The four wall configuration . . . . .	35
2.6	$n$ -atic order: Division of Gaussian curvature by wall defects . . .	37
2.7	Instability of a circular planar wall disclination . . . . .	39
2.8	Discussion and conclusions . . . . .	42
<b>3</b>	<b>Point- and wall disclinations on catenoids</b>	<b>45</b>
3.1	Introduction . . . . .	45
3.2	Vector order . . . . .	46
3.2.1	Disclination-free configuration . . . . .	46
3.2.2	Point disclinations . . . . .	47
3.2.3	Wall disclinations . . . . .	49
3.3	Nematic order . . . . .	56
3.3.1	Four point disclinations . . . . .	56
3.3.2	Four-wall configuration . . . . .	58
3.4	Point disclinations in tetratic- and hexatic order . . . . .	59
3.5	$n$ -atic order: Division of total Gaussian curvature by wall disclinations . . . . .	61
3.6	Finite sized catenoid . . . . .	63
3.7	Results and discussion . . . . .	64
<b>4</b>	<b>Point- and wall disclinations on Helicoids</b>	<b>65</b>
4.1	Introduction . . . . .	65
4.2	Point disclinations . . . . .	65
4.3	Wall disclinations . . . . .	69
4.4	Stability analysis of point- and wall disclinations . . . . .	71

<b>II</b>	<b>Sector-, and tent morphologies of polymer crystallites</b>	<b>75</b>
<b>5</b>	<b>The sector morphology of polymer crystallites</b>	<b>77</b>
5.1	Introduction . . . . .	77
5.2	Experimental observations of polymer single crystallites . . . . .	79
5.3	A model for the sector morphology . . . . .	81
5.3.1	Crystalline order: Hookian elasticity . . . . .	83
5.3.2	Tilt order of the stems . . . . .	83
5.3.3	Fold field . . . . .	84
5.3.4	Surface- and line tension energies . . . . .	86
5.4	Equilibrium equation: An exact solution . . . . .	87
5.5	Energetics . . . . .	89
5.6	Stability analysis: <i>A phase diagram</i> . . . . .	91
5.7	Results and discussion . . . . .	92
<b>6</b>	<b>Tent morphology of polymer crystallites</b>	<b>95</b>
6.1	Introduction . . . . .	95
6.2	The model . . . . .	96
6.3	Equilibrium equations . . . . .	99
6.4	Tent surface as an ansatz for shape equation . . . . .	100
6.5	Energetics . . . . .	102
6.6	Phase diagram of tent, sector and uniform configurations . . . . .	104
6.7	Results and discussion . . . . .	106
<b>A</b>	<b>Isothermal coordinates</b>	<b>109</b>
A.1	Isothermal coordinates . . . . .	109
A.1.1	Stereographic Projection of a sphere . . . . .	110
A.2	Green's function for sphere . . . . .	112
A.3	Magnitude of order parameter . . . . .	112
<b>B</b>	<b>Catenoid and helicoid isometry</b>	<b>115</b>
B.1	Isothermal coordinates on catenoid and helicoid . . . . .	115
B.2	Division of total Gaussian curvature . . . . .	116
B.3	Helicoid : Isomorphism to catenoid . . . . .	117
	<b>Bibliography</b>	<b>119</b>



# List of Figures

1.1	Schematics of in-plane orientational orders. (a) Vector order ( $n = 1$ ) (b) Nematic order ( $n = 2$ ): The nematic phase is a liquid crystalline phase with head-tail symmetry consisting of anisotropic molecules with no positional ordering. It has orientational (two-fold) order and breaks the rotational symmetry of the fluid phase. (See the Sec. 1.2 ) . . . . .	2
1.2	Topological defects in vector order: Dots in the figures represent the core regions. The black curve in (a) is an anti-clock wise contour to characterise the defect. . . . .	3
1.3	Topological defects in nematic order: . . . . .	4
1.4	Crystal defects in two-dimensional hexagonal lattice: The coordination number for hexagonal lattice is is 6. (a) Positive disclination: Five-fold (black dot) coordination number and angle deficit $\omega = 2\pi/6$ . Black curve indicates the counter-clock wise loop L. (b) Negative disclination: Seven-fold (black dot) coordination number and $\omega = -2\pi/6$ . Here the negative sign indicates that a wedge with angle $\omega$ is added at the core. (c) Dislocations are pairs of positive (black dot) and negative (red dot) disclinations. The white arrow represents the Burgers vector (See the text). . . . .	5
1.5	A 2-dimensional surface in 3-dimensions: Vectors $\mathbf{t}_1$ , $\mathbf{t}_2$ and $\mathbf{N}$ are tangents and normal to the surface of parametrisation as $\mathbf{R}(x^1, x^2)$ . . . . .	7

1.6 Curvature of a surface: The surface normal ( $\mathbf{N}$ ) points upward. Two black-curves in the figures represent the principal radii (corresponding principal curvatures  $\kappa_1, \kappa_2$ ) at the point of intersection. (a) Upper hemisphere: Following the convention (see text), we get  $\kappa_1 < 0$  and  $\kappa_2 < 0$ . Thus mean curvature  $H < 0$  and Gaussian curvature  $K > 0$ . (b) Lower hemisphere: Here  $\kappa_1 > 0$  and  $\kappa_2 > 0$ . Therefore  $H > 0$ ;  $K > 0$ . (c) Saddle: For this surface,  $\kappa_1 < 0$ ;  $\kappa_2 > 0$ . Saddle is a minimal surface i.e.,  $\kappa_2 = -\kappa_1$  so that  $H = 0$  and  $K < 0$ . . . . . 7

1.7 Ground state configurations of in-plane orientational order on spheres containing point defects: The images in upper row show the equilibrium positions of point defects in vector-, nematic-order and hexagonal lattice, and lower row depicts the corresponding textures. (a) Antipodal configuration for vector order. Two point disclination of index  $s = 1$  placed at north and south poles. (b) For nematic order, equilibrium position of four  $+1/2$  disclinations are vertices of tetrahedron inscribed in a sphere. (c) In hexatic order and also in hexagonal lattice, the ground state has 12 positive disclinations (five-folded coordination number) located on the vertices of icosahedron inscribed in a sphere. The color images shows the equilibrium configuration of hexagonal lattice on a sphere. . . . . 9

1.8 Schematics of buckling phenomenon of flexible membranes in presence of topological defects: Positive disclinations in vector order (sub fig.(a) ) and hexagonal lattice (sub fig.(c) ) buckle to conical shape whose Gaussian curvature is positive. Similarly, negative defects acquire shapes that have negative Gaussian curvature (sub Figs.(d) and (d) ). . . . . 10

1.9 Orthonormal frame: (a) For a flat membrane, the angle  $\alpha$  is measured with respect to the  $\hat{\mathbf{x}}$ -axis (fixed orthonormal frame). (b) On curved membrane,  $\alpha$  is measured with respect to the orthonormal  $\hat{\mathbf{e}}$ - basis. The tips of the basis vectors can lie anywhere on the unit circle in the tangent plane, implying  $O2$  symmetry. . . . . 12

- 2.1 Vectorial order- Point disclinations: (a) Single point disclination of index  $s = 2$ . (b) Antipodal configuration-Two point disclinations, each of index  $s = 1$  at the poles. . . . . 25
- 2.2 Optimised core sizes: The symbols ap, and tp represent the antipodal (index  $s = 1$  each) and tetrahedral (index  $s = 1/2$  each) configurations of point disclinations; ew, 2w, and 4w refer to the equatorial (index  $s = 2$ ), two-wall (index  $s = 1$  each), and four-wall (index  $s = 1/2$  each) configurations respectively. The inset depicts the two core sizes required to minimise the total free energy for the 4w-configuration. Order is completely destroyed at  $\zeta = \{\pi/8, \pi/4, \pi/2, \pi/2\}$  for the {4w, 2w, ew, ap}- configurations respectively. Above  $\zeta = (1/2) \arccos(-1/3) \simeq 0.96$ , cores of neighboring disclinations of the tp-configuration overlap each other (see the text). . . . . 27
- 2.3 Minimised free energy  $\mathcal{F} = F_T - 4\pi\eta$ : We set the reference of the total free energy to the condensation energy  $4\pi\eta$  of the entire sphere. The dots indicate the  $\eta$ -values beyond which wall defects are unstable ( $\zeta(\eta) = 0$ ), see Fig. 2.2. The symbols ap, and tp represent the antipodal (index  $s = 1$  each) and tetrahedral (index  $s = 1/2$  each) configurations of point disclinations; ew, 2w, and 4w refer to the equatorial (index  $s = 2$ ), two-wall (index  $s = 1$  each), and four-wall (index  $s = 1/2$  each) configurations respectively. . . . . 28
- 2.4 Equatorial wall: (a) Side ( $\theta = \pi/2, \phi = \pi/2$  at the center) view of the index  $s = 2$ , equatorial wall. The directed lines are the streamlines of the vector field. The shaded region represents the disordered core, within which vector order is completely destroyed, and cannot be assigned a direction. The full field, as given by Eq. 2.19, (including that shown within the core region) corresponds to a wall with zero core-size. Rounding off the slope singularity of the field at the equator, the wall defect of zero core-size transforms into the antipodal configuration of a pair of index  $s = 1$  point disclinations. (b) Front view ( $\theta = \pi/2, \phi = 0$  at the center). (c) Top view, showing that the polar regions are free of point disclinations. . . . . 29

2.5	Interaction potential energy (dimensionless) $\mathcal{F}^{(\text{int})} = F_{(\text{int})}/K_\alpha$ : (a) For the single wall disclination of index $s = 2$ . Clearly, the equatorial configuration ( $\omega = \pi/2$ ) has the minimum energy (b) For the two wall configuration with $s = 1$ each. The function has minimum at $\omega = \pi/3$ rad (See Sec. 2.4.3). . . . .	32
2.6	Two-wall configuration: (a) Side view. The vector field between the two index $s = 1$ walls follows the longitudes. The two-wall configuration degenerates to the antipodal configuration by smoothly sliding the walls towards the respective poles. (b) Front view. (c) Top view. . . . .	32
2.7	Equilibrium position of two wall disclinations: The plot of $\omega_1^{(2w)}$ vs $\eta$ . The dot in the plot represents the limit of stability. . . . .	33
2.8	Tetrahedral configuration: Texture of four point disclinations of index $s = 1/2$ each placed on the vertices of tetrahedron inscribed in sphere. The block dots represent the cores. (a) Front view. (b) Side view. . . . .	35
2.9	Four-wall configuration: (a) Side view. (b) Back ( $\theta \simeq \pi/2$ , $\phi \simeq 3\pi/2$ ) view. (c) Top view. Each wall in this configuration has the index $s = 1/2$ , with uniform linear disclination density. Therefore the change in the angle per unit length across each wall is small as compared to that for index $s = 1$ (and $s = 2$ ) walls. This should be borne in mind, particularly while viewing the back view (b). . . . .	36
2.10	Texture of planar circular wall: (a) Index of the wall $s = 1$ . Outside ring, i.e., $r > r_0$ the texture matches with that of point disclination of index 1. (b) Texture for index $s = -1$ . The texture outside the ring is same as point disclination of index $s = -1$ . In these figures, the shaded region depicts the core centered at $r_0$ . Note that by shrinking the ring to a point transforms a wall disclination to point disclination with same index. . . . .	40
3.1	(a) Catenoid with disclination-free configuration. (b) Helicoid with disclination-free configuration. . . . .	46

- 3.2 Two point disclinations of index  $s = -1$  : (a) Side view ( $z = 0, \phi = 3\pi/2$ ) of two point disclinations of index  $s = -1$ . (b) Front view ( $z = 0, \phi = 0$ ) of two point disclinations of index  $s = -1$ . The black dot in (a) depicts the core region of the point disclination. . . . . 47
- 3.3 Optimal core sizes: The notations (2p), (1w), (2w), (4p) and (4w) represent the two point (index  $s = -1$  each)-, single wall (index  $s = -2$ )-, two wall (index  $s = -1$  each)-, four point (index  $s = -1/2$  each)-and four wall (index  $s = -1/2$  each)-configurations, respectively. The subscripts  $z, \phi$  represent the core sizes along those directions. The inset depicts the two core sizes required to minimise the total free energy for the 4w configuration. For 4p configuration, the optimal cores along  $\phi$  direction overlap up to  $\eta \simeq 0.02$  and indicating the single wall configuration at neck (See the text.). . . . . 49
- 3.4 Minimised free energy  $\mathcal{F}$ : The dots indicate the  $\eta$ -values beyond which wall defects are unstable ( $\zeta(\eta) = 0$ ), see Fig. 3.3. The notations (2p), (1w), (2w), (4p) and (4w) represent the two point (index  $s = -1$  each)-, single wall (index  $s = -2$ )-, two wall (index  $s = -1$  each)-, four point (index  $s = -1/2$  each)-and four wall (index  $s = -1/2$  each)-configurations, respectively. . . . . 50
- 3.5 Wall configuration in vector order: (a) Front view of single wall disclination of index  $s = -2$ . (b) Side view of single wall disclination of index  $s = -2$ . (c) Front view, (d) Side view of two wall disclinations of index  $s = -1$  each. The shaded regions in above figures illustrate cores of the wall disclination(s). . . . . 51
- 3.6 Interaction potential energy (dimensionless)  $\mathcal{F}^{(\text{int})} = F_{(\text{int})}/K_\alpha$  for the single wall disclination of index  $s_0$ . The curve above  $d/a$ -axis is for  $s_0 < 0$ , indicating that negative disclinations are attracted towards the neck region. The behavior of positive disclinations ( $s_0 > 0$ ) is shown in the curve which is below  $d/a$ -axis. Positive disclinations are expelled from the neck region. . . . . 54

- 3.7 (a) Equilibrium position of two-wall configuration: The plot of  $d/a$  vs  $\eta$ . At  $\eta \simeq 0.1$ ,  $d^{(2w)} \simeq 0.55a$ . (b) The interaction potential energy of the two wall disclinations of index  $-1$  each placed symmetrically at  $z = \pm d$ . The function has minimum at  $d \simeq 0.55a$  which implies the division of Gaussian curvature (See text below.). 55
- 3.8 Arrangement of four point disclinations of index  $s = -1/2$  each. The blue dots in the figures represent the position of disclinations. 57
- 3.9 Interaction potential plots of four  $s = -1/2$  point defects: (a) Black color curve is for the alternating configuration (A-I) and blue color curve is for the atop configuration (A-II). (b) Four disclinations placed on the neck with angular position  $\{\pi/4, \omega + \pi/4, 5\pi/4$  and  $5\pi/4 + \omega\}$ . Interaction potential as function of  $\omega$  is plotted and it has minimum at  $\omega = \pi/2$ . . . . . 57
- 3.10 Defects in nematic order:(a) Side view of four point disclinations of index  $s = -1/2$  each. (b) Front view of four point disclinations. (c) Front view of four wall disclinations of index  $s = -1/2$  each. (d) Side view of four wall disclinations. The shaded regions in above figures illustrate the cores. . . . . 58
- 3.11 Arrangement of eight point disclinations of index  $-1/4$  each. The blue dots in all the figures represent the position of disclinations. 60
- 3.12 Interaction potential plots of tetratic order : Eight point disclinations of  $s = -1/4$  each. Black, blue and orange curves represent the configuration-I (C-I) , configuration-II (C-II), and configuration-III (C-III) respectively. Note that blue and black curves coincide for  $d > 0.5$ . The image on the left side shows the zoomed version of the three plots. It indicates that configuration-I with  $d \simeq 0.45a$  has the minimum interaction energy among the three. . . . . 61
- 3.13 Plots of interaction potential for hexatic order : Twelve point disclinations of  $s = -1/6$  each. Blue and black curves represent Configuration-I (C-I) and Configuration-II (C-II) respectively. It indicates that Configuration-I with  $d \simeq 0.5a$  has the minimum interaction energy among the three. . . . . 62

3.14	Minimised free energy $\mathcal{F}$ of finite sized catenoid: Total height in (units of the neck radius $a$ ) of the catenoid is $2\mathcal{L}$ . The dots indicate $\eta$ -values beyond which wall defects are unstable ( $\zeta(\eta) = 0$ ). (a) $\mathcal{L} = 0.5$ , (b) $\mathcal{L} = 1$ , (c) $\mathcal{L} = 1.5$ and (d) $\mathcal{L} = 2$ . . . . .	63
4.1	The disclination-free configuration . . . . .	66
4.2	(a) Streamlines of two $s = -1$ point disclinations on the axis of a helicoid ( $r = 0$ ; $\phi = \pi/2, 3\pi/2$ ). (b) The plot of $F_{el}$ (in $K_\alpha$ units) vs $w/b$ : Orange color curve is for uniform configuration. Blue- and black curves represent the elastic free energy of two point disclinations with core sizes (or, cutoffs) $0.05b$ and $0.1b$ , respectively. . . . .	67
4.3	Arrangement of four point disclinations of index $s = -1/2$ each. The blue dots in the figures represent the position of disclinations. . . . .	68
4.4	(a) Interaction potential energy plots of point disclination in nematic order: Blue and black curves are for Alternating (A-I) and Atop (A-II) configurations. (b) Streamlines of four point disclinations placed on the axis of the helicoid ( $\rho = 0$ ; $\phi = \pi/4, 3\pi/4, 5\pi/4$ and $7\pi/4$ ). . . . .	69
4.5	Interaction potential energy plots of tetratic order: Blue and black color curves represent the Configuration-I (C-I) and Configuration-II (C-II) respectively. It indicates that configuration-I with $\rho \simeq 0.475 b$ has the minimum interaction energy. . . . .	69
4.6	Interaction potential plots for hexatic order: Twelve point disclinations of $-1/4$ each. Blue and black color curves represent the configuration-I (C-I) and configuration-II (C-II) respectively. It indicates that configuration-I with $\rho \simeq 0.5 b$ has the minimum interaction energy. . . . .	70
4.7	Streamlines of wall disclination(s) on a helicoid:(a) Single wall disclination with index $s = -2$ placed on the axis of helicoid. (b) Two wall disclinations of index $s = -1$ each. (c) Four wall disclinations of index $s = -1/2$ each. The shaded regions in these figures depict core regions. . . . .	72

- 5.1 Morphologies of polymer crystallites. (a). Spherulite: Schematic representation of spherulite obtained by radially growing polymer lamellae. The first magnified image illustrates the lamellar structure and second magnified image shows the crystalline arrangement. Image credits: Dingler et.al, Macromol. Rapid Commun.2019. (b). Twisted spherulite: Polymer lamellae twisted in the form of helicoids. (c) Scroll: Lamellae are rolled over. Images (b) and (c) are borrowed from Ref [4]. . . . . 79
- 5.2 Adjacent re-entry model: (a) Schematic representation of adjacent re-entrant folds. The free polymer chains resemble cilia, microscopic hairlike vibrating structures (b) Schematic of lamellar stack with adjacent re-entrant folds. Images are taken from the internet. 80
- 5.3 TEM images of solution-grown single crystals: (a) Lozenge shape sector: Linear polyethylene crystal decorated with polyethylene vapour. (b) Hexagonal sector: Polyoxymethylene single crystal decorated with polyethylene vapour. Images (a) and (b) are borrowed from Wittmann and Lotz (1985). (c) Poly( $\epsilon$ -caprolactone) crystal grown from a n-hexanol solution at 40C. (Image is taken from Nunez and Gedde (2005)) . . . . . 80
- 5.4 Schematic illustration of folds at the surface of polymer lamella in sector configuration: (a) Lozenge shaped sector: It has four  $\{110\}$  sectors. (b) Hexagonal sector: It has four  $\{110\}$  sectors and two  $\{100\}$  sectors. Here vectors  $a, b$  are the crystal axes. . . . . 81
- 5.5 (a). Schematic illustration of unit cell of a crystalline polyethylene lamella. The unit cell has symmetry of base-centered orthorhombic. Here  $\mathbf{a}, \mathbf{b}$  and  $\mathbf{c}$  represent the the crystal axes and lamella is  $xy$ -plane with lamellar normal is along the  $z$  axis. Note that the  $\mathbf{c}$  axis of the unit cell is tilted with respect to the  $z$  axis. Blue and red colored shaded strips represent oriented stems formed by the all-trans configurations. Folds are not shown. Image is taken from Ref [5]. (b) Cartoon showing trans-gauche configurations of polyethylene and fold formation. Image is taken from S.P.Schmm et al., macromolecules, (1994). . . . . 82

5.6	Surface of the PE lamella: (a) Viewed along the $c$ -axis. The two dashed lines represent the two possible folds. Energetically the thick dashed fold is favourable. (b) Illustration of lozenge-shaped, sectored lamella. Images are taken from Ref. [5] . . . . .	84
5.7	Square sector: Texture of fold field obtained from the exact solution $\alpha_s(x, y)$ . Two shaded lines represent the soliton type walls of wall width $w$ . The fold field follow stream lines of +1 disclination and the disclination core is located at the center of the square. . . . .	88
5.8	(a) Uniform fold field: Squared shaped lamella with side length (in $w$ units) $L$ . (b) Sector: Square shaped sector with side length (in $w$ ) units $L$ . Shape of the core is symmetrical to the sector and has side length (in $w$ ) $\zeta$ . . . . .	89
5.9	Phase diagram of sector and uniform configurations: The curve is a phase boundary between between square sector and uniform configurations. Region below/ above the curve is the stability range for uniform/ sector configuration. . . . .	92
6.1	AFM images of solution-grown single crystals: (a) Convex hollow pyramidal type. (b) Concave hollow pyramidal type. (c) Chair type. (Image is taken from Toda group,2003 [64]) . . . . .	96
6.2	(a) Cartoon of tent configuration depicting essential features. (b) Illustration of buckling of a sector into tent configuration. . . . .	97
6.3	Schematics of bending of the polymer crystalline lamella. Two types of bending: (i) Splay-like bending in which polymer stems undergo splay deformation. (ii) Slide-like bending in which the stems point along the vertical direction via sliding mechanism. . . . .	98
6.4	(a) A square pyramid (tent) surface: A plot of the height function $h(x, y)$ . The black vertical and the blue lines represent axis and faces of the tent surface respectively. (b) Schematics of apex angle( $2\beta$ ): By definition, the angle between axis and face of the tent is $\beta$ . The asymptotic slope of the tent face (blue line) is $\tan(\pi/2 + \beta)$ . . . . .	100
6.5	Cartoon of buckling of polymer lamella with tilted stem into tent configuration. . . . .	101

6.6	Schematics of the fold field: (a) On the tent surface (an exaggerated height field). Note the tent edges match with soliton-type walls in the fold field. The base length of the tent, in $w$ units, is $L_T$ . The black colored square represents the core with side length $\zeta$ (in $w$ units). (b) For flat sector of side length $L$ (in $w$ units). (c) For flat uniform configuration. . . . .	103
6.7	The phase diagram: Plots indicating stability range of the tent, the flat sector and the flat uniform. . . . .	106
A.1	Magnitude of order parameter around equatorial wall disclination:	113

# Chapter 1

## Introduction

### 1.1 Soft matter

Soft matter physics is a particular branch of solid-state physics that studies easily deformable systems. The word “soft” implies that minimal mechanical stresses or even the thermal fluctuations (or entropic forces) are enough to deform those systems [6, 7, 8, 9, 10]. Soft matter physics covers various exotic systems such as liquid crystals, lipid membranes, polymers, colloids, gels, foams, emulsions, granular particles, and some biological systems. The standard and exciting feature in all these materials is that corresponding elastic moduli are very small. For example, the shear modulus of the blue phase liquid crystal is of the order 100 Pa, which is  $10^9$  times lesser than that of aluminum metal [6]. The energy scales of soft materials are comparable to thermal energy so, the quantum effects are negligible. Thus, most of the soft materials are studied with classical phenomenological theories [3, 6, 7].

The internal structures and morphologies of these soft phases and materials are quite fascinating. For example, self assembly of lipids (amphiphilic molecules) in aqueous solution results micelles, mono-layers, bi-layers, vesicles, and cylindrical micelles depending on the amphiphilic concentration and molecular packing parameter [11, 12]. In this thesis we focus on *two-dimensional* morphologies with in-plane order. Examples of two-dimensional soft materials are nematic films and vesicles, smectics ( $Sm - A$ ,  $Sm - C$ ,  $Sm - F$ ) [13], membranes, lamellar phases of lipid bilayers ( $L_\alpha$ ,  $L_\beta$ ,  $L'_\beta$ ; lyotropic analog of smectics) [14], elastomer sheets [15], etc. They offer an ideal testing ground for fundamental concepts involving order (symmetry), low-energy excitations, topological defects,

and thermal fluctuations. Other fascinating systems that we explore in this thesis (Part-II) are morphologies of polymer crystallites. Interestingly these morphologies are lamellar in nature. Thus we consider them as effectively two dimensional surfaces with in-plane crystalline order and orientational order (See Chapter 5 for more details).

The basic theme of this thesis is to study the interplay between geometry, topology, and elasticity in two-dimensional soft materials with in-plane orientational order. In this chapter, we discuss some examples of in-plane order and corresponding topological defects (in Sec. 1.2), followed by geometry of a two dimensional membrane, or surface (in Sec. 1.3).

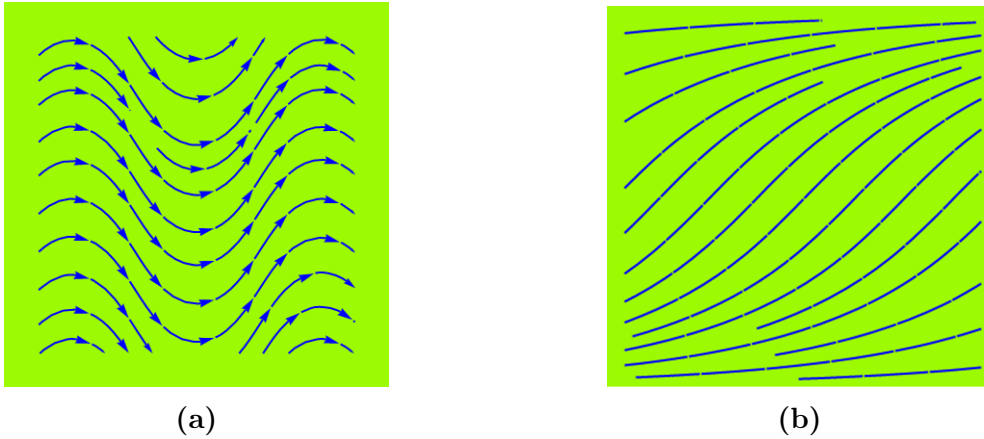


**Figure 1.1:** Schematics of in-plane orientational orders. (a) Vector order ( $n = 1$ ) (b) Nematic order ( $n = 2$ ): The nematic phase is a liquid crystalline phase with head-tail symmetry consisting of anisotropic molecules with no positional ordering. It has orientational (two-fold) order and breaks the rotational symmetry of the fluid phase. (See the Sec. 1.2 )

## 1.2 Order and Topological defects

To describe tangent plane (or, in-plane)  $n$ -atic orientational order in a flat surface, we introduce a unit vector  $\hat{\mathbf{m}}(x, y) = \cos \alpha(x, y) \hat{\mathbf{x}} + \sin \alpha(x, y) \hat{\mathbf{y}}$ , or a complex order parameter  $\psi = \psi(x, y) = |\psi(x, y)| \exp[i \alpha(x, y)]$  [16]. Here the coarse grained [3] angle  $\alpha$  is measured modulo  $2\pi/n$  with respect to  $(\hat{\mathbf{x}}, \hat{\mathbf{y}})$ . The in-plane vector- and nematic order are represented by  $n = 1$  and  $n = 2$  respectively (See Fig. 1.1).

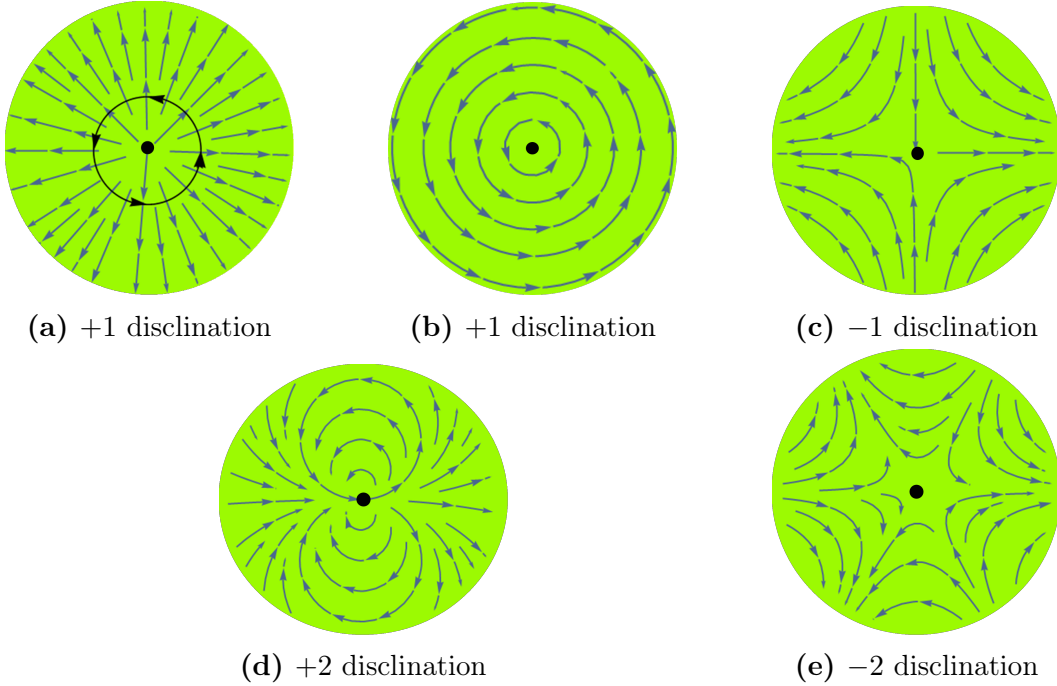


**Figure 1.2:** Topological defects in vector order: Dots in the figures represent the core regions. The black curve in (a) is an anti-clockwise contour to characterise the defect.

The in-plane orientational order in the ordered phase breaks the rotational symmetry (continuous symmetry) of the phase. In the ordered phase, there exist topological defects, which try to restore the symmetry in the ordered phase [17]. These defects are topologically stable, i.e., in-order to remove these defects, we need to take them to infinity or make cuts in the ordered phase. In the soft matter context, they are often called as disclinations. Examples of point-disclinations in vector ( $n = 1$ ) and nematic ( $n = 2$ ) order are shown Fig. 1.2 and Fig. 1.3 respectively.

A disclination has core region, in which order gets destroyed and melts to disordered phase, and “charge” associated to it. To characterise point disclinations, we consider an anti-clockwise loop around the core 1.2(a). If the unit vector  $\hat{\mathbf{m}}$  (order parameter  $\psi$ ) on the loop changes in same sense with the loop direction, then the disclination is positive. Otherwise it is negative. Number of rotation of  $\hat{\mathbf{m}}$  for one complete loop defines the charge or index of the disclination.



**Figure 1.3:** Topological defects in nematic order:

Mathematically topological defects are characterised by [3]

$$\oint_L d\alpha = 2\pi s \quad (1.1)$$

where  $L$  is the anti-clockwise loop enclosing the disclination core and  $s$  is the index of the disclination. For vector order  $s$  values are positive or negative integers. We note that nematic order has up down symmetry that allows  $s$  to take positive or negative half-integer values (See Fig. 1.3).

To characterise defects in crystalline order in a plane, we recall the displacement vector  $\mathbf{u}(x, y) = u_x \hat{\mathbf{x}} + u_y \hat{\mathbf{y}}$  [18]. In the presence of topological defects,  $\mathbf{u}$  becomes multi-valued function. There are two kinds of topological defects in crystalline order, namely dislocation and disclinations (See Fig. 1.4). Disinclination in crystalline order arises from the orientational order of the lattice points. It is obtained by insertion/removal of a wedge with an angle  $\omega$ . Thus, in the presence of disclinations coordination number (number of nearest neighbours for a lattice point) for the disclination core is changed (See Fig. 1.4(a), Fig. 1.4(b)). The bond angle for the orientation of the lattice points, for small deformations, is given by  $\Theta = (1/2)(\partial_x u_y - \partial_y u_x)$  [19]. If  $\omega$  is the angle deficit/gain corresponding to a disclination, then loop integral of  $\Theta$  enclosing disclination core is given by

$$\oint_L d\Theta = \omega \quad (1.2)$$

where  $L$  is the anti-clockwise loop around the disclination.

In two dimensions, dislocations are obtained by addition or removal of lattice lines in the crystalline order. It is characterised by Burgers vector ( $\mathbf{b}$ ) and defined

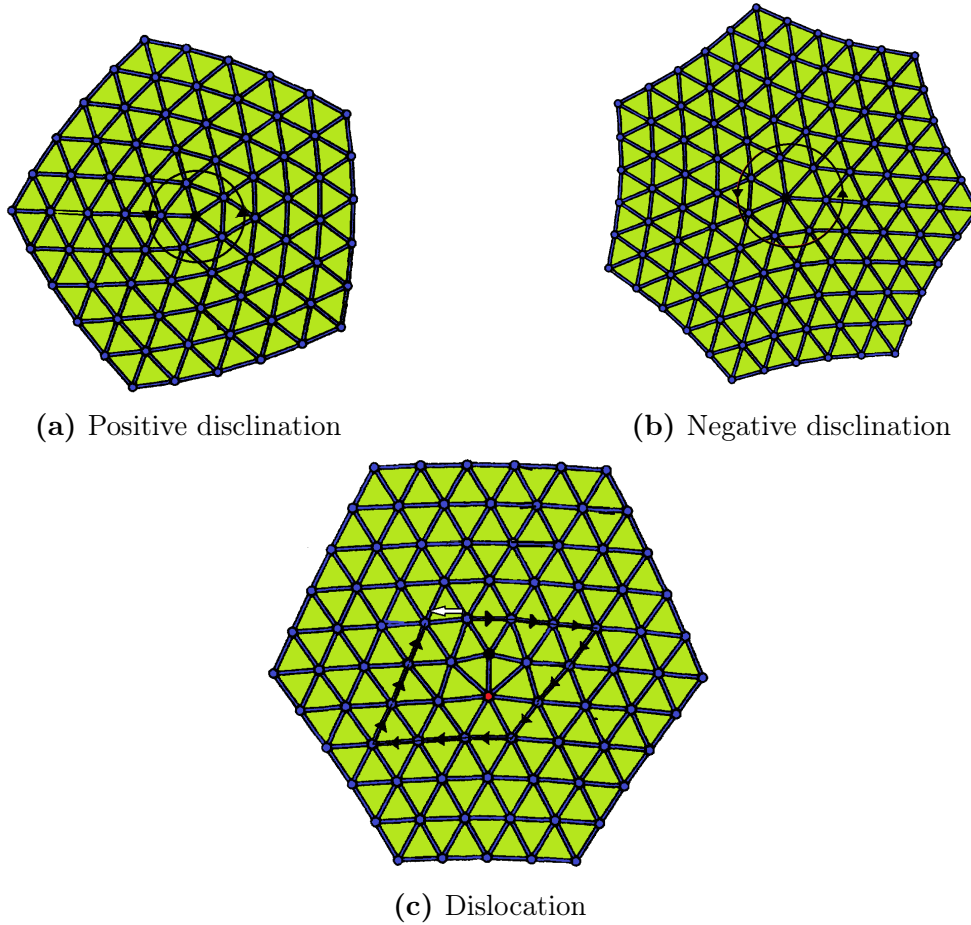


**Figure 1.4:** Crystal defects in two-dimensional hexagonal lattice: The coordination number for hexagonal lattice is 6. (a) Positive disclination: Five-fold (black dot) coordination number and angle deficit  $\omega = 2\pi/6$ . Black curve indicates the counter-clock wise loop  $L$ . (b) Negative disclination: Seven-fold (black dot) coordination number and  $\omega = -2\pi/6$ . Here the negative sign indicates that a wedge with angle  $\omega$  is added at the core. (c) Dislocations are pairs of positive (black dot) and negative (red dot) disclinations. The white arrow represents the Burgers vector (See the text).

by [3]

$$\oint_L d\mathbf{u} = \mathbf{b} \quad (1.3)$$

where  $L$  is the anti-clockwise loop containing dislocation core. A dislocation in two-dimensions consists of a bound pair of positive and negative disclinations (See Fig. 1.4(c)). In the presence of dislocation, taking an equal number of steps in four directions to enclose a path around the core will not lead to the starting point. The direction from starting to end points on the path defines the Burgers

vector which completes the circuit around the core. For the dislocation shown in Fig. 1.4(c), the white arrow represents the Burgers vector.

### 1.3 Curvature of a membrane

Mathematical description of two dimensional surfaces in three dimensions are very well studied. In this thesis, we use the differential geometry techniques to study the curves and surfaces in 3-dimensions [20, 21, 22, 23]. Let  $\mathbf{R}(\underline{\mathbf{x}})$  be the parametrisation of a given two dimensional surface embedded in three dimensions with the internal coordinates  $\underline{\mathbf{x}} = (x^1, x^2)$  (Fig. 1.5). Tangents to the surface, at any point, are given by  $\mathbf{t}_\mu = \partial_\mu \mathbf{R}$  with  $\partial_\mu = \partial/\partial x^\mu$  and  $\mu = \{1, 2\}$ . The unit, outward surface normal ( $\hat{\mathbf{N}}$ ) and the metric tensor ( $g_{\mu\nu}$ ) are defined by  $\hat{\mathbf{N}}(\underline{\mathbf{x}}) = (\mathbf{t}_1 \times \mathbf{t}_2)/(|\mathbf{t}_1 \times \mathbf{t}_2|)$  and  $g_{\mu\nu} = \mathbf{t}_\mu \cdot \mathbf{t}_\nu$ , respectively. Determinant of the metric tensor defines the metric ( $g$ ) of the given surface i.e.,  $g = \det(g_{\mu\nu})$ . Any vector  $\mathbf{V}$  that belongs to the tangent plane of the surface can be expressed as  $\mathbf{V} = V^\mu \mathbf{t}_\mu = V_\mu \mathbf{t}^\mu$ , where Einstein's notation of summation over repeated indices is implemented. Hereafter, we follow the same convention. The components  $V_\mu$  ( $V^\mu$ ) form covariant (contravariant)-vector in the tangent plane.

The curvature information of the surface is given by curvature tensor and it is defined as  $K_{\mu\nu} = \hat{\mathbf{N}} \cdot \partial_\nu \mathbf{t}_\mu$ . Mean ( $H$ ) and the Gaussian curvature ( $K$ ) are, by definition,  $H = \frac{1}{2} \text{tr}(K^\mu{}_\nu)$  and  $K = \det(K^\mu{}_\nu)$ , respectively. Here,  $K^\mu{}_\nu$  is the mixed curvature tensor. Mean curvature is an extrinsic property and depends on the embedding of the surface and its normal. The Gaussian curvature is intrinsic, and depends only on the metric ( $g_{\mu\nu}$ ) [20, 21].

Understanding of mean and the Gaussian curvatures are simpler if we make use of principal curvatures (say,  $\kappa_1$  and  $\kappa_2$ ) along the principal directions (orthogonal to each other) (Fig. 1.6). By definition, principal curvature is reciprocal of the radius of a circle inscribed along the principal direction. For radii of curvatures  $r_1$  and  $r_2$  curvatures  $\kappa_1 = 1/r_1$  and  $\kappa_2 = 1/r_2$ . Depending on the convention, principal curvature can be positive or negative. For example, if the center of the inscribed circle is in the same direction as the unit surface normal ( $\hat{\mathbf{N}}$ ), then the principal curvature is positive. Otherwise, it is negative. In terms of principal

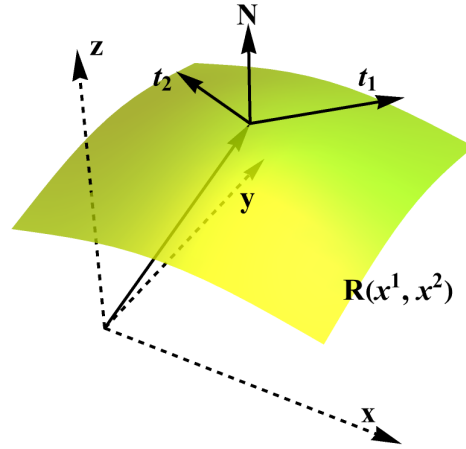


**Figure 1.5:** A 2-dimensional surface in 3-dimensions: Vectors  $\mathbf{t}_1$ ,  $\mathbf{t}_2$  and  $\mathbf{N}$  are tangents and normal to the surface of parametrisation as  $\mathbf{R}(x^1, x^2)$ .

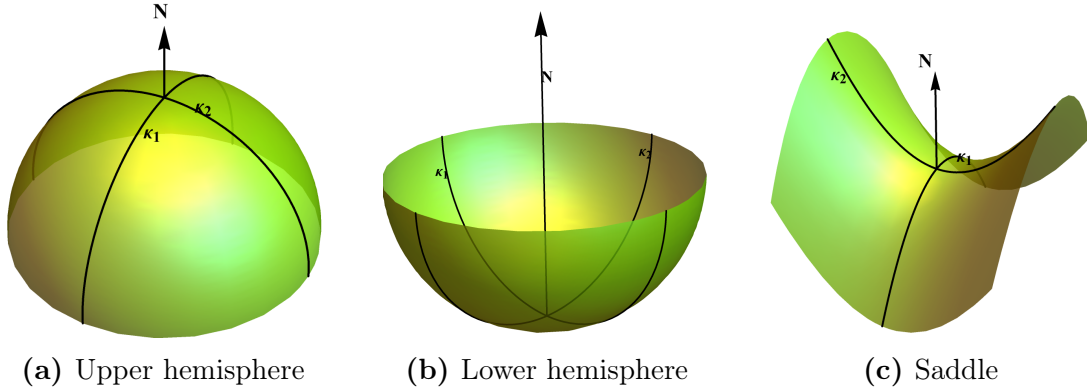


**Figure 1.6:** Curvature of a surface: The surface normal ( $\mathbf{N}$ ) points upward. Two black-curves in the figures represent the principal radii (corresponding principal curvatures  $\kappa_1$ ,  $\kappa_2$ ) at the point of intersection. (a) Upper hemisphere: Following the convention (see text), we get  $\kappa_1 < 0$  and  $\kappa_2 < 0$ . Thus mean curvature  $H < 0$  and Gaussian curvature  $K > 0$ . (b) Lower hemisphere: Here  $\kappa_1 > 0$  and  $\kappa_2 > 0$ . Therefore  $H > 0$ ;  $K > 0$ . (c) Saddle: For this surface,  $\kappa_1 < 0$ ;  $\kappa_2 > 0$ . Saddle is a minimal surface i.e.,  $\kappa_2 = -\kappa_1$  so that  $H = 0$  and  $K < 0$ .

curvatures, mean ( $H$ ) and the Gaussian ( $K$ ) curvatures are given by

$$\begin{aligned} H(\underline{\mathbf{x}}) &= \frac{1}{2} \text{tr}(K^\mu{}_\nu) = \frac{1}{2}(\kappa_1 + \kappa_2) \text{ and,} \\ K(\underline{\mathbf{x}}) &= \det(K^\mu{}_\nu) = \kappa_1 \kappa_2. \end{aligned} \quad (1.4)$$

Notice that mean curvature depends on the convention, and the Gaussian curvature is independent of the convention.

## 1.4 Interplay between shape, order and topological defects

The ground-state configuration of a planar membrane with in-plane orientational order breaks the rotational symmetry. The ordered phase, in its ground-state, spontaneously picks up one of the states in the ground-state manifold. For the case of vector order, one of the ground-states is that all vectors are aligned along  $\hat{x}$ -direction (Uniform configuration). Establishment of in-plane order on a curved membrane (with non zero Gaussian curvature) introduces geometrical frustration in the order [24]. The uniform ordering may not be possible as the Gaussian curvature acts as a source of geometrical frustration. Thus the ground state configuration contains topological defects to counter the frustration caused in the ordering.

A striking example of geometrical frustration is given by the Poincaré-Hopf index theorem [25, 26]. The theorem states that a sphere with in-plane orientational order must have a singular, isolated point disclination of index  $s = 2$ , or isolated disclinations with total index  $s_T = 2$ . The ground state configurations (with point-disclinations) for the vector, nematic order, and triangular lattice are shown in the Fig. 1.7.

Topological defects (disclinations) have in-plane stresses due to misalignment of ordering away from the core. These stresses increase with system size. When the disclinations emerge on a flexible membrane, they tend to change the shape of the membrane by buckling. This is due to the fact that buckling of the membrane allows disclinations to reduce in-plane stresses [2, 27]. Illustration of buckling of membranes in the presence of disclinations are shown in Fig. 1.8.

In short, there is a delicate interplay between order, geometry, and topological defects. It establishes that Gaussian curvature of membranes acts as a source of defects in the orientational order. Conversely, defects tend to bend flat, deformable membranes. Positive and negative defects of equal strength prefer locally positive (sphere-like) and negative (saddle-like) Gaussian curvatures. The interplay plays a key role in this thesis. In addition to the interplay, energetics of membrane with in-plane orientational order is essential to obtain equilibrium shapes. Below, we discuss the free energy and equilibrium equations for fluid membranes with in-plane orientational order.

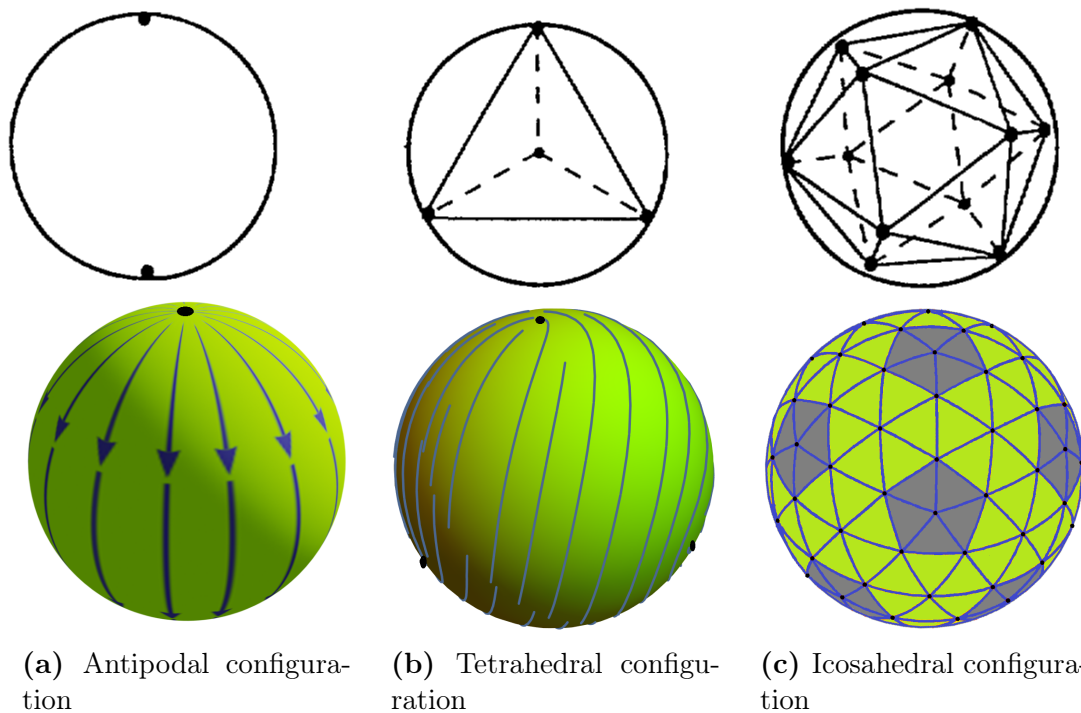


**Figure 1.7:** Ground state configurations of in-plane orientational order on spheres containing point defects: The images in upper row show the equilibrium positions of point defects in vector-, nematic-order and hexagonal lattice, and lower row depicts the corresponding textures. (a) Antipodal configuration for vector order. Two point disclination of index  $s = 1$  placed at north and south poles. (b) For nematic order, equilibrium position of four  $+1/2$  disclinations are vertices of tetrahedron inscribed in a sphere. (c) In hexatic order and also in hexagonal lattice, the ground state has 12 positive disclinations (five-folded coordination number) located on the vertices of icosahedron inscribed in a sphere. The color images shows the equilibrium configuration of hexagonal lattice on a sphere.

## 1.5 Energetics and Euler-Lagrange equations of fluid membranes with in-plane order

Typically, the thickness of the membranes is of the order of nanometers, and the lateral dimensions are up to micro-meters. As the lateral dimensions of the membrane are much larger than its thickness, we model the membranes as mathematical surfaces with “zero” thickness.

Total free elastic energy of a fluid membrane with in-plane orientational order has contributions from bending (Helfrich free energy), surface tension, and from

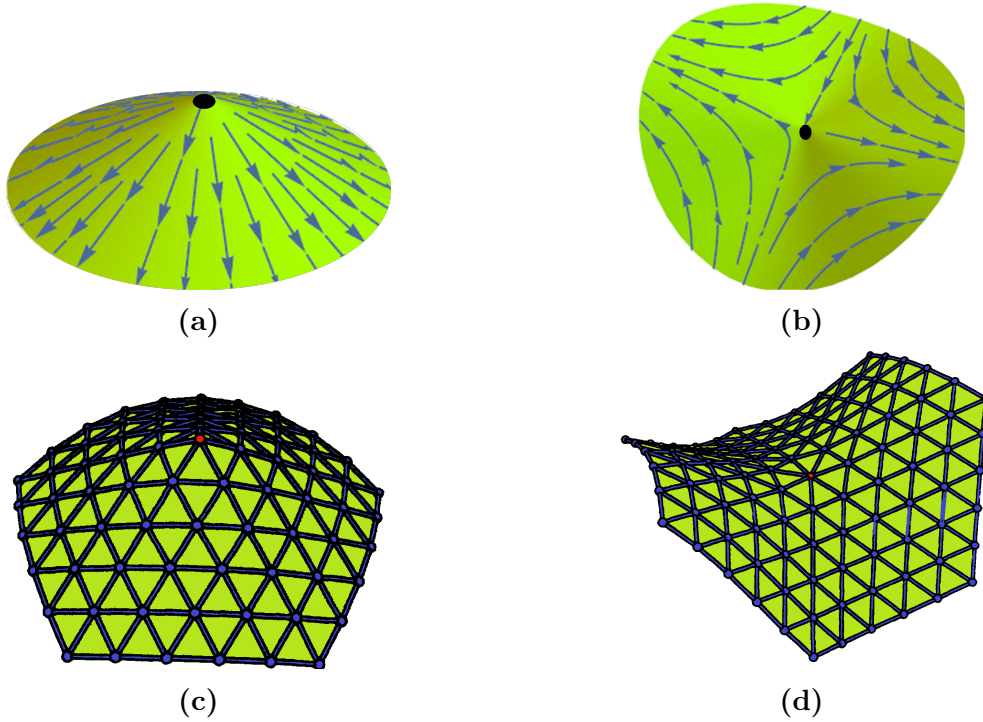


**Figure 1.8:** Schematics of buckling phenomenon of flexible membranes in presence of topological defects: Positive disclinations in vector order (sub fig.(a) ) and hexagonal lattice (sub fig.(c) ) buckle to conical shape whose Gaussian curvature is positive. Similarly, negative defects acquire shapes that have negative Gaussian curvature (sub Figs.(d) and (d) ).

distortions in orientational order (Frank free energy). The Helfrich bending free energy ( $F_H$ ) of the fluid membrane is [28],

$$F_H = \int \left[ \frac{\kappa}{2} (H(\mathbf{x}) - H_0)^2 + \kappa_G K(\mathbf{x}) \right] d\mathcal{A} \quad (1.5)$$

where,  $\kappa$  and  $\kappa_G$  are the bending rigidity and Gaussian rigidity, and the area element  $d\mathcal{A} = \sqrt{g} dx^1 dx^2$ . The integral is taken over the curved membrane and  $H$ ,  $H_0$  and  $K$  are mean, spontaneous and Gaussian curvatures of the membrane, respectively. For symmetric membranes  $H_0 = 0$ .

The expression for surface tension energy ( $F_S$ ) is given by

$$F_S = \sigma \int d\mathcal{A}, \quad (1.6)$$

where  $\sigma$  is the surface tension.

For a finite membrane with boundary, there is also line tension contribution in addition to the bulk energy. The free elastic energy from line tension has the form

$$F_l = \gamma \oint dl, \quad (1.7)$$

where  $\gamma$  is the line tension and  $dl$  is length element on the boundary.

### 1.5.1 Frank free energy $F_\alpha$

To arrive at a qualitative expression for  $F_\alpha$ , let us recall the two dimensional continuum  $xy$  model on a rigid, flat surface. The order parameter  $\hat{\mathbf{m}}(x, y) = (\cos \alpha(x, y), \sin \alpha(x, y))$ , where  $\alpha(x, y)$  is the coarse grained angle that the  $\hat{\mathbf{m}}(x, y)$ -vector (indicating 1-atic order) makes with respect to the  $x$ -axis (See Fig. 1.9(a)).

The uniform  $\hat{\mathbf{m}}$  (i.e.,  $\alpha = \text{const.}$ ) is a reference state. Any elastic deformation in  $\hat{\mathbf{m}}$  contributes to the Frank free energy  $F_\alpha$ . For two dimensional vector field such as  $\hat{\mathbf{m}}$ , there exist two types of independent deformations. They are splay-(in which divergence of  $\hat{\mathbf{m}}$  is non zero) and bend-(in which curl  $\hat{\mathbf{m}}$  is non zero) deformations. Thus, the free elastic energy  $F_\alpha$  is given by [29]

$$F_\alpha = \int \left( \frac{K_1}{2} (\boldsymbol{\partial} \cdot \hat{\mathbf{m}}(x, y))^2 + \frac{K_2}{2} (\boldsymbol{\partial} \times \hat{\mathbf{m}}(x, y))^2 \right) dx dy, \quad (1.8)$$

where  $\boldsymbol{\partial}$  is the ordinary flat-space gradient operator, and  $K_1$  and  $K_2$  are the splay- and bend elastic constants respectively. Within the ‘‘one-constant approximation’’  $K_1 = K_2 = K_\alpha$  [9], Eq.1.8 reduces to

$$F_\alpha \simeq \frac{K_\alpha}{2} \int |\boldsymbol{\partial} \alpha(x, y)|^2 dx dy \quad (1.9)$$

because  $\hat{\mathbf{m}}$  is a unit vector. This is the commonly used, square-gradient elastic free energy for the continuum  $xy$  model.

We note that the rigid, flat plane allows us to use the *global, orthonormal* frame with respect to which the angle  $\alpha(x, y)$  can be defined. This is not possible on deformable, curved surfaces, where it is necessary to set up a local orthonormal frame ( $\hat{\mathbf{e}}$  – *basis*) to define  $\alpha$  [1]. Unlike in the flat case, on a curved surface the  $\hat{\mathbf{e}}$ – basis is spatially varying. The relation between orthonormal basis  $\hat{\mathbf{e}}_i(x^\mu)$  and

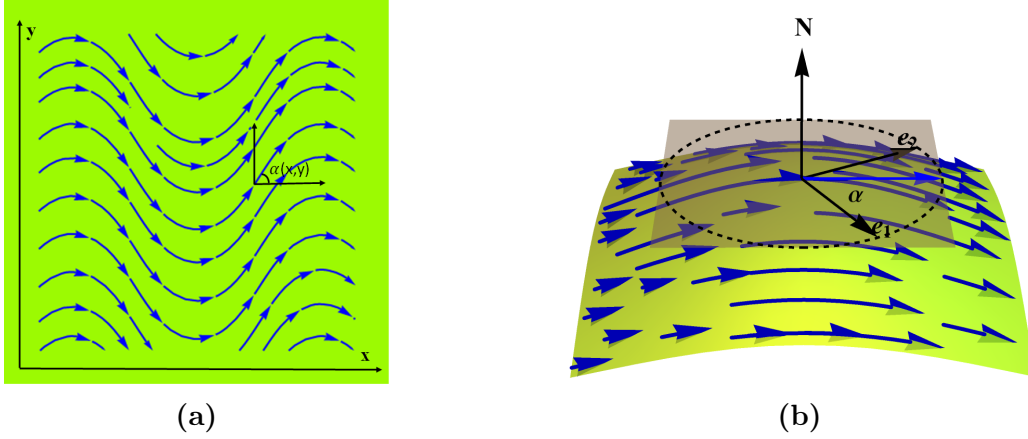


**Figure 1.9:** Orthonormal frame: (a) For a flat membrane, the angle  $\alpha$  is measured with respect to the  $\hat{\mathbf{x}}$ -axis (fixed orthonormal frame). (b) On curved membrane,  $\alpha$  is measured with respect to the orthonormal  $\hat{\mathbf{e}}$ -basis. The tips of the basis vectors can lie anywhere on the unit circle in the tangent plane, implying  $O2$  symmetry.

tangent basis is given by

$$\hat{\mathbf{e}}_i(\mathbf{x}) = E_i^\mu(\mathbf{x}) \mathbf{t}_\mu(\mathbf{x})$$

where  $i = \{1, 2\}$ ,  $\mu = \{1, 2\}$ .  $E_i^\mu$  are called vierbein or frame field. Henceforth we preserve the notation that Latin letters  $\{i, j, l..\}$  represent  $\hat{\mathbf{e}}$ -basis, whereas, Greek letters  $\{\mu, \nu, \lambda..\}$  represent  $\mathbf{t}$ -basis. The unit vector  $\hat{\mathbf{m}}(\mathbf{x})$  in  $\hat{\mathbf{e}}$ -basis takes the form

$$\begin{aligned} \hat{\mathbf{m}} &= m_i(\mathbf{x}) \hat{\mathbf{e}}_i(\mathbf{x}) \\ &= \cos \alpha(\mathbf{x}) \hat{\mathbf{e}}_1(\mathbf{x}) + \sin \alpha(\mathbf{x}) \hat{\mathbf{e}}_2(\mathbf{x}). \end{aligned}$$

Since the  $\hat{\mathbf{e}}$ -basis is locally Euclidean, there is no distinction between raising and lower indices i.e.  $m_i = m^i$ . With the help of  $\hat{\mathbf{e}}$ -basis, the expression for  $F_\alpha$  takes the form [1]

$$F_\alpha = \frac{1}{2} K_\alpha \int (\partial\alpha - \mathbf{A})^2 d\mathcal{A} \quad (1.10)$$

with notation  $(\partial\alpha - \mathbf{A})^2 \equiv g^{\mu\nu}(\partial_\mu\alpha - A_\mu)(\partial_\nu\alpha - A_\nu)$  and  $g^{\mu\nu}$  is inverse of  $g_{\mu\nu}$ .

The spin connection  $\mathbf{A}$  has information about spatial variation of  $\hat{\mathbf{e}}$ -basis, and is defined as  $A_\mu = (1/2) (\hat{\mathbf{e}}_1 \cdot \partial_\mu \hat{\mathbf{e}}_2 - \hat{\mathbf{e}}_2 \cdot \partial_\mu \hat{\mathbf{e}}_1)$  [1]. It is a gauge field and the transformation  $\alpha \rightarrow \alpha + \Psi$  implies  $A_\mu \rightarrow A_\mu + \partial_\mu \Psi$  such that  $\partial_\mu \alpha - A_\mu$  is invariant under  $O2$  freedom of  $\hat{\mathbf{e}}$ -basis. Thus, Eq. 1.10 is also invariant under the  $O2$  symmetry. The covariant derivative  $\mathcal{D}_\mu \equiv \partial_\mu \alpha - A_\mu$  measures true deformation

in  $\hat{\mathbf{m}}$  and accounts for the correct free energy cost. We note that the Gaussian curvature( $K$ ) and spin connection terms are related by [1]

$$K = \gamma^{\mu\nu} \nabla_\mu A_\nu \quad (1.11)$$

where  $\gamma^{\mu\nu} = \epsilon_{\mu\nu}/\sqrt{g}$  and anti-symmetric tensor  $\epsilon_{\mu\nu}$ , by definition,  $\epsilon_{12} = -\epsilon_{21}$ ;  $\epsilon_{11} = \epsilon_{22} = 0$ . The symbol  $\nabla_\mu$  represents covariant derivative on the surface. Having obtained the free energy of the membrane, we discuss the equilibrium equations below.

### 1.5.2 Euler-Lagrange equations

Minimisation of total elastic free energy ( $F_{\text{el}}$ ) gives the Euler-Lagrange equations. Total (bulk) free elastic energy  $F_{\text{el}}$  is

$$F_{\text{el}} = F_{\text{H}} + F_{\alpha} + F_{\text{S}} \quad (1.12)$$

There are two kinds of minimization in the free energy of a fluid membrane with in-plane orientational order. First, minimization of orientational order field by keeping the shape of membrane fixed and second, shape variation by keeping orientational order field unaltered (Lie dragging).

#### The $\alpha$ -equation

The  $\alpha$ -equation is obtained by varying  $F_{\text{el}}$  with respect to  $\alpha$ , and it is given by

$$\frac{\delta F_{\text{el}}}{\delta \alpha} = -K_\alpha \nabla \cdot (\partial \alpha - \mathbf{A}) = 0 \quad (1.13)$$

where  $\nabla \cdot$  represents covariant divergence [20, 21].

We use of Airy stress function formalism to solve the Eq. 1.13 [2]. The stress function  $\chi$  is defined as,  $\nabla^\mu \chi = \gamma^{\mu\nu} (\partial_\nu \alpha - A_\nu)$  such that  $\alpha$ -equation (Eq. 1.13) is satisfied automatically. Uniqueness of stress function  $\chi$  is achieved with *the compatibility condition*

$$\nabla^2 \chi(\underline{\mathbf{x}}) = K(\underline{\mathbf{x}}) - \mathcal{S}(\underline{\mathbf{x}}) \quad (1.14)$$

where Laplace-Beltrami operator  $\nabla^2 = \frac{1}{\sqrt{g}} \partial_\mu (\sqrt{g} g^{\mu\nu} \partial_\nu)$ . The coarse grained, continuum disclination density i.e., number of disclinations per unit area on the

membrane, by definition, is given by [2]

$$\mathcal{S}(\underline{\mathbf{x}}) = \gamma^{\mu\nu} \nabla_\mu \partial_\nu \alpha. \quad (1.15)$$

If the membrane has  $N$  discrete, point disclinations of indices  $s_i$  at position  $\underline{\mathbf{x}}^i$  (for  $i = 1, 2, \dots, N$ ), disclination density is given by

$$\mathcal{S}(\underline{\mathbf{x}}) = \frac{2\pi}{\sqrt{g}} \sum_i^N s_i \delta^{(2)}(\underline{\mathbf{x}} - \underline{\mathbf{x}}^i)$$

where  $\delta^{(2)}(\underline{\mathbf{x}})$  is two dimensional Dirac delta function. In terms of stress function  $\chi$ ,  $F_\alpha$  is given by [2]

$$F_\alpha = \frac{K_\alpha}{2} \int g^{\mu\nu} (\partial_\mu \chi) (\partial_\nu \chi) d\mathcal{A}. \quad (1.16)$$

We note that the curvature ( $K$ ) and disclination density ( $\mathcal{S}$ ) of the membrane surface are connected by compatibility condition (Eq. 1.14) which elucidates the interplay between shape, order and topological defects.

## The shape equation

The shape variation can be along tangents (stretching) and normal (bending) and given by  $\delta \mathbf{R} = \delta R_\parallel^\mu \mathbf{t}_\mu + \delta R_\perp \hat{\mathbf{N}}$ . Here  $\delta R_\parallel^\mu$  and  $\delta R_\perp$  represent tangential and normal variations, respectively. However,  $\delta R_\perp$  contributes to the bulk shape equation, whereas  $\delta R_\parallel^\mu$  to the boundary conditions [31]. The minimization of  $F_{\text{el}}$  with respect to shape is [32]

$$\frac{\delta F_{\text{el}}}{\delta R_\perp} = \frac{\delta F_\alpha}{\delta R_\perp} + \frac{\delta F_{\text{H}}}{\delta R_\perp} = 0 \quad (1.17)$$

where,

$$\frac{\delta F_\alpha}{\delta R_\perp} = K_\alpha (K^{\mu\nu} \psi_{\mu\nu} + H \phi)$$

$$\frac{\delta F_{\text{H}}}{\delta R_\perp} = \frac{\kappa}{2} [\nabla^2 H + 2(H - H_0)(H^2 - K + H H_0)] - 2\sigma H$$

with the definitions  $\psi_{\mu\nu} = \nabla_\mu \nabla_\nu \chi - (\nabla_\mu \chi)(\nabla_\nu \chi)$ ,  $\phi = (\nabla \chi)^2 - 2\nabla^2 \chi$  and  $K^{\mu\nu}$  is curvature tensor. For minimal symmetric bilayer membranes, mean ( $H$ ) and spontaneous curvature ( $H_0$ ) are zero. Thus, the shape equation Eq. 1.17 reduces

to

$$K^{\mu\nu}\psi_{\mu\nu} = 0 \tag{1.18}$$

These equilibrium equations are essential to study the membranes with orientational order and to lay the foundation for the following chapters in this thesis. The thesis work is divided into two parts. Part-I addresses the stability of singular, topological wall defects on spheres (Chapters 2), catenoids (Chapters 3), and helicoids (Chapters 4). In Part-II (Chapters 5, 6) we discuss the role of topological defects in determining the observed morphologies of polymer crystallites. These topological defects are point defects with *soliton*-type wall configurations. In contrast to Part-I, the soliton-type wall configuration is not a singular defect line in order parameter field rather a domain wall separating two domains with continuous, smooth deformations in order parameter field.



## Part I

# Stability of singular, topological wall disclinations on curved membranes



## Chapter 2

# Wall disclinations on spheres

### 2.1 Introduction

In Part-I of this thesis (Chapters 2, 3, 4), we address the stability of singular, *topological wall defects* (line defects in 2-dimensions) on spheres, catenoids, and helicoids. This work is done with the collaboration of Dr. Jaya Kumar A (IISc, Bengaluru, India). To begin with we consider a spherical surface with in-plane orientational order, such as nematic order.

The Poincaré-Hopf index theorem [25, 26] strikingly demonstrates the remarkable interplay between curvature of a surface, and frustration of orientational order on it. According to this theorem, a sphere with in-plane orientational order must have a singular, isolated point disclination of index  $s = 2$ , or isolated disclinations with total index  $s_T = 2$ . The study of topological defects in systems of spherical topology, such as vesicles with in-plane orientational order, is important for investigating the interplay between geometry, topology, and elasticity, and for its potential applications in materials science.

Lubensky and Prost [33] have investigated equilibrium positions of point disclinations on orientationally ordered rigid spheres. Due to repulsive interactions between like disclinations, the shape of *deformable* spherical vesicles is altered. Equilibrium shapes of deformable vesicles are discussed in [16]. Thickness effects in spherical nematic *shells* plays an important role in determining the nature of defects on the sphere. As the thickness of the shell increases, the tetrahedral configuration of four half-index disclinations (which is the ground state for “zero thickness” shells) becomes unstable, and a three-dimensional “escape

configuration” composed of two pairs of half-hedgehogs becomes energetically favorable [29].

Disclination cores on spherical particles such as micron-scale colloidal particles coated with liquid crystals can be functionalised to create “super-atoms” with directional bonds [34]. This opened up new possibilities such as self-assembly of super-atoms by linking across functionalised groups (including biomolecules such as DNA), and the development of atomic chemistry at micron scales. Rigid spheres have been prepared by molecular coating of ordered, tilted monolayers on metal nanospheres [35], leading to the antipodal configuration of a source-sink pair of disclinations of index  $s = 1$  each. These divalent super-atoms spontaneously form long one-dimensional chains. Thin nematic shells consisting of a nematic drop containing a smaller aqueous drop have been obtained in double emulsions [36]. These can be engineered to imitate  $sp$ -,  $sp^2$ -, and  $sp^3$  geometries of carbon bonds. Deformable vesicles with orientational order can form facets. These fascinating possibilities have led to rapid advances in theoretical and experimental studies [29, 37, 38, 39, 40] in this field.

In our work, we study the energetics and stability of topological wall defects (line defects in 2-dimensions) in fluid membranes with  $n$ -atic orientational order. Topological arguments show that singular wall defects in two- and three dimensional ordered systems are unstable because they can be made to disappear by making local changes in the orientational order [9, 3]. In three dimensions, removal of disclinations lines with index  $s = 1$  via “escape” of the nematic director in the third dimension [9, 10, 3, 41, 42] is well known. However, close to nematic-smectic transition the bend elastic constant diverges, the escape configuration has a larger free energy than that of the line disclination of index 1, and the disclination line is stabilised. We show that singular wall defects can be stabilized on a sphere because of its Gaussian curvature, and not because of boundary conditions, externally imposed fields, or divergences in certain elastic constants. They are stable close to the order-disorder transition, over a finite range of a dimensionless parameter  $\eta$ . The parameter  $\eta$  is the ratio of basic free energy scales corresponding to the destruction of order in defect cores to that of elastic deformation outside the core [43].

## 2.2 Ginzburg-Landau theory

Our analysis is based on a Ginzburg-Landau type model that extends the Nelson-Peliti (spin connection) elasticity theory of orientationally ordered fluid membranes [1, 2]. The xy model elastic free energy does not take into account changes in the magnitude of the orientational order parameter. In the presence of singular, topological defects, magnitude of the order parameter is not uniform (See Sec. 1.2). In investigating the energetics and structure of topological defects it is essential to take gradients in the magnitude of the orientational order parameter into account. This is best accomplished by using the Ginzburg-Landau theory for a complex,  $n$ -atic order parameter  $\psi = \psi(\mathbf{x}) = |\psi(\mathbf{x})| e^{i\alpha(\mathbf{x})}$  [16]. Here, the angle  $\alpha$  is measured modulo  $2\pi/n$  with respect to a *local* orthonormal frame  $(\hat{e}_1(\mathbf{x}), \hat{e}_2(\mathbf{x}))$ .

The Ginzburg-Landau free energy density of orientationally ordered surfaces ( $f_{\text{GL}}$ ) is given by [16]

$$f_{\text{GL}} = \frac{r}{2} |\psi|^2 + \frac{u}{4} |\psi|^4 + \frac{k}{2} |(\boldsymbol{\partial} - i \mathbf{A}) \psi|^2, \quad (2.1)$$

where  $r = r_0(T - T_c)$ ,  $T$  and  $T_c$  are the temperature, and the critical temperature respectively, and  $u$  is assumed to be temperature independent. The term with coefficient  $k$  describes the elastic free energy of deformations within the “one-constant” approximation [9, 10, 3]. The symbol  $\boldsymbol{\partial}$  represents the flat-space gradient operator, and  $\mathbf{A}(\mathbf{x})$  is the local gauge field (the spin connection) that corrects the flat-space gradient by accounting for membrane curvature. In the term with coefficient  $k$ , complex conjugates are contracted using the metric tensor. The free energy  $F_{\text{GL}} = \int f_{\text{GL}} d\mathcal{A}$ , where the area element  $d\mathcal{A} = \sqrt{g} dx^1 dx^2$ , and  $g$  is the determinant of the metric tensor  $g_{\mu\nu}$ . The free energy  $F_{\text{GL}}$  is analogous to that of the Ginzburg-Landau theory of type-II superconductors [44]. In superconductors the complex order parameter is coupled to the electromagnetic vector potential  $\mathbf{A}$ , whereas in orientationally ordered membranes this coupling is via the “*geometric* vector potential” (spin connection).

### 2.2.1 Equations of equilibrium

The free energy  $F_{\text{GL}}$  has contributions from establishment of order, and elastic deformations in the order parameter. The former sets up the magnitude of the

order parameter and contributes to the condensation free energy density ( $f_C$ ). By definition,  $f_C$  is the free energy cost per unit area for destruction of orientational order. It plays a pivotal role in finding the optimal core-sizes of topological defects [3]. Within mean field theory the magnitude of order parameter  $|\psi_0| = \sqrt{-r/u}$ , and  $f_C = r^2/(4u)$ .

For surfaces of fixed shape (and therefore fixed  $\mathbf{A}$ ) that we consider, variational minimisation of the functional  $F_{\text{GL}}$  with respect to  $\alpha(\underline{x})$  and  $|\psi(\underline{x})|$  leads to the full set of equations of equilibrium.

$$\frac{\delta F_{\text{GL}}}{\delta \alpha} = -k \nabla \cdot [|\psi|^2 (\partial \alpha - \mathbf{A})] = 0. \quad (2.2)$$

Here  $\nabla \cdot$  represents covariant divergence [26]. Within mean-field theory  $|\psi|$  is uniform. Thence Eq. 2.2 reduces to the  $\alpha$ - equation (Eq. 1.13) with the modification  $K_\alpha = k |\psi_0|^2$ .

$$\frac{\delta F_{\text{GL}}}{\delta |\psi|} = [r + k (\partial \alpha - \mathbf{A})^2] |\psi| + u |\psi|^3 - k \nabla^2 |\psi| = 0, \quad (2.3)$$

where  $(\partial \alpha - \mathbf{A})^2 \equiv g^{\mu\nu} (\partial_\mu \alpha - A_\mu) (\partial_\nu \alpha - A_\nu)$  and the Laplace-Beltrami operator  $\nabla^2 \equiv (1/\sqrt{g}) \partial_\mu (\sqrt{g} g^{\mu\nu} \partial_\nu)$ . We define  $\Upsilon = |\psi|/|\psi_0|$  such that Eq. 2.3 takes the simple form as follows [45]

$$\frac{\delta F_{\text{GL}}}{\delta \Upsilon} = [1 - \xi^2 (\partial \alpha - \mathbf{A})^2] \Upsilon - \Upsilon^3 + \xi^2 \nabla^2 \Upsilon = 0 \quad (2.4)$$

where correlation length  $\xi = \sqrt{-k/r} \sim (\Delta T)^{-1/2}$ .

The above equation is essential for studying variation of order parameter magnitude around the defect core. However, for simplicity, we assume that the core of size  $\vartheta(\xi)$  is completely disordered. In other words,  $|\psi| = 0$  in the core and takes the mean-field value outside the core. In what follows, we study the stability of wall disclinations using this approximation [3, 33].

## 2.3 The elastic free energy

The elastic part of the Ginzburg-Landau free energy density (Eq. 2.1) is

$$f_{\text{el}} = \frac{1}{2} K_{\alpha} (\boldsymbol{\partial}\alpha - \mathbf{A})^2 = \frac{1}{2} K_{\alpha} (\partial_{\mu}\alpha - A_{\mu})(\partial^{\mu}\alpha - A^{\mu}), \quad (2.5)$$

where  $K_{\alpha} = k|\psi_0|^2$  in the mean field approximation. Minimisation of the elastic free energy  $F_{\text{el}} = \int f_{\text{el}} d\mathcal{A}$  leads to the  $\alpha$ -equation discussed in Chapter-1 (Eq. 1.13). We use the Airy function formalism (See Sec. 1.5.2) to study the energetics. In terms of the stress function  $\chi$ , the elastic free energy density (Eq. 2.5) can be written as

$$f_{\text{el}} = \frac{1}{2} K_{\alpha} (\boldsymbol{\partial}\chi)^2 = \frac{1}{2} K_{\alpha} (\partial_{\mu}\chi)(\partial^{\mu}\chi). \quad (2.6)$$

Making the simplifying assumption that order is destroyed over the entire core region, the condensation free energy  $F_{\text{C}} = \int f_{\text{C}} d\mathcal{A}$ , where the integral is over the core region [3]. Thus the total free energy density of our model is  $F_{\text{T}} = F_{\text{el}} + F_{\text{C}}$ .

### 2.3.1 The Coulomb gas model

For a shape of Gaussian curvature ( $K(\underline{\mathbf{x}})$ ), given disclination density ( $\mathcal{S}(\underline{\mathbf{x}})$ ) the exact solution to the compatibility condition ( Eq. 1.14) can be obtained from Green's function approach. The Green's function  $G(\underline{\mathbf{x}}, \underline{\mathbf{x}}')$  for the surface satisfies the Laplace equation

$$\nabla_{\underline{\mathbf{x}}}^2 G(\underline{\mathbf{x}}, \underline{\mathbf{x}}') = \frac{\delta(\underline{\mathbf{x}} - \underline{\mathbf{x}}')}{\sqrt{g}} \quad (2.7)$$

where  $\delta(\underline{\mathbf{x}} - \underline{\mathbf{x}}')$  is the 2-dimensional Dirac delta function.

The exact solution for the stress function  $\chi$  is given by

$$\chi(\underline{\mathbf{x}}) = \int G(\underline{\mathbf{x}}, \underline{\mathbf{x}}') \rho(\underline{\mathbf{x}}') d\mathcal{A}' \quad (2.8)$$

where the source function  $\rho(\underline{\mathbf{x}}) = K(\underline{\mathbf{x}}) - \mathcal{S}(\underline{\mathbf{x}})$ . Substituting for  $\chi$  in Eq. 2.6, and with some algebraic manipulations we get the elastic free energy as

$$F_{\text{el}} = -\frac{1}{2} K_{\alpha} \iint \rho(\underline{\mathbf{x}}) G(\underline{\mathbf{x}}, \underline{\mathbf{x}}') \rho(\underline{\mathbf{x}}') d\mathcal{A} d\mathcal{A}', \quad (2.9)$$

This form of the elastic free energy is very much useful to investigate the interaction potentials of defects on the curved surfaces [19]. The elastic free energy Eq. 2.9 can be written as  $F_{\text{el}} = -(1/2) K_\alpha (F_{KK} - 2F_{K\mathcal{S}} + F_{\mathcal{S}\mathcal{S}})$ , where

$$\begin{aligned} F_{KK} &= \iint K(\underline{\mathbf{x}}) G(\underline{\mathbf{x}}; \underline{\mathbf{x}}') K(\underline{\mathbf{x}}') d\mathcal{A} d\mathcal{A}', \\ F_{K\mathcal{S}} &= \iint K(\underline{\mathbf{x}}) G(\underline{\mathbf{x}}; \underline{\mathbf{x}}') \mathcal{S}(\underline{\mathbf{x}}') d\mathcal{A} d\mathcal{A}', \text{ and} \\ F_{\mathcal{S}\mathcal{S}} &= \iint \mathcal{S}(\underline{\mathbf{x}}) G(\underline{\mathbf{x}}; \underline{\mathbf{x}}') \mathcal{S}(\underline{\mathbf{x}}') d\mathcal{A} d\mathcal{A}'. \end{aligned}$$

The interaction potential energy of given defect configuration ( $\mathcal{S}$ ) is, by definition,

$$F_{\text{int}} = \frac{1}{2} K_\alpha (2F_{K\mathcal{S}} - F_{\mathcal{S}\mathcal{S}}). \quad (2.10)$$

With this background we discuss the procedure followed in calculating the free energies of point- and wall defects on a sphere of radius  $a$ . For vector order the free energy of the antipodal configuration of (index  $s = 1$ ) point disclinations has been obtained for small core-sizes  $r_c$ , where the dimensionless cutoff  $\zeta = r_c/a \ll 1$  [33]. A larger core reduces the elastic free energy  $F_{\text{el}}$ , but increases the condensation free energy. In investigating the energetics and stability of point- as well as wall defects for  $n$ -atic order the determination of optimal core-sizes, without the restriction  $\zeta \ll 1$ , is crucial. In what follows, we minimise the dimensionless total free energies  $\tilde{F}_{\text{T}} = F_{\text{T}}/K_\alpha$  with respect to  $\zeta$  to obtain the optimal core size. The minimised total free energy, and optimal core sizes are functions of a dimensionless parameter  $\eta = f_{\text{C}} a^2 / K_\alpha$ . Within the mean field theory,  $\eta \sim (T_c - T)$ . To compare total free energies and stability ranges of various disclination configurations, it is convenient to choose the dimensionless condensation energy  $4\pi\eta$  (corresponding to the destruction of order over the entire sphere) as the common reference of free energy. Thus minimised free energy  $\mathcal{F} = \tilde{F}_{\text{T}} - 4\pi\eta$ . In the next Section, we focus on vector order on a sphere.

## 2.4 Vector order

Parametrisation of a sphere with radius  $a$  is  $\mathbf{R}(\theta, \phi) = \{a \cos \phi \sin \theta, a \sin \phi \sin \theta, a \cos \theta\}$ ,  $0 \leq \theta < \pi$  and  $0 \leq \phi < 2\pi$ . The Gaussian curvature  $K = 1/a^2$  and mean curvature  $H = -1/a$ , and the components of the metric tensor are  $g_{\theta\theta} = a^2$ ,  $g_{\phi\phi} = a^2 \sin^2 \theta$ ,  $g_{\theta\phi} = g_{\phi\theta} = 0$ . The determinant of metric tensor  $g = a^4 \sin^2 \theta$ .

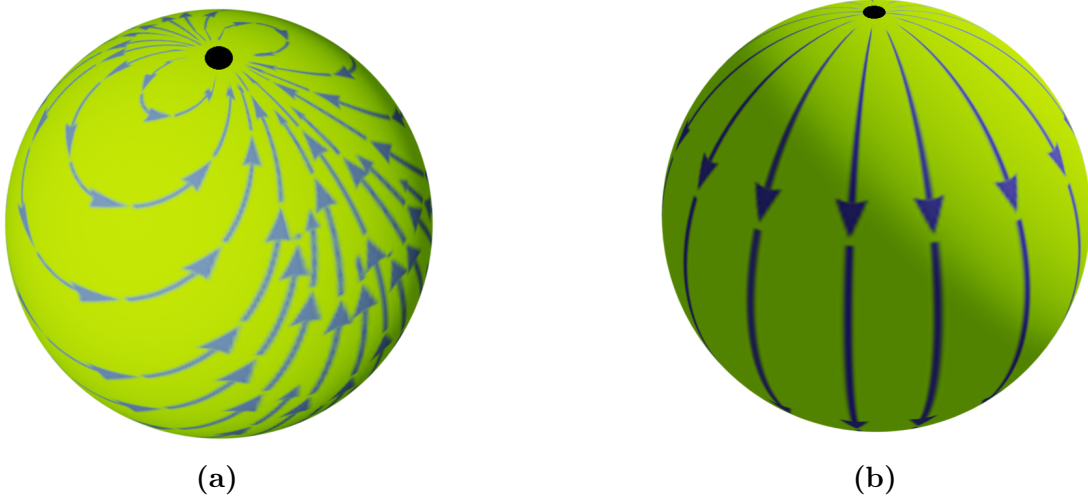


**Figure 2.1:** Vectorial order- Point disclinations: (a) Single point disclination of index  $s = 2$ . (b) Antipodal configuration-Two point disclinations, each of index  $s = 1$  at the poles.

Let us consider a unit tangent vector field  $\hat{\mathbf{m}}(\theta, \phi) = \cos \alpha(\theta, \phi) \hat{\mathbf{e}}_\theta + \sin \alpha(\theta, \phi) \hat{\mathbf{e}}_\phi$  on a sphere. This choice of coordinate system gives  $A_\theta = 0$ ,  $A_\phi = -\cos \theta$ .

It is widely known that the ground-state texture of rigid spheres with vector order has two antipodal disclinations of index  $s = 1$  each. We now discuss the antipodal configuration in section 2.4.1 below, followed by the equatorial configuration (Sec. 2.4.2), and the two-wall configuration (Sec. 2.4.3)

### 2.4.1 Antipodal configuration

For the simplest antipodal configuration,  $\alpha = 0$ , and streamlines of  $\hat{\mathbf{m}}$  follow longitudes on the sphere (See Fig. 2.1(b)). For more general defect configurations, such as a single  $s = 2$  point disclination, and wall disclinations, we use stereographic-projection approach to obtain the texture of the  $\alpha$ -field. Stereographic projection is particularly useful in plotting the texture as it eliminates the coordinate singularities at poles arising from  $(\hat{\mathbf{e}}_\theta, \hat{\mathbf{e}}_\phi)$  basis (See Appendix A).

Setting  $\alpha = 0$  in Eq. 2.5 gives the elastic free energy density of antipodal configuration

$$f_{\text{el}}^{(\text{ap})} = \frac{K_\alpha}{2a^2} \cot^2 \theta, \quad (2.11)$$

where the superscript (ap) stands for antipodal point disclinations. It has singularities at  $\theta = 0, \pi$ . To calculate the elastic free energy of antipodal point defects, we use circular cores of core radius  $r_c$  for both disclinations. The elastic free energy of the vectorial texture outside the core region is

$$\begin{aligned} F_{\text{el}}^{(\text{ap})} &= 2\pi \int_{\zeta}^{\pi-\zeta} f_{\text{el}}^{(\text{ap})} a^2 \sin \theta \, d\theta \\ &= 2\pi K_{\alpha} [\log \cot(\zeta/2) - \cos \zeta], \end{aligned} \quad (2.12)$$

where the dimensionless cutoff  $\zeta = r_c/a$ . For small  $r_c$  this result reduces to the result of Ref. [33]. We note that  $F_{\text{el}}^{(\text{ap})}$  depends solely on  $\zeta$ , and diverges logarithmically as  $\zeta \rightarrow 0$ .

The condensation free energy is

$$\begin{aligned} F_{\text{C}}^{(\text{ap})} &= 2 \times 2\pi \int_0^{\zeta} f_{\text{C}} a^2 \sin \theta \, d\theta \\ &= 4\pi a^2 f_{\text{C}} (1 - \cos \zeta). \end{aligned} \quad (2.13)$$

For  $\zeta \ll 1$ ,  $F_{\text{C}}^{(\text{ap})} \sim 2\pi r_c^2 f_{\text{C}}$ . Minimisation of the total free energy  $F_{\text{T}} = F_{\text{el}} + F_{\text{C}}$  gives the optimum core size for antipodal points (See Fig. 2.2).

$$\zeta^{(\text{ap})} = 2 \arctan[p(\eta)/q(\eta)], \quad (2.14)$$

where  $p(\eta) = [1 + 2\eta - \sqrt{2\eta(1 + 2\eta)}]^{1/2}$ , and  $q(\eta) = [1 + 2\eta + \sqrt{2\eta(1 + 2\eta)}]^{1/2}$ . We note that, as  $\eta \rightarrow 0$ ,  $\zeta \rightarrow \pi/2$  implying that full sphere is disordered.

The minimised total (elastic + condensation), dimensionless free energy of the antipodal configuration in units of  $K_{\alpha}$  is

$$\mathcal{F}^{(\text{ap})} = 2\pi[2\eta - \sqrt{2}h(\eta) + \operatorname{arctanh}(\sqrt{2}\eta/h(\eta))] - 4\pi\eta, \quad (2.15)$$

where  $h(\eta) = \sqrt{\eta(1 + 2\eta)}$ , and we have taken the dimensionless condensation free energy  $4\pi\eta$  for destruction of order over the entire sphere as the reference. The plot of  $\mathcal{F}^{(\text{ap})}$  as a function of  $\eta$  is shown in Fig. 2.3.

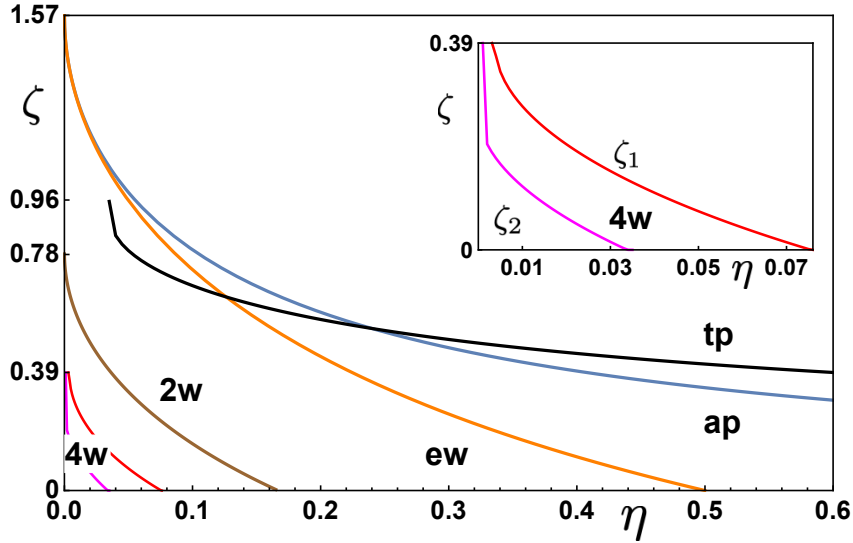


**Figure 2.2:** Optimised core sizes: The symbols ap, and tp represent the antipodal (index  $s = 1$  each) and tetrahedral (index  $s = 1/2$  each) configurations of point disclinations; ew, 2w, and 4w refer to the equatorial (index  $s = 2$ ), two-wall (index  $s = 1$  each), and four-wall (index  $s = 1/2$  each) configurations respectively. The inset depicts the two core sizes required to minimise the total free energy for the 4w-configuration. Order is completely destroyed at  $\zeta = \{\pi/8, \pi/4, \pi/2, \pi/2\}$  for the {4w, 2w, ew, ap}- configurations respectively. Above  $\zeta = (1/2) \arccos(-1/3) \simeq 0.96$ , cores of neighboring disclinations of the tp-configuration overlap each other (see the text).

### 2.4.2 Equatorial wall disclination

We now consider a singular, equatorial wall defect (at  $\theta = \pi/2$ ), defined by the disclination density

$$\mathcal{S}^{(\text{ew})} = \frac{S_0}{2\pi\sqrt{g}} \delta\left(\theta - \frac{\pi}{2}\right), \quad (2.16)$$

where the superscript (ew) stands for equatorial wall and  $\delta(\theta)$  is the Dirac delta function. Thus  $\int_0^{2\pi} d\phi \int_0^\pi \mathcal{S}^{(\text{ew})} \sqrt{g} d\theta = S_0$ , where index of the wall  $s = S_0/(2\pi)$  is as yet undetermined. The general solution to the compatibility condition (Eq. 1.14) is

$$\chi(\theta) = -c_1 \log \tan\left(\frac{\theta}{2}\right) - \log \sin \theta + s[\Theta\left(\theta - \frac{\pi}{2}\right) - 1] \log \cot \frac{\theta}{2} + c_2, \quad (2.17)$$

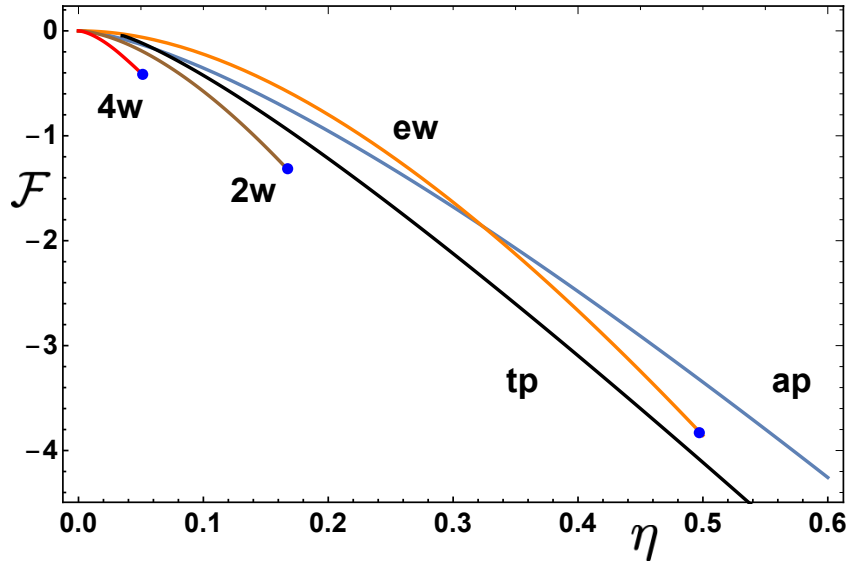


**Figure 2.3:** Minimised free energy  $\mathcal{F} = F_T - 4\pi\eta$ : We set the reference of the total free energy to the condensation energy  $4\pi\eta$  of the entire sphere. The dots indicate the  $\eta$ -values beyond which wall defects are unstable ( $\zeta(\eta) = 0$ ), see Fig. 2.2. The symbols ap, and tp represent the antipodal (index  $s = 1$  each) and tetrahedral (index  $s = 1/2$  each) configurations of point disclinations; ew, 2w, and 4w refer to the equatorial (index  $s = 2$ ), two-wall (index  $s = 1$  each), and four-wall (index  $s = 1/2$  each) configurations respectively.

where the symbol  $\Theta$  is the Heaviside theta function, and  $c_1, c_2$  are constants. By definition,  $\Theta(x) = 1$  if  $x > 0$ , and  $\Theta(x) = 0$  if  $x < 0$ . The Heaviside  $\Theta$  in Eq. 2.17 has important consequences for the stability of wall defects, as discussed below. Setting  $c_2 = 0$ , we exploit the symmetry  $\chi(\theta) = \chi(\pi - \theta)$  to obtain  $c_1 = -S_0/(4\pi)$ . Note that  $S_0$  is as yet undetermined. To ensure that there are no point disclinations of index  $s = 1$  each (from coordinate singularities) at the north and south poles, we investigate the behavior of  $\partial_\theta \chi(\theta)$  at the poles. We note that  $\lim_{\theta \rightarrow 0} \partial_\theta \chi(\theta)$  as well as  $\lim_{\theta \rightarrow \pi} \partial_\theta \chi$  go to infinity unless  $S_0 = 4\pi$ . With  $S_0 = 4\pi$ , both these limits go to zero. This in turn ensures that  $s = 2$ , vindicating the Poincaré-Hopf index theorem [46]. Setting  $c_1 = -S_0/(4\pi) = -1$  guarantees that there are no point disclinations at the north and south poles. The solution to the compatibility condition is

$$\chi^{(ew)} = 2 \left[ \Theta \left( \theta - \frac{\pi}{2} \right) \log \cot \frac{\theta}{2} - \log \left( \sqrt{2} \cos \frac{\theta}{2} \right) \right]. \quad (2.18)$$

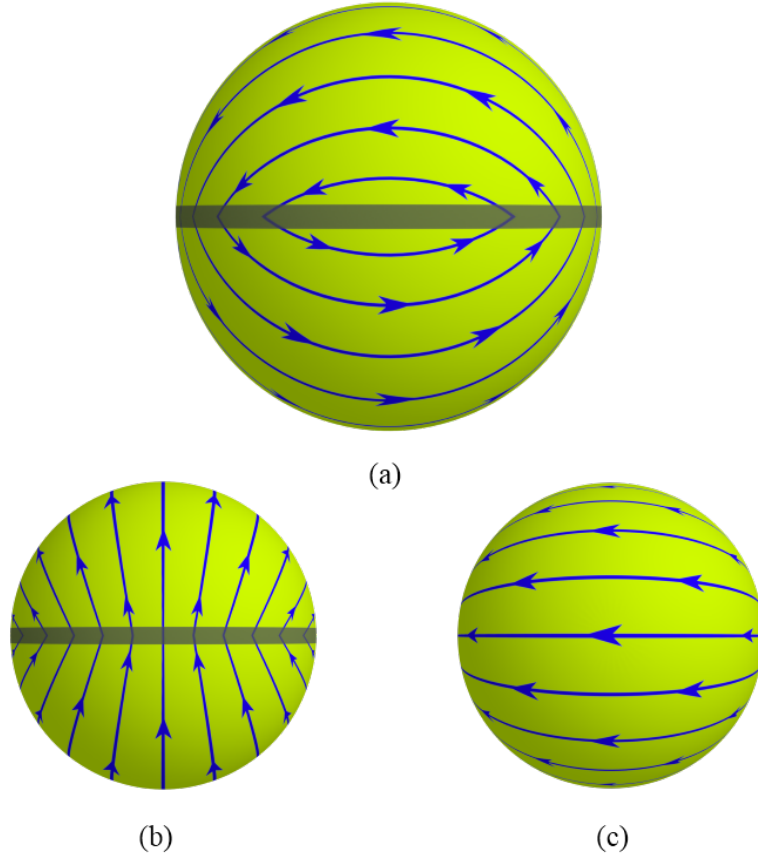


**Figure 2.4:** Equatorial wall: (a) Side ( $\theta = \pi/2$ ,  $\phi = \pi/2$  at the center) view of the index  $s = 2$ , equatorial wall. The directed lines are the streamlines of the vector field. The shaded region represents the disordered core, within which vector order is completely destroyed, and cannot be assigned a direction. The full field, as given by Eq. 2.19, (including that shown within the core region) corresponds to a wall with zero core-size. Rounding off the slope singularity of the field at the equator, the wall defect of zero core-size transforms into the antipodal configuration of a pair of index  $s = 1$  point disclinations. (b) Front view ( $\theta = \pi/2$ ,  $\phi = 0$  at the center). (c) Top view, showing that the polar regions are free of point disclinations.

We have thus constructed a wall defect with index  $s = 2$ , as demanded by the Poincaré-Hopf theorem extended to non-isolated zeros. In terms of  $\alpha$ , measured in the local orthonormal frame  $(\hat{e}_\theta(\theta, \phi), \hat{e}_\phi(\theta, \phi))$ , the solution Eq. 2.18 is particularly simple (Fig. 2.4):

$$\alpha^{(\text{ew})} = \begin{cases} -\phi & \text{if } \theta < \pi/2 \\ \phi & \text{if } \pi > \theta > \pi/2, \end{cases} \quad (2.19)$$

Notice that  $\oint_0^{2\pi} d\alpha_{(\text{lh})} - \oint_0^{2\pi} d\alpha_{(\text{uh})} = 2\pi \times 2 = 4\pi$ , where  $\alpha_{(\text{lh})}$  and  $\alpha_{(\text{uh})}$  refer to the lower and the upper hemisphere respectively, with the integrals taken in the anti-clockwise sense around the outward normal at the respective poles. This result is easily generalised to walls having other indices.

Use of the cut-offs in finding elastic energy of equatorial wall is essential as linear elasticity breaks down near the core. Therefore, we choose dimensionless, one-sided core size  $\zeta$  such that width of the equatorial wall is  $2\zeta$  (in units of  $a$ ). Substituting for the exact solution for  $\chi$  (Eq. 2.18) in free energy density expression Eq. 2.6, we get the elastic free energy density of the equatorial wall configuration as follows

$$f_{\text{el}}^{(\text{ew})} = \frac{K_\alpha}{2a^2} \left[ \csc \theta \left\{ \cos \theta - 1 + 2\Theta\left(\theta - \frac{\pi}{2}\right) \right\} + 4 \delta\left(\theta - \frac{\pi}{2}\right) \log \tan \frac{\theta}{2} \right]^2. \quad (2.20)$$

We note that the term with Heaviside  $\Theta$  in Eq. 2.18, when substituted in  $f_{\text{el}}[\chi]$  Eq. 2.6 leads to a term involving  $(\delta[\theta - (\pi/2)])^2$  in the integrand. With  $\zeta = 0$  at, or within the limits of integration, the integral is, strictly speaking, undefined. However it diverges as  $1/\zeta$ , in contrast to the logarithmic divergence encountered in the case of antipodal point disclinations. This can be seen by putting  $\theta = 0$  in  $\delta(\theta) = (1/(2\pi)) \int_{-\infty}^{\infty} e^{ik\theta} dk$ , and setting the ultraviolet cutoff to  $2\pi/\zeta$ . We therefore expect the index  $s = 2$  wall to become unstable as  $\zeta$  approaches the molecular size, within the coarse-grained elasticity theory that we have used. This is borne out by the minimisation of the total free energy discussed below. Away from the core, the elastic free energy of the equatorial wall is

$$\begin{aligned} F_{\text{el}}^{(\text{ew})} &= 2\pi \int_0^{\pi/2-\zeta} f_{\text{el}}^{(\text{ew})} \sqrt{g} d\theta + 2\pi \int_{\pi/2+\zeta}^{\pi} f_{\text{el}}^{(\text{ew})} \sqrt{g} d\theta \\ &= 2\pi K_\alpha \left[ \sin \zeta - 4 \log \sin\left(\frac{\zeta}{2} + \frac{\pi}{4}\right) - 1 \right]. \end{aligned} \quad (2.21)$$

The condensation free energy is given by

$$\begin{aligned} F_{\text{C}}^{(\text{ew})} &= 2\pi \int_{\pi/2-\zeta}^{\pi/2+\zeta} f_{\text{C}} a^2 \sin \theta d\theta \\ &= 4\pi a^2 f_{\text{C}} \sin \zeta. \end{aligned} \quad (2.22)$$

The core size  $\zeta^{(\text{ew})}$  that minimises the total free energy  $\mathcal{F}^{(\text{ew})} = F_{\text{T}}^{(\text{ew})} - 4\pi\eta$  of the equatorial wall defect is given below, and is plotted in Fig. 2.2 as a function of  $\eta$ .

$$\zeta^{(\text{ew})} = \arctan \frac{1 - 2\eta}{2\sqrt{2\eta}}. \quad (2.23)$$

We find that  $\zeta^{(\text{ew})} = 0$  at  $\eta = 1/2$ . Moreover, it crosses zero and is negative above  $\eta = 1/2$ , which is unphysical. Thus, the singular equatorial wall is stable only for  $0 < \eta < 1/2$ .

The minimised, dimensionless total free energy of the equatorial wall in units of  $K_{\alpha}$ , with reference to the dimensionless condensation free energy  $4\pi\eta$  (Fig. 2.3) is

$$\mathcal{F}^{(\text{ew})} = 4\pi [\log(1 + 2\eta) - 2\eta]. \quad (2.24)$$

As in the case of antipodal point disclinations,  $\mathcal{F}^{(\text{ew})}$  depends only on  $\eta$ . We note that all the calculations of energetic of point and wall disclinations are based on the approximation that magnitude of order parameter is zero in the core, and non zero away from the core. There is step like discontinuity across the core. In Appendix A, we study the magnitude of order parameter for the equatorial wall disclination.

For the sake of generality, we study the interaction potential (Eq. 2.10) of a wall disclination of index  $s = 2$  as a function of its position  $\theta = \omega$ . The corresponding disclination density is  $\mathcal{S}^{(2\text{w})} = \frac{2}{\sqrt{g}}\delta(\theta - \omega)$ . The analytical expression for the interaction potential as defined by Eq. 2.10 is (Fig. 2.5(a))

$$\mathcal{F}^{(\text{int})} = 2\pi[-1 + \log 4 - 2\log(\sin \omega)]. \quad (2.25)$$

### 2.4.3 Two wall disclinations

The equatorial wall is not necessarily the minimum energy configuration over its entire range of stability. For vector-, as well as nematic order it can split into two walls with index  $s = 1$ . For generality, we consider two walls with index  $s_1$  and  $s_{-1}$  respectively, placed at  $\theta = (\omega_1^{(2\text{w})}, \omega_2^{(2\text{w})} = \pi - \omega_1^{(2\text{w})})$ . The disclination density is given by

$$\mathcal{S}^{(2\text{w})} = \frac{s_1}{\sqrt{g}}\delta(\theta - \omega_1^{(2\text{w})}) + \frac{s_{-1}}{\sqrt{g}}\delta(\theta - \omega_2^{(2\text{w})}), \quad (2.26)$$

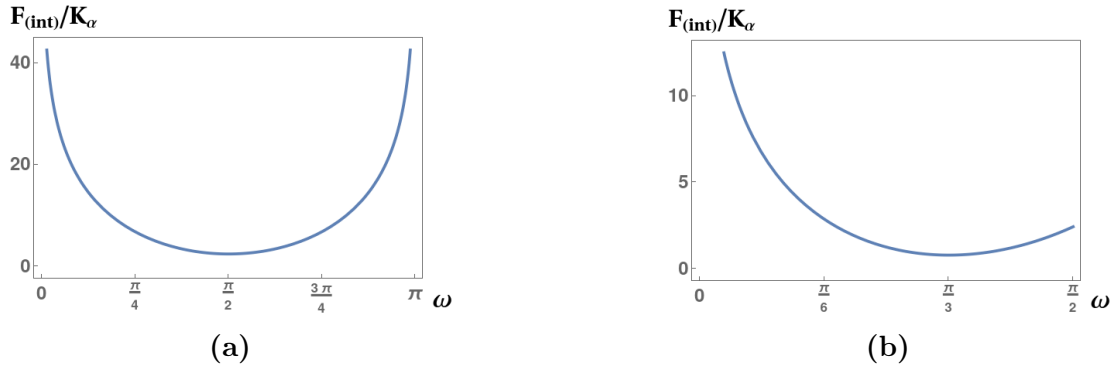


**Figure 2.5:** Interaction potential energy (dimensionless)  $\mathcal{F}^{(\text{int})} = F_{(\text{int})}/K_\alpha$ : (a) For the single wall disclination of index  $s = 2$ . Clearly, the equatorial configuration ( $\omega = \pi/2$ ) has the minimum energy (b) For the two wall configuration with  $s = 1$  each. The function has minimum at  $\omega = \pi/3$  rad (See Sec. 2.4.3).

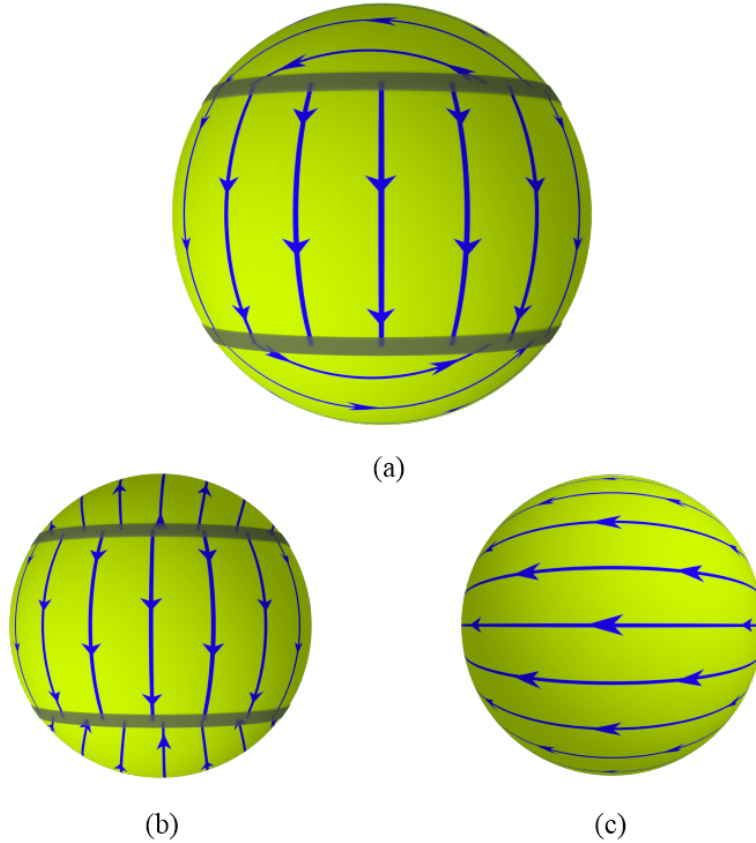


**Figure 2.6:** Two-wall configuration: (a) Side view. The vector field between the two index  $s = 1$  walls follows the longitudes. The two-wall configuration degenerates to the antipodal configuration by smoothly sliding the walls towards the respective poles. (b) Front view. (c) Top view.

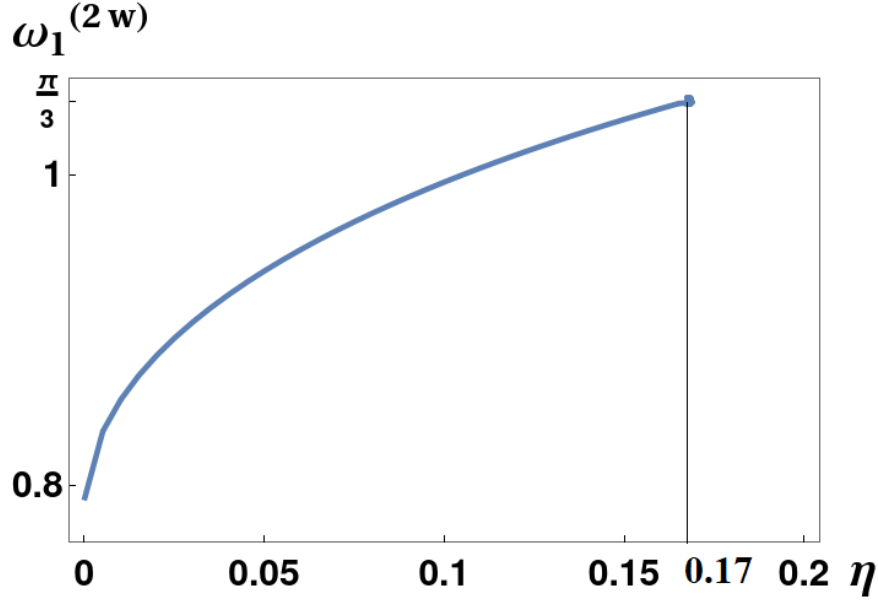


**Figure 2.7:** Equilibrium position of two wall disclinations: The plot of  $\omega_1^{(2w)}$  vs  $\eta$ . The dot in the plot represents the limit of stability.

where  $\omega_1^{(2w)} < \pi/2$ . The solution to the compatibility condition Eq. 1.14 with the boundary conditions ( $\chi(\pi - \theta) = \chi(\theta)$ ,  $\lim_{\theta \rightarrow 0} \partial_\theta \chi(\theta)$  is finite) demands that  $s_1 = s_{-1} = 1$ . Thus, the total index is  $s = 2$ , as dictated by the Poincaré-Hopf index theorem. The exact solution for the  $\chi^{(2w)}$  is

$$\begin{aligned} \chi^{(2w)} = & \log\left(\tan \frac{\theta}{2}\right) - \log(\sin \theta) + \Theta(\theta - \omega_1^{(2w)}) \log\left(\cot \frac{\theta}{2} \tan \frac{\omega_1^{(2w)}}{2}\right) \\ & + \Theta(\theta + \omega_1^{(2w)} - \pi) \log\left(\cot \frac{\theta}{2} \cot \frac{\omega_1^{(2w)}}{2}\right). \end{aligned} \quad (2.27)$$

In terms of the  $\alpha$ -field, the solution to the compatibility condition (Eq. 1.14) for the two-wall configuration (Fig. 2.6) is simple;

$$\alpha^{(2w)} = \begin{cases} -\phi & \text{if } 0 \leq \theta < \omega_1^{(2w)} \\ 0 & \text{if } \omega_1^{(2w)} < \theta < \omega_2^{(2w)} \\ \phi & \text{if } \omega_1^{(2w)} < \theta < \pi. \end{cases} \quad (2.28)$$

Following the same procedure as the one used above for the equatorial wall, we find numerically optimal core sizes and minimised total free energy of the

two-wall configuration (plotted as a function of  $\eta$  in the Fig. 2.2 and Fig. 2.3 respectively). The two-wall configuration is stable only for  $0 < \eta < 0.17$ . For optimal positions of two-wall configuration, we find that the angle  $\omega_1^{(2w)}(\eta)$  is a monotonic increasing function with  $\omega_1^{(2w)}(\eta = 0) = 0.9 \simeq \pi/4$ , and  $\omega_1^{(2w)}(\eta = 0.17) = \pi/3 \simeq 1.05$  (See Fig 2.7). As  $\eta$  approaches the limit of stability (cutoff  $\zeta^{(2w)} \rightarrow 0$ ), the total (integrated) Gaussian curvature of the spherical region between the two walls  $K_T \rightarrow 2\pi$ , leaving total Gaussian curvatures tending to  $\pi$  each for the polar caps. We notice a similar trend for the division of total Gaussian curvature between successive walls in the index  $s = 1/2$ , four-wall configuration for nematic order. We discuss this division of Gaussian curvature in Sec. 2.6.

The interaction potential energy of two  $s = 1$  wall configuration is

$$\mathcal{F}^{(\text{int})} = 2\pi[-1 + \log 4 + \log \tan(\omega/2) - 2 \log \sin(\omega)]. \quad (2.29)$$

From Fig. 2.5(b), it is clear that the potential has local minimum at  $\omega = \pi/2$  (equatorial configuration) and global minimum at  $\omega = \pi/3 \simeq 1.05$  which corresponds to the division of Gaussian curvature.

## 2.5 Nematic order

We represent the nematic director field on the sphere by  $\hat{\mathbf{n}} = \cos \alpha \hat{\mathbf{e}}_\theta + \sin \alpha \hat{\mathbf{e}}_\phi$ . Recall that nematic director has head and tail symmetry, i.e.,  $-\hat{\mathbf{n}} \equiv \hat{\mathbf{n}}$ . Thus, the angle  $\alpha$  is measured modulo  $\pi$ .

### 2.5.1 Tetrahedral configuration

To begin with, we discuss the tetrahedral configuration of isolated, disclinations of index  $s = 1/2$ . It is known [33] that for small core sizes the ground state has four disclinations arranged on the vertices of a tetrahedron inscribed in the sphere. The coordinates of these points on unit sphere, for example, are  $v_1 = \{1/\sqrt{3}, 1/\sqrt{3}, 1/\sqrt{3}\}$ ,  $v_2 = \{-1/\sqrt{3}, -1/\sqrt{3}, 1/\sqrt{3}\}$ ,  $v_3 = \{-1/\sqrt{3}, 1/\sqrt{3}, -1/\sqrt{3}\}$ , and  $v_4 = \{1/\sqrt{3}, -1/\sqrt{3}, -1/\sqrt{3}\}$ . The corresponding  $\alpha$ -field (in

isothermal coordinates, see Appendix A) is

$$\begin{aligned} \alpha^{4p}(x, y) = & \frac{1}{2} \arctan\left(\frac{y - \sqrt{3} - 1}{x - \sqrt{3} - 1}\right) + \frac{1}{2} \arctan\left(\frac{y + \sqrt{3} + 1}{x + \sqrt{3} + 1}\right) \\ & + \frac{1}{2} \arctan\left(\frac{y - \sqrt{3} + 1}{x + \sqrt{3} - 1}\right) + \frac{1}{2} \arctan\left(\frac{y + \sqrt{3} - 1}{x - \sqrt{3} + 1}\right). \end{aligned} \quad (2.30)$$

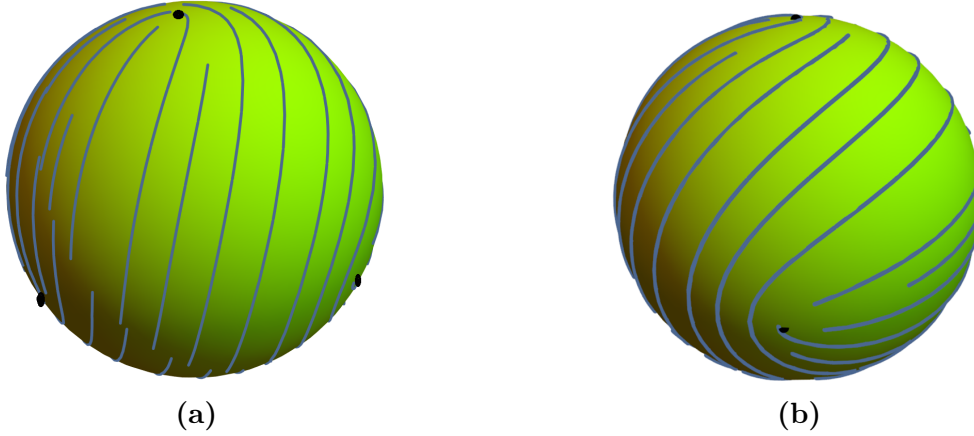


**Figure 2.8:** Tetrahedral configuration: Texture of four point disclinations of index  $s = 1/2$  each placed on the vertices of tetrahedron inscribed in sphere. The block dots represent the cores. (a) Front view. (b) Side view.

For the tetrahedral configuration, we minimise the total free energy numerically, using equal cutoffs (core size  $\zeta$ ) along the  $\theta$ - and  $\phi$  directions, to obtain the optimised core size (Fig. 2.2), and the total free energy (Fig. 2.3). Above  $\zeta \simeq 0.96$  (below  $\eta(0.96) \simeq 0.05$ ), cores of neighboring disclinations overlap each other at nonzero  $\eta$ , and an extension of the Helfrich-Landau mesoscopic approach of Ref. [47] is better suited to address the problem. However, we pursue the Prost and Lubensky approach [33].

### 2.5.2 The four wall configuration

For the sake of generality, we consider four walls of arbitrary indices. The solution to the compatibility condition with boundary conditions ( $\chi(\pi - \theta) = \chi(\theta)$ ,  $\lim_{\theta \rightarrow 0} \partial_\theta \chi(\theta)$  is finite) imply that each wall must have index  $s = 1/2$ . The four-wall configuration has the four-wall (of index  $s = 1/2$  each) has two walls located at  $\theta = (\omega_1^{(4w)}, \omega_2^{(4w)} > \omega_1^{(4w)})$  on the upper hemisphere. The other two symmetry related walls are located in the lower hemisphere, with the convention

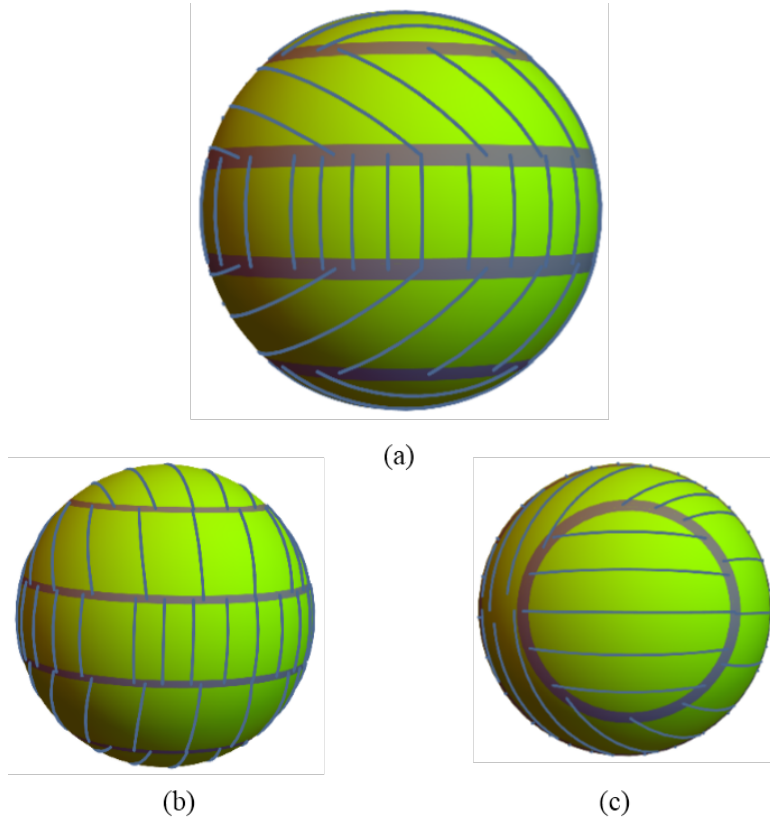


**Figure 2.9:** Four-wall configuration: (a) Side view. (b) Back ( $\theta \simeq \pi/2$ ,  $\phi \simeq 3\pi/2$ ) view. (c) Top view. Each wall in this configuration has the index  $s = 1/2$ , with uniform linear disclination density. Therefore the change in the angle per unit length across each wall is small as compared to that for index  $s = 1$  (and  $s = 2$ ) walls. This should be borne in mind, particularly while viewing the back view (b).

$\omega_3^{(4w)} = \pi - \omega_2^{(4w)}$ ,  $\omega_4^{(4w)} = \pi - \omega_1^{(4w)}$ . The solution to the compatibility condition gives

$$\begin{aligned}
 \chi^{(4w)} = & \frac{1}{2} \left[ \Theta(\theta - \omega_1^{(4w)}) \log\left(\cot \frac{\theta}{2} \tan \frac{\omega_1^{(4w)}}{2}\right) + \Theta(\theta - \omega_2^{(4w)}) \log\left(\cot \frac{\theta}{2} \tan \frac{\omega_2^{(4w)}}{2}\right) \right. \\
 & + \Theta(\theta - \omega_3^{(4w)}) \log\left(\cot \frac{\theta}{2} \tan \frac{\omega_3^{(4w)}}{2}\right) + \Theta(\theta - \omega_4^{(4w)}) \log\left(\cot \frac{\theta}{2} \tan \frac{\omega_4^{(4w)}}{2}\right) \\
 & \left. + 2 \log\left(\csc \theta \tan \frac{\theta}{2}\right) \right].
 \end{aligned} \tag{2.31}$$

In terms of  $\alpha$ -field (Fig. 2.9)

$$\alpha^{(4w)} = \begin{cases} -\phi & \text{if } 0 < \theta < \omega_1^{(4w)} \\ -\phi/2 & \text{if } \omega_1^{(4w)} < \theta < \omega_2^{(4w)} \\ 0 & \text{if } \omega_2^{(4w)} < \theta < \pi - \omega_2^{(4w)} \\ \phi/2 & \text{if } \pi - \omega_2^{(4w)} < \theta < \pi - \omega_1^{(4w)} \\ \phi & \text{if } \pi - \omega_1^{(4w)} < \theta < \pi \end{cases} \quad (2.32)$$

where the superscript (4w) stands for the four walls configuration.

We find numerically optimal core sizes and minimised total free energy of the wall-wall configuration (plotted as a function of  $\eta$  in the Fig. 2.2 and Fig. 2.3 respectively). We find that this configuration is stable only for  $0 < \eta < 0.05$ . In minimising the total free energy of the pairs of walls we need to use two core sizes,  $\zeta_1^{(4w)}$  and  $\zeta_2^{(4w)}$ , for the walls at  $\omega_1^{(4w)}$  and  $\omega_2^{(4w)}$  respectively. We note that optimised wall positions, i.e., the angles  $\omega_1^{(4w)}$  and  $\omega_2^{(4w)}$  are weakly monotonic increasing functions of  $\eta$ . Close to the limit of stability ( $\eta \rightarrow 0.05$ ), the optimal positions of the four walls follow the division of Gaussian curvature. That is the total (integrated) Gaussian curvature of the spherical region between any two successive walls  $K_T \rightarrow \pi = 2\pi \times (\text{index of the wall})$ . In what follows, we extend this trend to  $n$ -atic order.

## 2.6 $n$ -atic order: Division of Gaussian curvature by wall defects

We consider  $n$ -atic order on a sphere with  $2n$  walls of strength  $s = 1/n$  each, and indicate the positions of symmetry related pairs of walls by  $(\omega_k, \omega_{-k} = \pi - \omega_k)$ , where  $k = 1, 2, \dots, n$ . The disclination density of this configuration is

$$\mathcal{S}(\theta) = \frac{1}{n\sqrt{g}} \sum_{k=1}^n [\delta(\theta - \omega_k) + \delta(\theta - \omega_{-k})]. \quad (2.33)$$

Our aim is to minimise the free energy of such configurations with respect to the angular positions of the symmetry-related pairs of walls. For core sizes  $\zeta \rightarrow 0$  the condensation energy is negligibly small, clearly implicating the elastic free

energy as the root cause of the phenomenon of division of Gaussian curvature. To evaluate the elastic free energy of the wall configurations we use the Coulomb gas form of the elastic free energy. Substituting for the  $\phi$ -independent Green's function  $G(\theta; \theta')$  ( Eq. A.14, for further details See Appendix A ) and for  $\mathcal{S}(\theta)$  in Coulomb's free energy expression Eq. 2.9, we find that  $F_{KK} = \text{constant}$ . Thus,  $F_{KK}$  does not contribute to the minimisation. Thus, the interaction potential energy ( $F_{\text{int}}$ ) plays major role in the minimisation. Minimisation of elastic free energy with respect to the angular positions  $\omega_i$  leads to

$$\begin{aligned} \frac{dF_{\text{el}}}{d\omega_i} &= K_\alpha (J_1 + J_2) = 0 \text{ where,} \\ J_1 &= \frac{dF_{K\mathcal{S}}}{d\omega_i} \\ &= \frac{1}{n\sqrt{g}} \sum_{k=1}^n \left[ \int d\theta \sqrt{g} K \left\{ \frac{d}{d\omega_i} G(\theta, \omega_k) + \frac{d}{d\omega_i} G(\theta, \pi - \omega_k) \right\} \right] \\ J_2 &= -\frac{1}{2} \frac{dF_{\mathcal{S}\mathcal{S}}}{d\omega_i} \\ &= -\frac{1}{n^2} \sum_{k=1}^n \sum_{l=1}^n \left[ \frac{d}{d\omega_i} G(\omega_k, \omega_l) + \frac{d}{d\omega_i} G(\omega_k, \pi - \omega_l) \right]. \end{aligned}$$

After some algebraic manipulations, we get  $J_1 = 0$ . Therefore only the  $J_2$  or  $F_{\mathcal{S}\mathcal{S}}$  term is important in determining  $\omega_i$ . The set of angular positions that minimise the elastic free energy is given by

$$2 \cos \omega_i = \frac{2n - 2i + 1}{n}, \quad (2.34)$$

and the integrated Gaussian curvature between the symmetry-related walls at  $\omega_i$  and  $(\pi - \omega_i)$  is

$$\begin{aligned} K_i &= 2\pi \int_{\omega_i}^{\pi - \omega_i} d\theta \sqrt{g} K = 2\pi(2 \cos \omega_i) \\ &= \frac{2\pi}{n}(2n - 2i + 1). \end{aligned}$$

This directly leads to the result that the integrated Gaussian curvature between any two successive walls

$$K_{\text{T}}(i, i + 1) = 2\pi \int_{\omega_i}^{\omega_{i+1}} K \sqrt{g} d\theta = 2\pi/n, \quad (2.35)$$

where  $i = \{1, 2, \dots, 2n - 1\}$  labels the walls in the order of increasing  $\theta$ . Thus, the lowest *elastic free-energy* configuration for  $n$ -atic order has  $2n$  walls of index  $s = 1/n$  each, located such that the integral of Gaussian curvature of the sphere between any two successive walls is  $2\pi/n$ .

## 2.7 Instability of a circular planar wall disclination

In the preceding sections, we show the stability of circular wall disclinations on a sphere. It is interesting to study the stability analysis of a circular wall disclination on a plane. In this next section, we show that wall-disclinations are not stable on a plane, and thus, the Gaussian curvature is essential for stability of wall disclinations. We begin by considering a planar, singular, circular wall disclination in a plane. By definition, the disclination density of circular wall defect of index  $s$  centered at  $r = r_0$  in  $xy$ -plane is

$$\mathcal{S} = \frac{s}{\sqrt{g}} \delta(r - r_0), \quad (2.36)$$

where  $\delta(r)$  is the Dirac delta function. Thus  $\int_0^\infty dr \int_0^{2\pi} \mathcal{S} \sqrt{g} d\phi = 2\pi s$ .

For a plane  $K = 0$ . With this we look for the  $\phi$ - independent stress function that satisfies the compatibility condition (Eq. 1.14). Substituting for the Laplace operator in polar form, the compatibility condition reads as

$$\frac{d^2 \chi}{dr^2} + \frac{1}{r} \frac{d\chi}{dr} = -\frac{s}{r} \delta(r - r_0). \quad (2.37)$$

The general solution for  $\chi(r)$  is

$$\chi(r) = c_2 + c_1 \log\left(\frac{r}{r_0}\right) - s \Theta(r - r_0) \log\left(\frac{r}{r_0}\right) \quad (2.38)$$

where  $\Theta(r)$  is Heaviside theta function. We set the overall additive constant  $c_2 = 0$ . We note that circular polar coordinates have a coordinate singularity at the origin ( $r = 0$ ). This coordinate singularity acts as a point disclination (the polar angle  $\phi$  is multivalued at  $r = 0$ ). We eliminate this spurious singularity by setting  $\lim_{r \rightarrow 0}(d\chi/dr) = 0$ . With this condition we get  $c_1 = 0$ .

Thus the  $\alpha$ -field for the circular wall disclination centered at  $r = r_0$  is

$$\alpha(\phi) = -\phi + s\Theta(r - r_0) + sr\delta(r - r_0)\log\left(\frac{r}{r_0}\right). \quad (2.39)$$

Note that at  $r = r_0$ ,  $\alpha$  is singular. Away from  $r_0$ , the  $\alpha$  is given by (See Fig. 2.10)

$$\alpha(\phi) = \begin{cases} -\phi + const & \text{if } r < r_0 \\ (s - 1)\phi + const & \text{if } r > r_0 \end{cases} \quad (2.40)$$

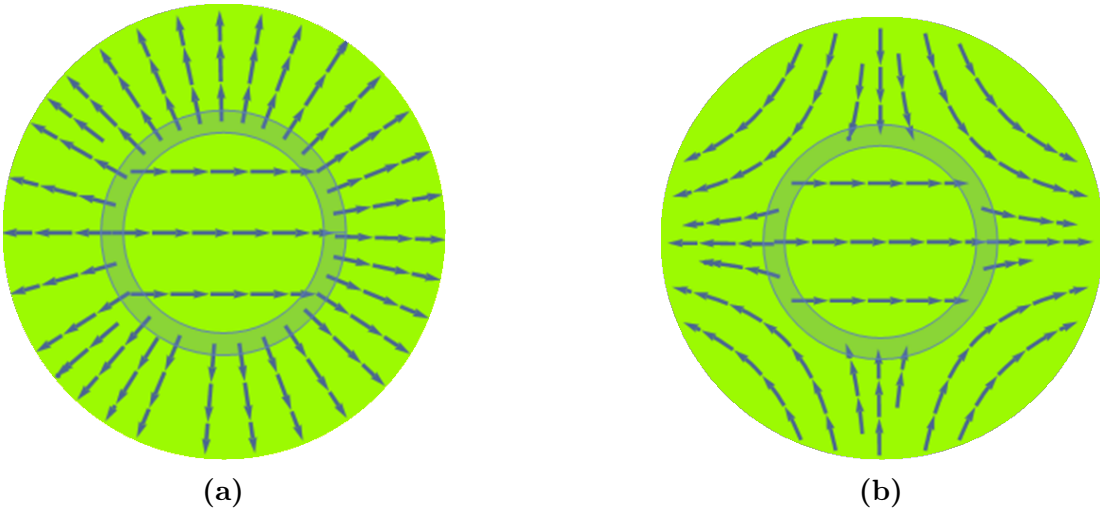


**Figure 2.10:** Texture of planar circular wall: (a) Index of the wall  $s = 1$ . Outside ring, i.e.,  $r > r_0$  the texture matches with that of point disclination of index 1. (b) Texture for index  $s = -1$ . The texture outside the ring is same as point disclination of index  $s = -1$ . In these figures, the shaded region depicts the core centered at  $r_0$ . Note that by shrinking the ring to a point transforms a wall disclination to point disclination with same index.

We note that  $\oint_0^{2\pi} d\alpha_{>} - \oint_0^{2\pi} d\alpha_{<} = 2\pi s$ , where  $\alpha_{<}$  and  $\alpha_{>}$  refer to  $r < r_0$  and  $r > r_0$ , with the integrals taken in the anticlockwise sense around the core.

The free elastic energy density of the circular wall configuration is

$$f_{\text{el}} = \begin{cases} 0 & \text{if } r < r_0 \\ \frac{K_\alpha s^2}{2r^2} & \text{if } r > r_0 \end{cases} \quad (2.41)$$

The singularity at  $r = r_0$  in Eq. 2.41 is eliminated by the use of cutoff to calculate total elastic free energy  $F_{\text{el}}$ . This is as follows

$$\begin{aligned} F_{\text{el}} &= 2\pi \int_0^{r_0-w} f_{\text{el}} dr + 2\pi \int_{r_0+w}^R f_{\text{el}} dr \\ &= K_\alpha \pi s^2 \log\left(\frac{R}{r_0+w}\right). \end{aligned} \quad (2.42)$$

where  $w$  is half-width of the core and  $R$  is the radius of the circular region. The corresponding condensation energy of the wall is

$$\begin{aligned} F_{\text{C}} &= 2\pi \int_{r_0-w}^{r_0+w} f_{\text{C}} r dr \\ &= 4\pi f_{\text{C}} r_0 w. \end{aligned} \quad (2.43)$$

Total free energy (in  $K_\alpha$  units) is

$$\begin{aligned} \mathcal{F} &= \frac{F_{\text{el}} + F_{\text{C}}}{K_\alpha} \\ &= \pi \left[ s^2 \log\left(\frac{R}{r_0+w}\right) + 4 \frac{r_0 w}{\xi^2} \right]. \end{aligned} \quad (2.44)$$

where the correlation length  $\xi = \sqrt{K_\alpha/f_{\text{C}}}$ .

Upon minimisation of  $\mathcal{F}$  w.r.t.  $w$ , we obtain minimised core width  $w = \frac{s^2 \xi^2}{4r_0} - r_0$ . We note that for the stability of wall disclination,  $w > 0$ . This happens if  $r_0 < s\xi/2$ . Otherwise  $w$  becomes negative which is unphysical. Therefore the circular wall is stable if its radius is less than the correlation length ( $s \xi$ ). However, for a planar point disclination of index  $s$ , the core size is of the order of ( $s \xi$ ) [3]. It means that the stability condition for the circular wall demands the radius of the wall be less than the core size of a point disclination of the same index. Thus the planar, circular wall disclination is unstable to the formation of a point disclination with the same index.

Unlike in the case of sphere, wall disclinations are unstable on a plane. We emphasise that the non-zero Gaussian curvature of the sphere stabilises the wall disclinations.

## 2.8 Discussion and conclusions

In this work we have used a simplified version of the Ginzburg-Landau theory to predict the existence of stable topological wall defects (near the order-disorder transition) on spheres with  $n$ -atic order. Wall defects are stable in the range  $0 < \eta < 0.5$ . We use mean field theory to examine the extent to which wall defects are realizable in experiments. This involves estimating the radius  $a$ , the thickness  $h$ , and the temperature range  $\Delta T = T_c - T$  over which stable wall defects are observable.

We recall that the scale of  $\eta$  in Fig. 2.3, Fig. 2.2 is linear in  $\Delta T$ . For the sake of concreteness we consider the experiments of Ref. [35], where molecules of the self assembled monolayer (thickness  $h$  of order molecular size) on the sphere are tilted with respect to the local normal to the sphere. The projection of tilted molecules onto the local tangent plane to the sphere imparts vectorial order to it. Within mean field theory the correlation length diverges as  $\xi = \xi_0(\Delta T/T_c)^{-1/2}$ . The bare correlation length  $\xi_0$  is of order 2 nm (molecular dimensions), and  $K_\alpha \simeq k_B \Delta T$ , leading to  $f_C \simeq k_B \Delta T / \xi^2$ . Substituting for  $\xi$  in  $\eta$ , we get  $\Delta T \simeq T_c(\xi_0/a)^2 \eta$ . For  $T_c \simeq 300K$ , spheres with  $a = 5nm$ , and  $a = 10nm$  (used in Ref. [35]),  $\eta = 0.1$  corresponds to  $\Delta T \simeq 4.8K$  and  $\Delta T \simeq 1.2K$ , respectively, thus establishing the temperature scale. For  $a = 35nm$ ,  $\eta = 0.1$ , corresponds to  $\Delta T \simeq 0.1K$ . For  $a = 35nm$  the equatorial wall is stable between  $\eta \simeq 0.16$  ( $\equiv \Delta T = 0.16K$ ) and  $\eta \simeq 0.5$  ( $\equiv \Delta T = 0.5K$ ); it is likely to be the simplest one to observe. Evidently, for large core sizes, point as well as wall defects will not have a ‘‘valence’’ = 1, as is the case for the antipodal disclinations of Ref. [35]. However, nano-particles with small radii of order 35 nm are faceted [48] and cannot be reliably approximated as spheres. Thus the observation of wall defects (as against antipodal point disclinations) using nano-particles may not yet be possible using available experimental techniques.

In our analysis we have ignored the effects of thermal fluctuations. Fluctuation effects will be important close to  $T_c$ . However, spheres are closed surfaces,

and the system size is very small, thus diminishing the effects of fluctuations. The nature of order-disorder transition on orientationally ordered spheres is not clear and needs to be investigated. In particular, the transition may not be of the Kosterlitz-Thouless type (see, e.g., Ref. [3]). Close to  $T_c$ , interacting wall defects rather than point defects will dominate the transition. It would be of interest to extend the theory to include a detailed analysis of fluctuation effects, the effects of anisotropy of elastic constants and study the shape changes of deformable vesicles, induced by wall defects.



## Chapter 3

# Point- and wall disclinations on catenoids

### 3.1 Introduction

The preceding chapter is devoted to the study of the stability of point and wall disclinations (with total index  $s = 2$ ) on rigid spheres, in consequence of the Poincaré-Hopf index theorem. For spheres, the Gaussian curvature  $K$  is uniform and positive. It is natural to extend our investigation of the stability of wall disclinations to surfaces with  $K < 0$ . In Chapters 3 and 4, we consider catenoids and helicoids as example surfaces (Fig. 3.1). They are minimal surfaces i.e., their mean-curvature  $H = 0$ , and Gaussian curvature are negative.

Unlike spheres, catenoids and helicoids are open surfaces. Thus there is no topological imperative to have disclinations with a specified total index on catenoids and helicoids endowed with orientational order. This chapter is dedicated to the study of the stability of point- and wall disclinations on catenoids. We discuss the stability of *point* disclinations in vector-, nematic-, tetratic- and hexatic order on catenoids. We extend the investigation of stability of wall disclinations, and find that they are stable near the order disorder transition over a finite range of a dimensionless parameter  $\eta$ . The parameter  $\eta$  is the ratio of energy scales corresponding to the destruction of order in defect core and elastic deformation outside the core. To begin with we introduce the geometrical information of a catenoid that is essential for the investigation, and discuss vector order on a catenoid.

## 3.2 Vector order

We consider a catenoid with parameterization  $\mathbf{R}(\phi, z) = \{a \cosh(z/a) \cos \phi, a \cosh(z/a) \sin \phi, z\}$ , where  $-\infty < z < \infty$  and  $0 \leq \phi < 2\pi$ . Here  $a$  is the neck radius of the catenoid. The Gaussian and mean curvature of the catenoid, respectively, are  $K = -(1/a^2) \operatorname{sech}^2(z/a)$  and  $H = 0$ . The components of the metric tensor are  $g_{\phi\phi} = a^2 \cosh^2(z/a)$ ,  $g_{zz} = \cosh^2(z/a)$ ,  $g_{\phi z} = g_{z\phi} = 0$ , and the determinant of metric tensor  $g = a^2 \cosh^4(z/a)$ . Since the tangent vectors  $\mathbf{t}_\phi(\phi, z)$  and  $\mathbf{t}_z(\phi, z)$  are orthogonal, it is natural to choose  $\hat{\mathbf{e}}_1(\phi, z) = \hat{\mathbf{t}}_\phi(\phi, z)$  and  $\hat{\mathbf{e}}_2(\phi, z) = \hat{\mathbf{t}}_z(\phi, z)$ . In this coordinate system the components of spin connection terms are  $\mathbf{A} = (A_\phi, A_z) = (\tanh(z/a), 0)$ . Thus, any unit tangent vector field on the catenoidal surface can be expressed as  $\hat{\mathbf{m}}(\phi, z) = \cos \alpha(\phi, z) \hat{\mathbf{e}}_\phi + \sin \alpha(\phi, z) \hat{\mathbf{e}}_z$ . With this background we discuss point- and wall disclinations in vector-, and nematic order on a catenoid.

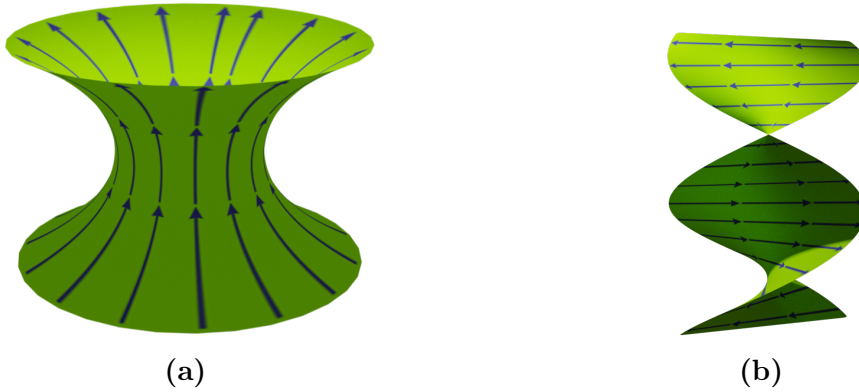


**Figure 3.1:** (a) Catenoid with disclination-free configuration. (b) Helicoid with disclination-free configuration.

### 3.2.1 Disclination-free configuration

The simplest disclination-free configuration that satisfies the Euler-Lagrange equation 1.13 is  $\alpha = \pi/2$  (Fig. 3.1(a)). For a catenoid with total height  $2l$  ( $z = -l$  to  $z = l$ ) the elastic free energy of this configuration is

$$F_{\text{el}}^{(0)} = 2\pi K_\alpha \left[ \frac{l}{a} - \tanh\left(\frac{l}{a}\right) \right], \quad (3.1)$$

where the superscript (0) represents the disclination-free configuration.

Because of large splay deformation far away from the neck (See Fig. 3.1),  $F_{\text{el}}^{(0)}$  diverges linearly as  $l \rightarrow \infty$ . Thus the disclination-free configuration is untenable for an infinite catenoid.

### 3.2.2 Point disclinations

Noticing that the total (integrated) Gaussian curvature of a catenoid of infinite extent is  $K_t = \int_0^{2\pi} d\phi \int_{-\infty}^{\infty} K \sqrt{g} dz = -4\pi$ , we consider point disclination(s) of total index  $s = -2$  on an infinite catenoid. If  $K_t \neq -4\pi$ , the elastic free energy of a catenoid with infinite extent diverges as is the case with the disclination-free configuration discussed above.



**Figure 3.2:** Two point disclinations of index  $s = -1$  : (a) Side view ( $z = 0, \phi = 3\pi/2$ ) of two point disclinations of index  $s = -1$ . (b) Front view ( $z = 0, \phi = 0$ ) of two point disclinations of index  $s = -1$ . The black dot in (a) depicts the core region of the point disclination.

It is known that two point disclinations of index  $s = -1$  each, located diametrically opposite on the neck ( $z = 0$ ; and  $\phi = \{\pi/2, 3\pi/2\}$  for example) have lowest elastic free energy for vectorial order [49]. The  $\alpha$  field for this configuration is (See Fig. 3.2)

$$\alpha^{(2p)}(\phi, z) = -\arctan[\cot \phi \coth(z/a)], \quad (3.2)$$

where the superscript (2p) refers to the two point disclinations. The expression above is obtained by considering level sets of the catenoid (intersection of the catenoid with  $y = \text{const.}$  planes), and is a solution to the Euler-Lagrange equation 1.13. We note that  $\alpha$ -field for the same configuration obtained from isothermal coordinates have more elastic deformations (See Appendix B). From

Eq. 2.5 the elastic free energy density of two point disclinations is

$$f_{\text{el}}^{(2\text{p})} = \frac{K_\alpha \sin^2(\phi) \operatorname{sech}^4(z/a)}{a^2 [\cosh(2z/a) + \cos(2\phi)]} \quad (3.3)$$

which has singular behavior at  $z = 0$  and  $\phi = \{\pi/2, 3\pi/2\}$ . For simplicity, we take two different cutoffs corresponding to  $z$  and  $\phi$  directions for each core. Let  $2\xi_z$  and  $2\xi_\phi$  be the core sizes along  $z$  and  $\phi$  directions. The free elastic energy away from the core regions is

$$\begin{aligned} F_{\text{el}}^{(2\text{p})} = & \int_{-\infty}^{\infty} dz \left[ \int_0^{\pi/2-\Delta_\phi} d\phi \sqrt{g} f_{\text{el}}^{(2\text{p})} + \int_{\pi/2-\Delta_\phi}^{3\pi/2+\Delta_\phi} d\phi \sqrt{g} f_{\text{el}}^{(2\text{p})} + \int_{3\pi/2-\Delta_\phi}^{2\pi} d\phi \sqrt{g} f_{\text{el}}^{(2\text{p})} \right] \\ & + \int_{\Delta_z}^{\infty} dz \left[ \int_{\pi/2-\Delta_\phi}^{\pi/2+\Delta_\phi} d\phi \sqrt{g} f_{\text{el}}^{(2\text{p})} + \int_{3\pi/2-\Delta_\phi}^{3\pi/2+\Delta_\phi} d\phi \sqrt{g} f_{\text{el}}^{(2\text{p})} \right] \\ & + \int_{-\infty}^{-\Delta_z} dz \left[ \int_{\pi/2-\Delta_\phi}^{\pi/2+\Delta_\phi} d\phi \sqrt{g} f_{\text{el}}^{(2\text{p})} + \int_{3\pi/2-\Delta_\phi}^{3\pi/2+\Delta_\phi} d\phi \sqrt{g} f_{\text{el}}^{(2\text{p})} \right] \end{aligned} \quad (3.4)$$

where the cutoffs  $\Delta_z$ ,  $\Delta_\phi$  and core sizes are related by  $\Delta_z = a \operatorname{arcsinh}[\xi_z/a]$  and  $\Delta_\phi = (\xi_\phi/a) \operatorname{sech}[z/a]$ . The condensation energy is given by

$$\begin{aligned} F_{\text{C}}^{(2\text{p})} &= 2f_{\text{C}} \int_{-\Delta_z}^{\Delta_z} dz \int_{\pi/2-\Delta_\phi}^{\pi/2+\Delta_\phi} d\phi \sqrt{g} \\ &= 8f_{\text{C}} \xi_z \xi_\phi. \end{aligned} \quad (3.5)$$

We define the dimensionless total free energy  $\mathcal{F}^{(2\text{p})} = F_{\text{T}}^{(2\text{p})}/K_\alpha$ , where the total free energy  $F_{\text{T}}^{(2\text{p})} = F_{\text{el}}^{(2\text{p})} + F_{\text{C}}^{(2\text{p})}$ . We note that  $\mathcal{F}^{(2\text{p})}$  is a function of dimensionless core sizes  $\zeta_z = \xi_z/a$ ,  $\zeta_\phi = \xi_\phi/a$ , and that the dimensionless parameter  $\eta = (a^2 f_{\text{C}})/K_\alpha$ . Within the mean field theory,  $\eta \sim (T_c - T)$ .

Numerically obtained core sizes  $\zeta_z^{(2\text{p})}$ ,  $\zeta_\phi^{(2\text{p})}$ , and the minimised total free energy  $\mathcal{F}^{(2\text{p})}$  are plotted in Fig. 3.3, and Fig. 3.4 as functions of  $\eta$ . As  $\eta \rightarrow 0$ ,  $\zeta_z^{(2\text{p})} \rightarrow \infty$ , and  $\zeta_\phi^{(2\text{p})} \rightarrow \pi/2$ . This indicates that orientational order is destroyed over the entire catenoid. *Unlike the disclination-free configuration, the total free energy of two point disclinations on an infinite catenoid is finite.*

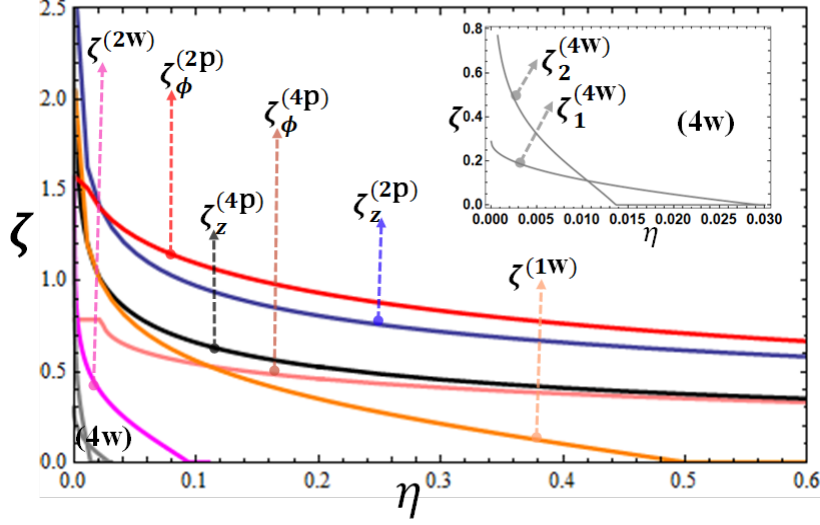


**Figure 3.3:** Optimal core sizes: The notations (2p), (1w), (2w), (4p) and (4w) represent the two point (index  $s = -1$  each)-, single wall (index  $s = -2$ )-, two wall (index  $s = -1$  each)-, four point (index  $s = -1/2$  each)-and four wall (index  $s = -1/2$  each)-configurations, respectively. The subscripts  $z, \phi$  represent the core sizes along those directions. The inset depicts the two core sizes required to minimise the total free energy for the 4w configuration. For 4p configuration, the optimal cores along  $\phi$  direction overlap up to  $\eta \simeq 0.02$  and indicating the single wall configuration at neck (See the text.).

### 3.2.3 Wall disclinations

To investigate the stability of wall disclinations on catenoids, we follow the same procedure as used for spherical membranes. In summary we solve for the stress function  $\chi$  for given a disclination density. As the starting point, we consider a disclination wall of total strength  $s_0$  at the neck ( $z = 0$ ), with disclination density

$$\mathcal{S}^{(1w)} = \frac{s_0}{\sqrt{g}} \delta(z), \quad (3.6)$$

where the superscript (1w) stands for a single wall. Thus  $\int_0^{2\pi} d\phi \int_{-\infty}^{\infty} \mathcal{S}^{(1w)} \sqrt{g} dz = 2\pi s_0$ , where  $s_0$  is yet to be determined. With this disclination density, the  $\phi$ -independent stress function  $\chi^{(1w)}(z)$  is obtained by solving for the compatibility condition (Eq. 1.14). The general solution, apart from an additive constant, is given by

$$\chi^{(1w)}(z) = c z - \frac{s_0}{a} z \Theta(z) - \log[\cosh(\frac{z}{a})], \quad (3.7)$$

where  $c$  is a constant, and  $\Theta(z)$  is unit step function defined as,  $\Theta(z) = 1$  for  $z > 0$  and  $\Theta(z) = 0$  for  $z < 0$ .

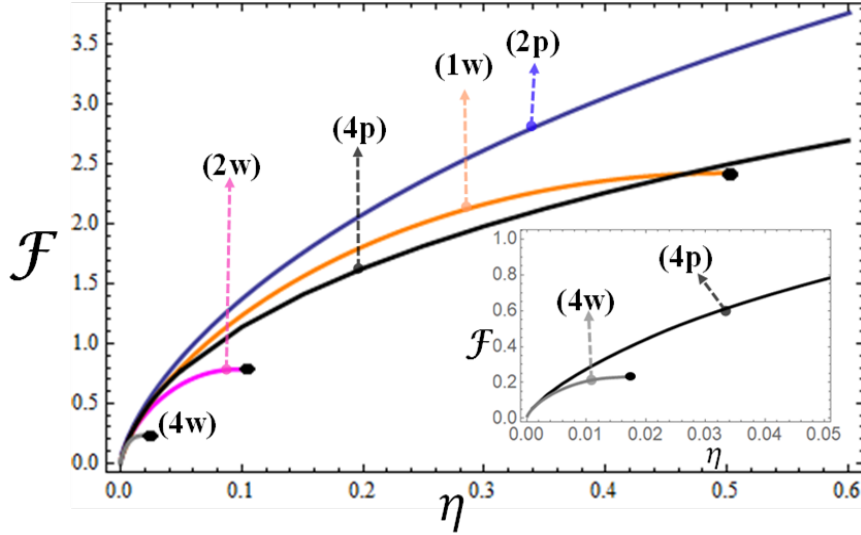


**Figure 3.4:** Minimised free energy  $\mathcal{F}$ : The dots indicate the  $\eta$ -values beyond which wall defects are unstable ( $\zeta(\eta) = 0$ ), see Fig. 3.3. The notations (2p), (1w), (2w), (4p) and (4w) represent the two point (index  $s = -1$  each)-, single wall (index  $s = -2$ )-, two wall (index  $s = -1$  each)-, four point (index  $s = -1/2$  each)-and four wall (index  $s = -1/2$  each)-configurations, respectively.

We seek the solution to the compatibility condition (Eq. 1.14) with the boundary conditions

$$\chi(-z) = \chi(z), \text{ and } \partial_z \chi \rightarrow 0 \text{ as } z \rightarrow \infty. \quad (3.8)$$

With these boundary conditions, we get  $c = -1/a$  and  $s_0 = -2$ .

$$\chi^{(1w)}(z) = -\log\left[\cosh\left(\frac{z}{a}\right)\right] + \frac{|z|}{a}. \quad (3.9)$$

The Euler characteristic of a catenoid is zero, and the Poincaré-Hopf index theorem is not applicable. Thus the result  $s_0 = -2$  is a consequence of free energetic considerations alone. The solution 3.9 is particularly simplified in terms

of the  $\alpha$ - field (See Fig. 3.5)

$$\alpha^{(1w)}(\phi, z) = \begin{cases} \phi & \text{if } z > 0 \\ -\phi & \text{if } z < 0 \end{cases} \quad (3.10)$$

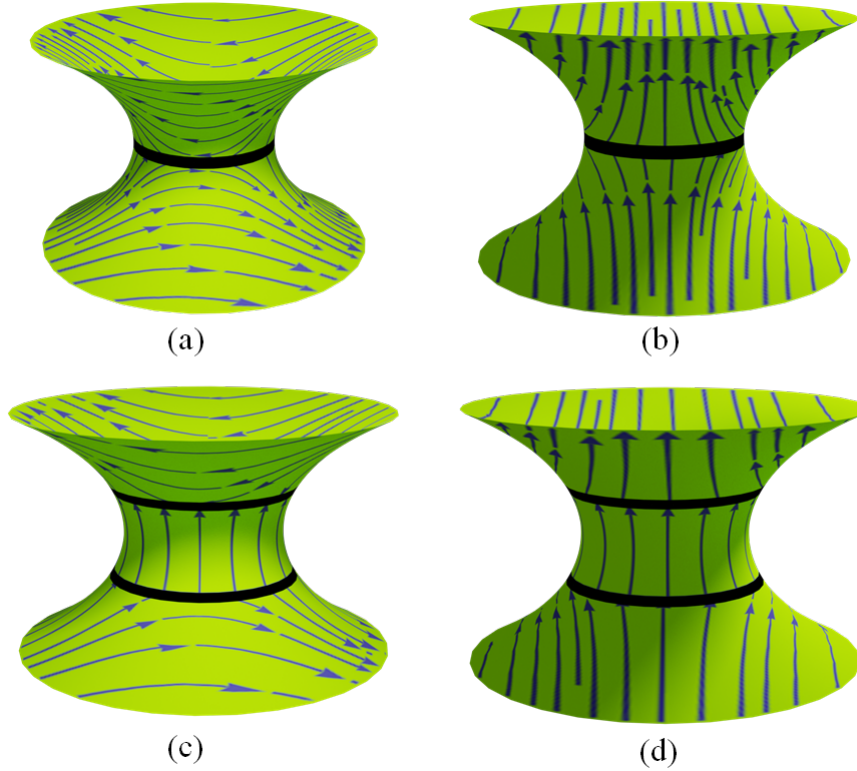


**Figure 3.5:** Wall configuration in vector order: (a) Front view of single wall disclination of index  $s = -2$ . (b) Side view of single wall disclination of index  $s = -2$ . (c) Front view, (d) Side view of two wall disclinations of index  $s = -1$  each. The shaded regions in above figures illustrate cores of the wall disclination(s).

It is easy to check that  $\oint d\alpha_{(lh)}^{(1w)} - \oint d\alpha_{(uh)}^{(1w)} = -4\pi$ , where  $\alpha_{(lh)}^{(1w)}$  and  $\alpha_{(uh)}^{(1w)}$  refer to the lower half ( $z < 0$ ) and the upper half ( $z > 0$ ) of the catenoid respectively, with the integrals taken in the anticlockwise sense around outward normal to the surface. Thus, the index of the single wall is  $-4\pi/(2\pi) = -2$ . This result is easily generalised to walls having other indices.

Substituting the exact solution for  $\chi$  (Eq. 3.9) in the free elastic energy density (Eq. 2.6), we get the elastic free energy density of the wall as

$$f_{\text{el}}^{(1\text{w})} = \frac{K_\alpha}{2a^2} \operatorname{sech}\left(\frac{z}{a}\right)^2 [1 - 2\Theta(z) - 2z\delta(z) + \tanh\left(\frac{z}{a}\right)]^2. \quad (3.11)$$

The presence of  $\delta(z)$  is crucial for discussing the energetics and thereby the stability of the wall disclination. Let  $2\xi$  be the wall width measured on the surface of the catenoid, then the cutoff in  $z$ -integral  $\Delta_z = a \operatorname{arcsinh}(\xi/a)$ . For a catenoid of height  $2l$  the elastic free energy of this configuration is

$$\begin{aligned} F_{\text{el}}^{(1\text{w})} &= 2 \times 2\pi \int_{\Delta_z}^l f_{\text{el}}^{(1\text{w})} \sqrt{g} dz \\ &= 2\pi K_\alpha \left\{ \frac{\zeta}{\sqrt{1+\zeta^2}} - \operatorname{arcsinh}(\zeta) + \log\left(\frac{1+\zeta^2}{\zeta + \sqrt{1+\zeta^2}}\right) \right. \\ &\quad \left. + \mathcal{L} - \log[\cosh(\mathcal{L})] - \tanh(\mathcal{L}) \right\}, \end{aligned} \quad (3.12)$$

where the dimensionless core size  $\zeta = \xi/a$  and the dimensionless length  $\mathcal{L} = l/a$ . In the limit  $l \rightarrow \infty$ ,  $F_{\text{el}}^{(1\text{w})}$  reduces to

$$F_{\text{el}}^{(1\text{w})} = 2\pi K_\alpha \left[ \frac{\zeta}{\sqrt{1+\zeta^2}} - \operatorname{arcsinh}(\zeta) + \log\left(\frac{1+\zeta^2}{\zeta + \sqrt{1+\zeta^2}}\right) + \log(4) - 1 \right]. \quad (3.13)$$

The condensation energy of the core is

$$\begin{aligned} F_{\text{C}}^{(1\text{w})} &= 2\pi f_{\text{C}} \int_{-\Delta_z}^{\Delta_z} \sqrt{g} dz \\ &= \pi a^2 f_{\text{C}} \{2 \operatorname{arcsinh}(\zeta) + \sinh[2 \operatorname{arcsinh}(\zeta)]\}. \end{aligned} \quad (3.14)$$

We numerically minimise the dimensionless total free energy  $\mathcal{F}^{(1\text{w})} = F_{\text{T}}^{(1\text{w})}/K_\alpha$ , where  $F_{\text{T}}^{(1\text{w})} = F_{\text{el}}^{(1\text{w})} + F_{\text{C}}^{(1\text{w})}$ , to get the optimised core size  $\zeta^{(1\text{w})}$  (Fig. 3.3), and minimised total energy  $\mathcal{F}^{(1\text{w})}$  (Fig. 3.4) as functions of  $\eta$ . Recall,  $\eta \sim (T_c - T)$ . We find that at  $\eta = 0.5$  the minimised core size  $\zeta^{(1\text{w})}$  is zero and becomes negative for  $\eta > 0.5$ , which is unphysical. Within the coarse grained theory,  $\zeta^{(1\text{w})} = 0$  implies that the cutoff is order of molecular length-scale. Thus, it sets the limit of stability of the wall disclination. For  $0 < \eta < 0.5$  the single wall disclination is stable, and has lower free energy than that for the configuration of

two point disclinations (Fig. 3.4).

The study of the single wall disclination (of index  $s = -2$ ) at the neck so far is the starting point to investigate the stability of the wall disclinations on catenoid. We chose the position of the single wall at the neck owing to the symmetry of the catenoid. In general, we can place the wall anywhere on the surface of catenoid. However, the potential energy due to the interaction between curvature and the wall disclination decides the optimal position. We show below that the neck is indeed optimal position for the single wall configuration of index  $s = -2$ .

For the sake of generality, we study interaction potential of a single wall disclination of index  $s_0$  at position  $z = d$ . The corresponding disclination density is given by

$$\mathcal{S}^{(1w)} = \frac{s_0}{\sqrt{g}} \delta(z - d). \quad (3.15)$$

Note that the Green's function on catenoid plays the important role in calculating the interaction energy of wall-defect configurations. Given the azimuthal symmetry of the configuration, we seek the  $\phi$ -independent Green's function, with the conditions  $G(z; z') = G(z'; z)$ , and  $G(-z; -z') = G(z; z')$ . The solution is

$$G(z; z') = \frac{|z - z'|}{4\pi a}, \quad (3.16)$$

Substituting the Green's function  $G(z; z')$  and  $\mathcal{S}^{(1w)}$  in interaction potential energy (Eq. 2.10), we get the interaction potential energy of the single wall disclination as a function of its position  $d$ . The analytic expression is given below and plotted in Fig. 3.6

$$\frac{F_{\text{int}}^{(1w)}}{K_\alpha} = -2\pi s_0 \log\left[2 \cosh\left(\frac{d}{a}\right)\right]. \quad (3.17)$$

From the Fig.3.6 it is clear that the interaction potential energy for positive wall disclinations ( $s_0 > 0$ ) is minimum at  $\pm\infty$ . Therefore positive wall disclinations are expelled from the neck ( $d = 0$ ) region of the catenoid. For negative wall disclinations ( $s_0 < 0$ ), interaction potential energy is minimum at the neck ( $d = 0$ ) and they are attracted to the neck region where the Gaussian curvature effects are predominant. However, the finite distortion energy constraint implies

that index of the wall  $s_0 = -2$ . Thus, the single wall of index  $s = -2$  placed at the neck is the minimum energy configuration.

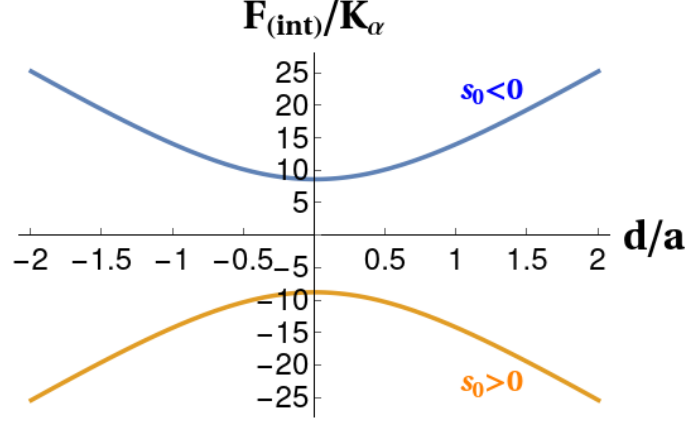


**Figure 3.6:** Interaction potential energy (dimensionless)  $\mathcal{F}^{(\text{int})} = F_{(\text{int})}/K_{\alpha}$  for the single wall disclination of index  $s_0$ . The curve above  $d/a$ -axis is for  $s_0 < 0$ , indicating that negative disclinations are attracted towards the neck region. The behavior of positive disclinations ( $s_0 > 0$ ) is shown in the curve which is below  $d/a$ -axis. Positive disclinations are expelled from the neck region.

The ground state configuration for vector order can have more than one wall disclination. Therefore we consider two walls of index  $s_1$  and  $s_{-1}$  placed symmetrically at  $z = \pm d$  on the catenoid. The disclination density for this configuration is

$$\mathcal{S}^{(2w)} = \frac{s_1}{\sqrt{g}}\delta(z-d) + \frac{s_{-1}}{\sqrt{g}}\delta(z+d). \quad (3.18)$$

The solution to the compatibility condition (Eq. 1.14) subject to the boundary conditions (Eq. 3.8) yields that  $s_1 = s_{-1} = -1$ , and the total disclination index  $s_T = -2$ . The corresponding  $\alpha$ -field, apart from an additive constant, is given by (Fig. 3.5),

$$\alpha^{(2w)}(\phi, z) = \begin{cases} \phi & \text{if } z > d \\ 0 & \text{if } -d < z < d \\ -\phi & \text{if } z < -d \end{cases} \quad (3.19)$$

where superscript (2w) stands for two wall configuration. In calculating elastic energy ( $F_{\text{el}}^{(2w)}$ ), we consider the same core size ( $\xi$ ) on both sides of the walls. The

condensation energy of the walls is

$$\begin{aligned} F_C^{(2w)} &= 2 \times 2\pi f_C \int_{d-\Delta_z}^{d+\Delta_z} \sqrt{g} dz \\ &= 2\pi a^2 f_C \left[ \frac{2\Delta_z}{a} + \cosh\left(\frac{2d}{a}\right) \sinh\left(\frac{2\Delta_z}{a}\right) \right] \end{aligned} \quad (3.20)$$

where  $\Delta_z = a \operatorname{arcsinh}[(\xi/a) \operatorname{sech}(d/a)]$ .

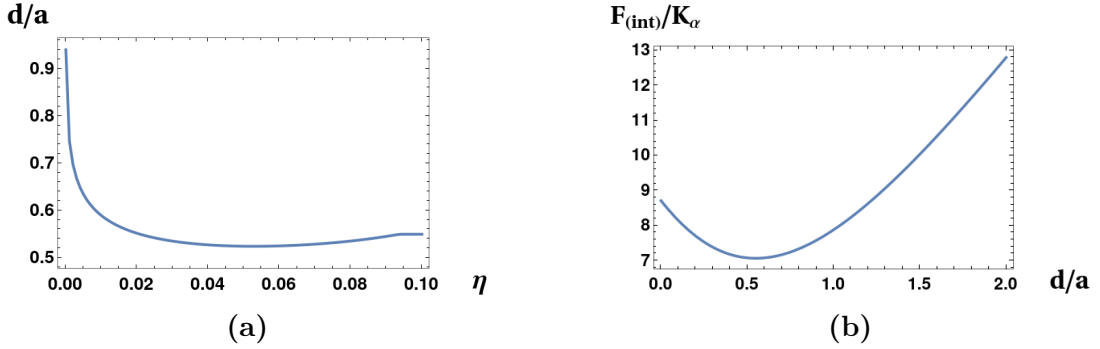


**Figure 3.7:** (a) Equilibrium position of two-wall configuration: The plot of  $d/a$  vs  $\eta$ . At  $\eta \simeq 0.1$ ,  $d^{(2w)} \simeq 0.55 a$ . (b) The interaction potential energy of the two wall disclinations of index  $-1$  each placed symmetrically at  $z = \pm d$ . The function has minimum at  $d \simeq 0.55 a$  which implies the division of Gaussian curvature (See text below.).

The optimised dimensionless core size  $\zeta^{(2w)} = \xi/a$  and dimensionless position  $D^{(2w)} = d/a$  are obtained, numerically, by minimising  $\mathcal{F}^{(2w)}$ . The plot of  $\zeta^{(2w)}$  (Fig. 3.3) shows that the two-wall configuration is stable up to  $\eta \simeq 0.1$ . The equilibrium positions of the walls are also functions of  $\eta$ , and close to the limit of stability ( $\eta \rightarrow 0.1$ ), the walls are located such that the total (integrated) Gaussian curvature between them  $K_T \rightarrow -2\pi$ ,  $D^{(2w)} \simeq 0.55$ . Within the range of stability the total free energy of the two-wall configuration ( $\mathcal{F}^{(2w)}$ ) is less than that of single wall configuration (Fig. 3.4). Thus, for  $0 < \eta < 0.1$ , and the two-wall configuration is the ground state.

The interaction energy of two wall-disclinations of index  $s = -1$  each, placed at  $z = \pm d$  is given by (Fig.3.7(b))

$$\frac{F_{\text{int}}^{(2w)}}{K_\alpha} = 4\pi \log\left[2 \cosh\left(\frac{d}{a}\right)\right] - 2\pi \frac{d}{a}. \quad (3.21)$$

The function has minimum at  $d \simeq 0.55 a$ , which implies the division of Gaussian curvature—the total (integrated) Gaussian curvature between the two walls is  $K_T = -2\pi = 2\pi \times (\text{index of the wall})$ . In what follows, we explore the division of Gaussian curvature for nematic order, and extend it to  $n$ -atic order. In the next section, we discuss the nematic order.

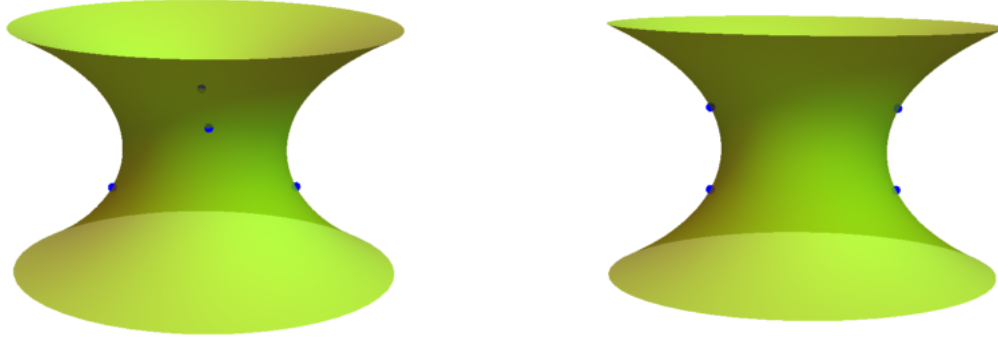
### 3.3 Nematic order

We choose the nematic director field on catenoid as  $\hat{\mathbf{n}} = \cos \alpha \hat{\mathbf{e}}_\phi + \sin \alpha \hat{\mathbf{e}}_z$ , with  $-\hat{\mathbf{n}} \equiv \hat{\mathbf{n}}$ . The symmetry of the nematic director allows the disclination indices to have half-integer values. This reduces the elastic free energy further [3].

#### 3.3.1 Four point disclinations

We consider four index  $s = -1/2$  point disclinations on a catenoid, so that the total index is  $s_T = -2$ . We study the interaction potential among these disclination in two different configurations. **(i). Alternating configuration (A-I)** in which two  $s = -1/2$  disclinations are placed in the  $z = d$  plane with angular separation of  $\pi$  (e.g.,  $\phi = \{3\pi/4, 7\pi/4\}$ ), and the remaining two  $s = -1/2$  disclinations are located in the  $z = -d$  plane (with angular separation of  $\pi$ , e.g.,  $\phi = \{\pi/4, 5\pi/4\}$ ) such that position of disclination is rotated by  $\pi/2$  with respect to the position of disclination in  $z = d$  plane (Fig. 3.8(a)). **(ii). Atop configuration (A-II)** in which two  $s = -1/2$  disclinations are placed in the  $z = d$  plane with angular separation of  $\pi$  (e.g.,  $\phi = \{\pi/4, 5\pi/4\}$ ), and remaining two  $s = -1/2$  disclinations are located in the  $z = -d$  plane (with angular separation of  $\pi$ , e.g.,  $\phi = \{\pi/4, 5\pi/4\}$ ) such that position of disclinations is directly beneath the position of disclinations in  $z = d$  plane (Fig. 3.8(b)).

The interaction potential plots of both configurations as a function of position is given in Fig 3.9(a). It is clear that configuration-I with  $d = 0$  (the neck) has the minimum energy. To check whether it is a global minimum, we consider all four disclinations placed on the neck with angular position  $\{\pi/4, \omega + \pi/4, 5\pi/4$  and  $5\pi/4 + \omega\}$ . Numerically it is obtained that equilibrium positions of the disclinations (global minimum) are such that they sit on the neck with an angular separation of  $\pi/2$  between two adjacent disclinations (Fig 3.9(b)). This result is in agreement with [49]. The corresponding  $\alpha$ -field is given below and



(a) Alternating configuration (A-I)

(b) Atop configuration (A-II)

**Figure 3.8:** Arrangement of four point disclinations of index  $s = -1/2$  each. The blue dots in the figures represent the position of disclinations.

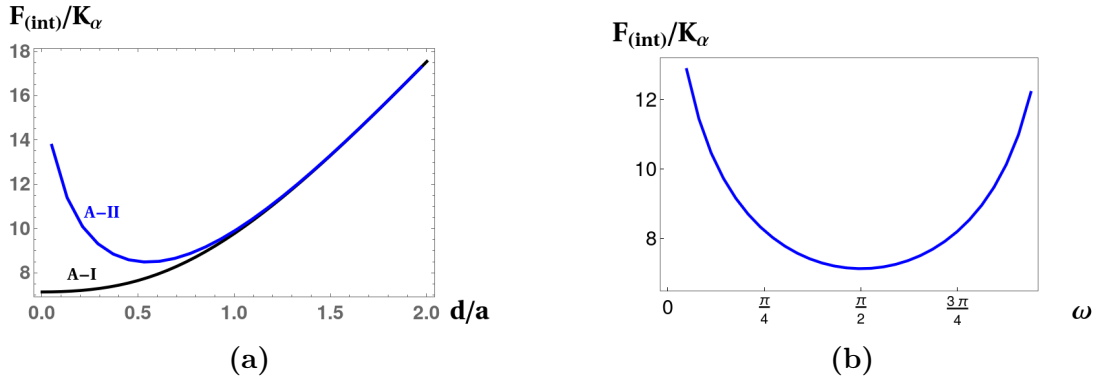


**Figure 3.9:** Interaction potential plots of four  $s = -1/2$  point defects: (a) Black color curve is for the alternating configuration (A-I) and blue color curve is for the atop configuration (A-II). (b) Four disclinations placed on the neck with angular position  $\{\pi/4, \omega + \pi/4, 5\pi/4$  and  $5\pi/4 + \omega\}$ . Interaction potential as function of  $\omega$  is plotted and it has minimum at  $\omega = \pi/2$ .

shown in Fig. 3.10.

$$\alpha^{(4p)} = \frac{1}{2} \arctan[\tan(\phi + \pi/4) \coth(\frac{z}{a})] - \frac{1}{2} \arctan[\cot(\phi + \pi/4) \coth(\frac{z}{a})]. \quad (3.22)$$

To obtain the optimal core sizes we use two different core sizes  $\zeta_z^{(4p)}$  and  $\zeta_\phi^{(4p)}$  along  $z$ - and  $\phi$ -directions respectively. Here, the superscript (4p) stands for the four point disclinations configuration. The minimised total free energy  $\mathcal{F}^{(4p)}$  is plotted as function of  $\eta$  and shown in Fig. 3.4. We notice that (Fig. 3.3),

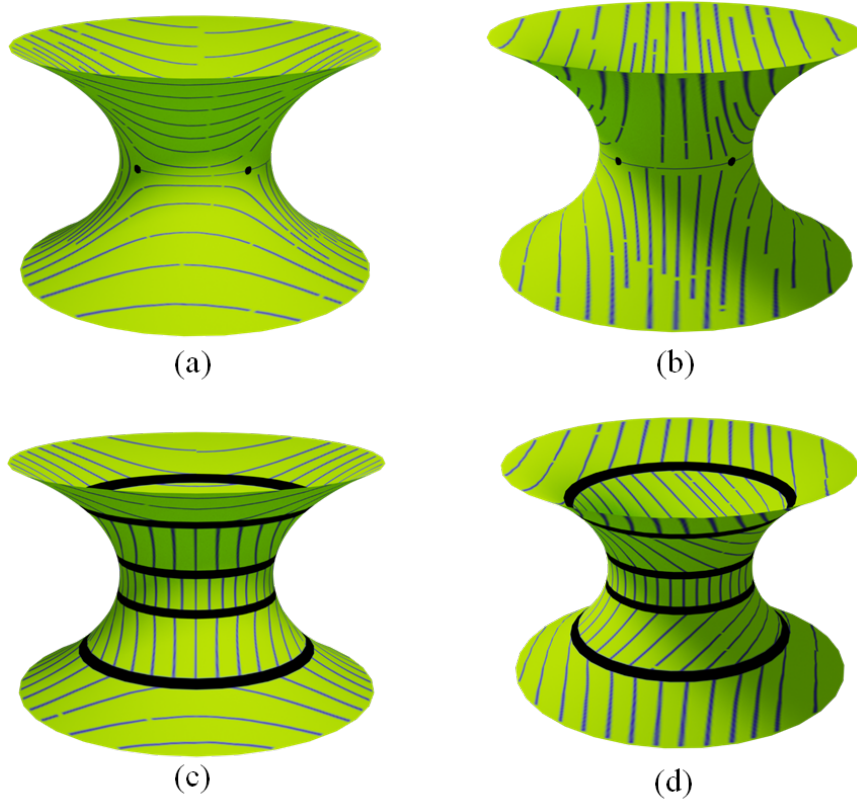


**Figure 3.10:** Defects in nematic order:(a) Side view of four point disclinations of index  $s = -1/2$  each. (b) Front view of four point disclinations. (c) Front view of four wall disclinations of index  $s = -1/2$  each. (d) Side view of four wall disclinations. The shaded regions in above figures illustrate the cores.

the optimised core sizes along  $\phi$ -direction ( $\zeta_\phi^{(4p)}$ ) overlap up to  $\eta \simeq 0.02$ . This vindicates the instability of point disclinations configuration. In this range of  $\eta$ , the four point disclinations configuration resembles the single wall disclination.

### 3.3.2 Four-wall configuration

We place four wall- configuration of  $s = -1/2$  each, symmetrically about the  $z$  axis at the positions  $z = \pm d_1, \pm d_2$ . The solution to the compatibility condition (Eq. 1.14) is given by

$$\begin{aligned} \chi^{(4w)} = \frac{1}{2a} & [(z - d_1)\Theta(z - d_1) + (z + d_1)\Theta(z + d_1) + (z - d_2)\Theta(z - d_2) \\ & + (z + d_2)\Theta(z + d_2) - 2(z + a \log \cosh \frac{z}{a})]. \end{aligned} \quad (3.23)$$

In terms of  $\alpha$ -field (Fig.3.10)

$$\alpha^{(4w)}(\phi, z) = \begin{cases} \phi & \text{if } z > d_2 \\ \phi/2 & \text{if } d_2 > z > d_1 \\ 0 & \text{if } d_1 > z > -d_1 \\ -\phi/2 & \text{if } -d_1 > z > -d_2 \\ -\phi & \text{if } z < -d_2 \end{cases} \quad (3.24)$$

where the superscript (4w) stands for the four-wall configuration. For the determination of optimal core sizes, we use two different core sizes  $\zeta_1^{(4w)}$  and  $\zeta_2^{(4w)}$  for the pairs of symmetry related walls located at  $z = d_1$  and  $z = d_2$ .

We numerically minimise the total dimensionless free energy  $\mathcal{F}^{(4w)}$  with respect to the core sizes  $(\zeta_1^{(4w)}, \zeta_2^{(4w)})$  and the positions  $(\pm d_1, \pm d_2)$ , as functions of  $\eta$ . Plots of the minimised free energy, and the optimal core sizes are shown in Fig. 3.4 and Fig. 3.3 respectively. We find that the four wall configuration is unstable for  $\eta > 0.014$ . Within its stability range, the four-wall configuration has the lowest free energy. The optimised positions  $(D_1^{(4w)} = d_1/a, D_2^{(4w)} = d_2/a)$  are functions of  $\eta$ . Close to the stability range ( $\eta > 0.014$ ), the optimised positions have values such that the integrated Gaussian curvature between any two successive walls ( $K_T$ ) is  $-\pi$ . This trend similar to that of the two walls configuration. Here,  $D_1^{(4w)} \simeq 0.25, D_2^{(4w)} \simeq 0.97$ . We note that this behaviour holds for  $n$ -atic order.

### 3.4 Point disclinations in tetratic- and hexatic order

The symmetry of tetratic and hexatic order allows the disclinations with indices that are integer multiples of  $\pm 1/4$  and  $\pm 1/6$  respectively. In tetratic order, we consider eight  $s = -1/4$  disclinations on the catenoid. In this section we consider three simple configurations. In **Configuration-I**, we place four  $s = -1/4$  disclinations are placed in the  $z = d$  plane with angular separation of  $\pi/2$ , and four  $s = -1/4$  disclinations are located in the  $z = -d$  plane (with angular separation of  $\pi/2$ ) such that the position of disclination is rotated by

$\pi/4$  with respect to the position of disclination in  $z = d$  plane. For example the coordinates are  $\{ z = d ; \phi = j\pi/8, j = \{1, 3, 9 \& 11\} \}$ , and  $\{ z = -d ; \phi = k\pi/8, k = \{5, 7, 13 \& 15\} \}$  (Fig. 3.11(a)). **Configuration-II** has four  $-1/4$  disclinations are placed in the  $z = d$  plane with angular separation of  $\pi/2$ , and four  $s = -1/4$  disclinations are located in the  $z = -d$  plane (with angular separation of  $\pi/2$ ) such that position of disclinations is beneath the position of disclinations in  $z = d$  plane, eg,  $\{ z = \pm d ; \phi = j\pi/8, j = \{1, 3, 9 \& 11\} \}$  (Fig. 3.11(b)). **Configuration-III** has two disclinations are placed in the  $z = -3d$  plane with angular position  $\phi = 0, \pi$ , two at  $\{ z = -d; \phi = \pi/3, 4\pi/3 \}$ , two at  $\{ z = d; \phi = 2\pi/3, 5\pi/3 \}$ , and two at  $\{ z = 3d; \phi = 0, \pi \}$  (Fig. 3.11(c)).

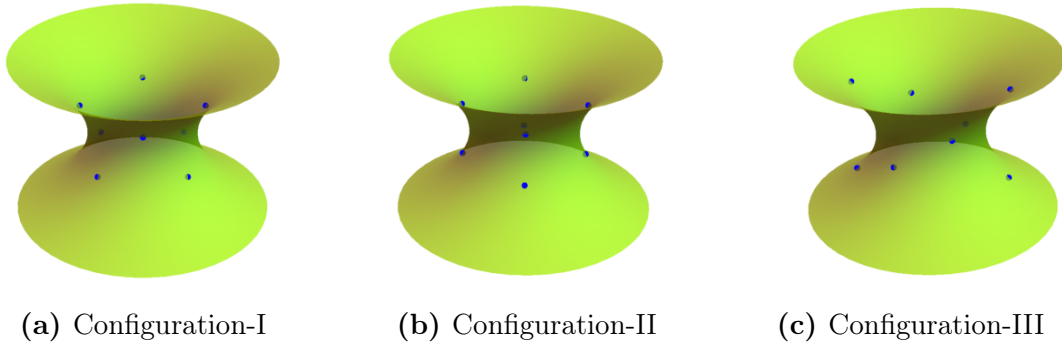


**Figure 3.11:** Arrangement of eight point disclinations of index  $-1/4$  each. The blue dots in all the figures represent the position of disclinations.

For tetratic order, numerically obtained plots of interaction energy (2.10) vs position of disclinations for the three configurations are shown in Fig.3.12. We find that the interaction is minimum for non zero  $d$ . Configuration-III has a local minimum in the potential plots at  $d \simeq 0.2$ , but it is not the global minimum. At  $d \simeq 0.45a$  Configurations-I and II have minimum potential energy. Interestingly, this value is closer to that of two wall disclination ( $d^{(2w)} \simeq 0.55a$ ). Configuration-I with  $d \simeq 0.45a$  has lowest free among the three configurations.

For hexatic order, **Configuration-I** has six  $s = -1/6$  disclinations placed in the  $z = d$  plane with angular separation of  $\pi/3$ , and six  $s = -1/6$  disclinations are located in the  $z = -d$  plane (with angular separation of  $\pi/3$ ) such that the position of disclinations is rotated by  $\pi/6$  with respect to the position of disclinations in the  $z = d$  plane ( eg,  $\{ z = d ; \phi = j\pi/12, j = \{1, 5, 9, 13, 17 \& 21\} \}$ ,  $\{ z = -d ; \phi = k\pi/12, k = \{3, 7, 11, 15, 19 \& 23\} \}$ ). In **Configuration-II**, six  $s = -1/6$  disclinations are placed in the  $z = d$  plane with angular separation of

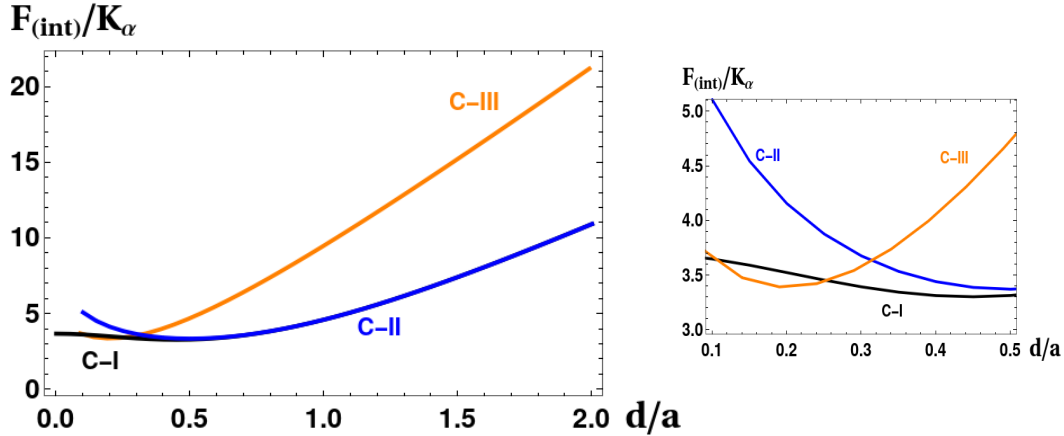


**Figure 3.12:** Interaction potential plots of tetratic order : Eight point disclinations of  $s = -1/4$  each. Black, blue and orange curves represent the configuration-I (C-I) , configuration-II (C-II), and configuration-III (C-III) respectively. Note that blue and black curves coincide for  $d > 0.5$ . The image on the left side shows the zoomed version of the three plots. It indicates that configuration-I with  $d \simeq 0.45a$  has the minimum interaction energy among the three.

$\pi/3$ , and six  $s = -1/6$  disclinations are located in the  $z = -d$  plane (with angular separation of  $\pi/3$ ) such that position of disclinations is beneath the position of disclinations in  $z = d$  plane ( eg,  $\{ z = \pm d ; \phi = j\pi/12, j = \{1, 5, 9, 13, 17 \ \& \ 21\} \}$  ). We ignore **Configuration-III** for the energetic considerations. As the disclinations in C-III are more distributed, the interaction among them is not predominant as compared to C-I and C-II. The interaction potential plots for C-I and C-II are given in Fig. 3.13. It is clear that configuration-I with  $d \simeq 0.5a$  is the lowest energy state and configuration-II has a local minimum at  $d \simeq 0.5a$ . We note that equilibrium positions of point disclinations in tetratic and hexatic order is close to that of two wall disclinations ( $d \simeq 0.55a$ ).

### 3.5 $n$ -atic order: Division of total Gaussian curvature by wall disclinations

In this section we generalise the calculations of the division of total Gaussian curvature to  $n$ -atic order. It is clear that, for  $n$ -atic order on catenoid, the lowest allowed disclination index is  $s = -1/n$ . We consider  $2n$  walls of index  $s = -1/n$  each, and indicate the positions of symmetry related pairs of walls by  $(d_k, d_{-k} =$

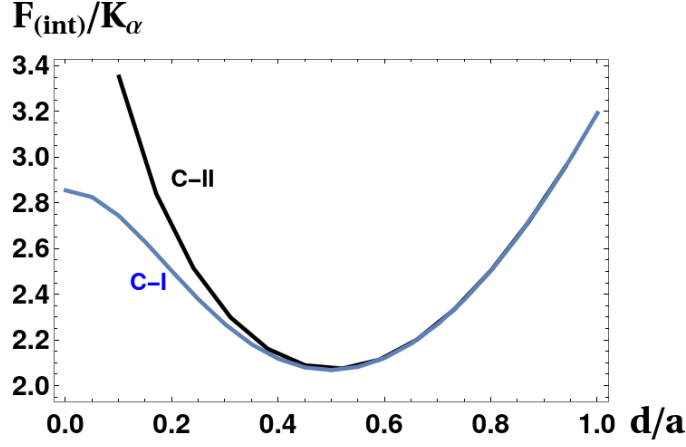


**Figure 3.13:** Plots of interaction potential for hexatic order : Twelve point disclinations of  $s = -1/6$  each. Blue and black curves represent Configuration-I (C-I) and Configuration-II (C-II) respectively. It indicates that Configuration-I with  $d \simeq 0.5a$  has the minimum interaction energy among the three.

$-d_k$ ), where  $k = 1, 2, \dots, n$ . The disclination density of this configuration is

$$\mathcal{S}(z) = -\frac{1}{n\sqrt{g}} \sum_{k=1}^n [\delta(z - d_k) + \delta(z - d_{-k})]. \quad (3.25)$$

To get optimal position of the walls, we use the Coulomb gas free energy (Eq. 2.9). After substituting for Green's function (Eq. 3.16) in Eq. 2.9, minimisation of elastic free energy with respect to the positions  $d_i$  leads to  $\int_{-d_i}^{d_i} dz \sqrt{g} K(z) = -(2i - 1)/n$  (See Appendix B for more details). Therefore, the integrated Gaussian curvature between the symmetry-related walls at  $d_i$  and at  $-d_i$  ( $K_i$ ) is

$$\begin{aligned} K_i &= 2\pi \int_{d_i}^{-d_i} dz \sqrt{g} K(z) \\ &= -\frac{2\pi}{n} (2i - 1). \end{aligned}$$

After some algebraic manipulations we get the integrated Gaussian curvature between any two successive walls

$$K_{\text{T}}(i, i + 1) = 2\pi \int_{d_i}^{d_{i+1}} K(z) \sqrt{g} dz = -2\pi/n, \quad (3.26)$$

where  $i = \{1, 2, \dots, 2n - 1\}$ . Thus for  $n$ -atic order, the lowest *elastic free-energy* configuration has  $2n$  walls of index  $-1/n$  each, located such that the integral of Gaussian curvature of the catenoid between any two successive walls is  $-2\pi/n$ .

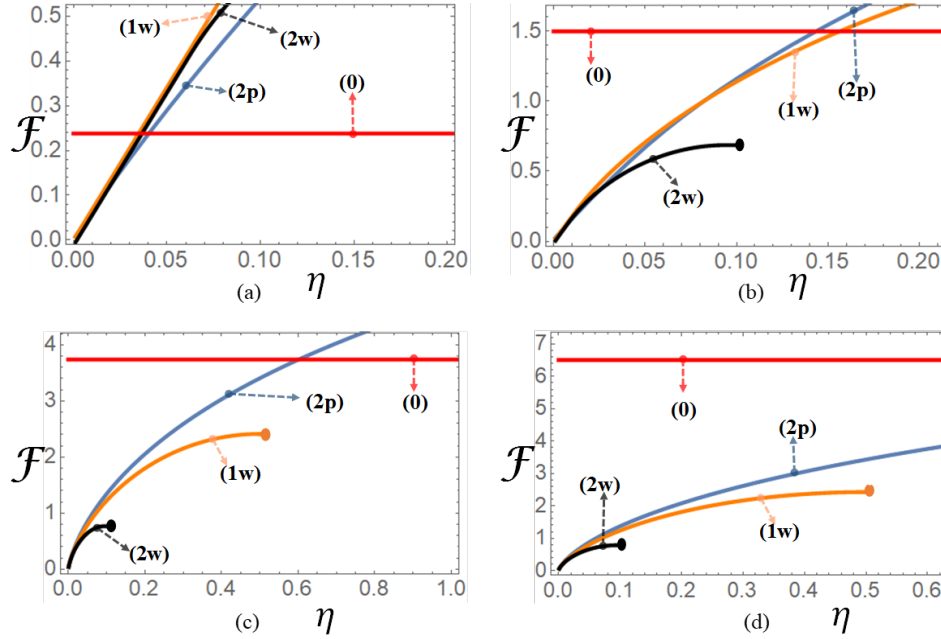


**Figure 3.14:** Minimised free energy  $\mathcal{F}$  of finite sized catenoid: Total height in (units of the neck radius  $a$ ) of the catenoid is  $2\mathcal{L}$ . The dots indicate  $\eta$ -values beyond which wall defects are unstable ( $\zeta(\eta) = 0$ ). (a)  $\mathcal{L} = 0.5$ , (b)  $\mathcal{L} = 1$ , (c)  $\mathcal{L} = 1.5$  and (d)  $\mathcal{L} = 2$ .

### 3.6 Finite sized catenoid

The results on stability of wall disclinations, and on the division of Gaussian curvature discussed above are valid for infinite catenoids (infinite  $l$ , finite  $a$ ). In experiments, only catenoids with finite  $l$  can be studied. For finite height of the catenoid, there are two circular boundaries. In this section we consider catenoids with finite  $l$  and  $a$ , and investigate the stability of two point disclinations ( $s = -1$  each), single wall ( $s = -2$ ) and two wall-configuration ( $s = -1$  each). We now minimise the total free energy  $\mathcal{F}$  with free boundary conditions on the circular boundaries by keeping a upper limit for the core size along  $z$ -direction. The plots of minimised  $\mathcal{F}$  as a function of  $\eta$  are shown in Fig.3.14 for the dimensionless height  $\mathcal{L} = 0.5, 1, 1.5$  and  $2$ .

We note that for  $\mathcal{L} < 0.5$ , there is a transition from disorder phase to disclination-free configuration as a function of  $\eta$ . The critical value  $\eta^*$ , at which this transition occurs, depends on the  $\mathcal{L}$ . For  $\mathcal{L} = 0.5$ ,  $\eta^* \simeq 0.03$ . We observe that in the range  $0.5 < \mathcal{L} < 0.78$ , the two-wall configuration is stable and it is an intermediate configuration in the transition from disorder to disclination free configuration. The upper limit  $\mathcal{L} = 0.78$  is obtained by comparing the elastic free energy ( $F_\alpha$ ) of the two-wall configuration to that of disclination-free configuration. The single wall disclination is stable in the range  $0.78 < \mathcal{L} < 1.23$ , and the transition as a function of  $\eta$  is as follows : disorder  $\rightarrow$  two-wall  $\rightarrow$  single wall  $\rightarrow$  disclination-free configuration. The limit  $\mathcal{L} = 1.23$  is obtained by comparing the elastic free energy  $F_\alpha$  of the single wall configuration to that of disclination-free configuration.

### 3.7 Results and discussion

This chapter shows that wall disclinations are stable on the surface of a catenoid close to order-disorder transition. Similar to spherical surfaces, the wall disclinations divide the Gaussian curvature equally (the division of Gaussian curvature). For a finite-sized catenoid, we predict a transition from uniform to wall disclinations configuration as a function of the height of the catenoid. There is a transition from two-wall configuration to single wall configuration as a function of temperature for catenoids of fixed height. It is interesting to test our predictions for finite-sized catenoids. The height scales are large enough such that one may avoid the faceting problem that occurs for deformable spherical surfaces.

## Chapter 4

# Point- and wall disclinations on Helicoids

### 4.1 Introduction

In this chapter, we discuss the point and wall disclinations on helicoids, another example of minimal surfaces. When helical spring is immersed in soap solution, the soap film acquires the helicoid shape. Helicoids and catenoids are members of the same associate family of minimal surfaces, hence, one can bend a catenoid into a portion of a helicoid without stretching [20]. Mathematically, there is a distance-preserving transformation between the catenoid and portion of the helicoid (locally isometric). Thus, our results for catenoidal membranes are mapped to helicoidal membranes.

To begin with, we discuss the geometry of helicoid and establish the  $\alpha$ -field for point disclinations. The isometric mapping of helicoid to catenoid is studied in the Sec. 4.3.

### 4.2 Point disclinations

We parametrise a right handed helicoid as  $\mathbf{R}(\phi, r) = \{r \cos \phi, r \sin \phi, b \phi\}$  where  $-\infty < r < \infty$  and  $0 \leq \phi < 2\pi$ . Here  $2\pi b$  is pitch of the helicoid. The components of the metric tensor are  $g_{\phi\phi} = (b^2 + r^2)$ ,  $g_{rr} = 1$ ,  $g_{\phi r} = g_{r\phi} = 0$ , and the determinant of metric tensor  $g = (b^2 + r^2)$ . The Gaussian and mean curvature are, respectively,  $K = -b^2/(b^2 + r^2)^2$ , and  $H = 0$ .

We choose  $\hat{\mathbf{e}}_1(\phi, r) = \hat{\mathbf{t}}_\phi(\phi, r)$  and  $\hat{\mathbf{e}}_2(\phi, r) = \hat{\mathbf{t}}_r(\phi, r)$  to express any tangent vector  $\hat{\mathbf{m}}(\phi, r)$  on the helicoid as  $\hat{\mathbf{m}}(\phi, r) = \cos \alpha(\phi, r) \hat{\mathbf{e}}_\phi + \sin \alpha(\phi, r) \hat{\mathbf{e}}_r$ . In this coordinate system the components of spin connection terms are  $\mathbf{A} = (A_\phi, A_r) = (0, r/\sqrt{b^2 + r^2})$ .

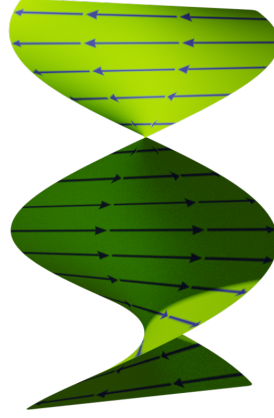


**Figure 4.1:** The disclination-free configuration

For the disclination free configuration,  $\alpha = \text{const}$ . The corresponding texture is shown in Fig. 4.1. With free boundary conditions, the elastic free energy of the helicoid of width  $2w$  is

$$F_{\text{el}} = \pi K_\alpha \left[ \log\left(\frac{\sqrt{w^2 + b^2} + w}{\sqrt{w^2 + b^2} - w}\right) - \frac{2w}{\sqrt{w^2 + b^2}} \right]. \quad (4.1)$$

Note that  $F_{\text{el}}$  diverges logarithmically as  $w \rightarrow \infty$ . Thus the disclination-free configuration is untenable for a helicoid with infinite extent (fixed  $b$  and  $w \rightarrow \infty$ ). Since  $\int_0^{2\pi} d\phi \int_{-\infty}^{\infty} K \sqrt{g} dr = -4\pi$ , we consider point disclinations of total index  $s = -2$  on an infinite helicoid. The  $\alpha$ -field for a pair of two  $s = -1$  disclinations at  $r = 0$  and  $\phi = \{\pi/2, 3\pi/2\}$  is

$$\alpha_{\text{h}}^{(2\text{p})}(\phi, r) = \arctan\left(\frac{r \tan \phi}{\sqrt{r^2 + b^2}}\right), \quad (4.2)$$

where the superscript (2p) refers to two point disclinations. This expression is obtained by the intersection of the helicoidal surface with  $x = \text{const}$  planes (level sets), and satisfies the  $\alpha$ -equation of the equilibrium (Eq. 1.13). The streamlines for this configuration are depicted in Fig. 4.2(a). From Eq. 2.5, the elastic free

energy density of this configuration is

$$f_{\text{el}}^{(2\text{p})}(\phi, r) = \frac{K_\alpha b^4 \sin^2 \phi}{(b^2 + r^2)^2 (b^2 + 2r^2 + b^2 \cos 2\phi)}. \quad (4.3)$$

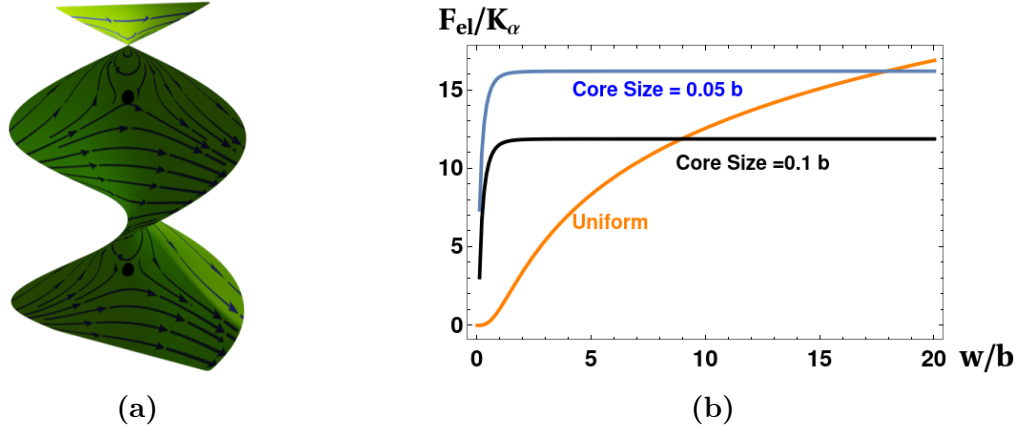


**Figure 4.2:** (a) Streamlines of two  $s = -1$  point disclinations on the axis of a helicoid ( $r = 0$  ;  $\phi = \pi/2, 3\pi/2$ ). (b) The plot of  $F_{\text{el}}$  (in  $K_\alpha$  units) vs  $w/b$  : Orange color curve is for uniform configuration. Blue- and black curves represent the elastic free energy of two point disclinations with core sizes (or, cutoffs)  $0.05b$  and  $0.1b$ , respectively.

It is evident that at  $r = 0$  and  $\phi = \{\pi/2, 3\pi/2\}$ , the elastic free energy density  $f_{\text{el}}^{(2\text{p})}$  has singularities. We use equal cutoffs in  $r$ - and  $\phi$ -directions for calculating the elastic free energy ( $F_\alpha$ ). Fig. 4.2(b) shows the plot of elastic free energy (in the units of  $K_\alpha$ ) of two point disclination configuration for fixed core area around point disclinations. For example, for the blue curve the cutoff in the  $r$ -direction is  $0.05b$ , and for the  $\phi$ -direction it is  $0.05$  rad (See, Fig. 4.2(b)). We note that for fixed core area, the elastic free energy for the (2p) saturates for large  $w$ .

For nematic order, we consider four  $s = -1/2$  point disclinations in two configurations. **Alternating configuration (A-I)**, the disclinations are placed at  $r = -\rho$  ;  $\phi = \{\pi/4, 5\pi/4\}$  and  $r = \rho$  ;  $\phi = \{3\pi/4, 7\pi/4\}$  (Fig. 4.3(a)). **Atop configuration (A-II)** has disclinations placed at  $r = \pm \rho$  ;  $\phi = \{\pi/4, 5\pi/4\}$  (Fig. 4.3(b)). The interaction potential energy plots of the two configurations are given in Fig. 4.4(a). We note that A-II has a local minimum around  $\rho \simeq 0.5 b$ , however, A-I with  $\rho = 0$  has the lower energy. The corresponding  $\alpha$ -field is (See



(a) Alternating configuration (A-I)

(b) Atop configuration (A-II)

**Figure 4.3:** Arrangement of four point disclinations of index  $s = -1/2$  each. The blue dots in the figures represent the position of disclinations.

Fig. 4.4(b))

$$\alpha_h^{(4p)}(\phi, r) = \frac{1}{2} \left[ \operatorname{arccot} \left( \frac{r \tan(\phi + \pi/4)}{\sqrt{r^2 + b^2}} \right) - \operatorname{arccot} \left( \frac{r \cot(\phi + \pi/4)}{\sqrt{r^2 + b^2}} \right) \right] \quad (4.4)$$

where the superscript (4p) indicates four point disclinations.

To study the point disclinations in tetratic order, we use two configurations in which eight  $s = -1/4$  disclinations are arranged as follows: **Configuration-I** has disclinations at  $r = \rho$ ;  $\phi = k\pi/8$  where  $\{k = 1, 3, 9 \text{ and } 11\}$ , and  $r = -\rho$ ;  $\phi = j\pi/8$  where  $\{j = 5, 7, 13 \text{ and } 15\}$ . In **Configuration-II** they are placed at  $r = \pm\rho$ ;  $\phi = k\pi/8$ , where  $\{k = 1, 3, 9 \text{ and } 11\}$ . Interaction potential energy plots of these two configurations are shown in Fig. 4.5. Note that Configuration-I with  $\rho \simeq 0.475 b$  has minimum interaction energy.

For hexatic order, we consider two configurations in which twelve  $s = -1/6$  disclinations are arranged as follows: **Configuration-I** has disclinations at  $r = \rho$ ;  $\phi = k\pi/12$  where  $j = \{1, 5, 9, 13, 17 \text{ and } 21\}$ ,  $r = -\rho$ ;  $\phi = j\pi/12$  where  $j = \{3, 7, 11, 15, 19 \text{ and } 23\}$ . In **Configuration-II**, they are placed at  $r = \pm\rho$ ;  $j = \{1, 5, 9, 13, 17 \text{ and } 21\}$ . Interaction potential energy plots of these two configurations are shown in Fig. 4.6. Note that Configuration-I with  $\rho \simeq 0.5 b$

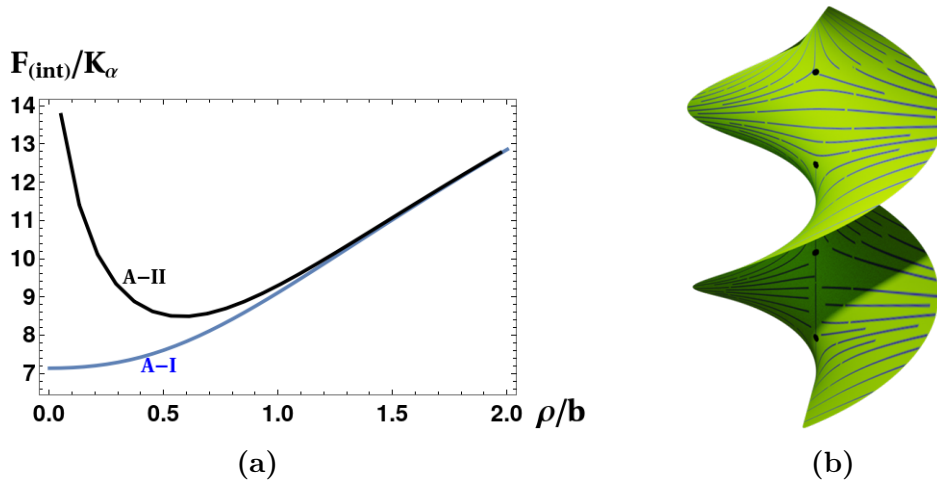


**Figure 4.4:** (a) Interaction potential energy plots of point disclination in nematic order: Blue and black curves are for Alternating (A-I) and Atop (A-II) configurations. (b) Streamlines of four point disclinations placed on the axis of the helicoid ( $\rho = 0$ ;  $\phi = \pi/4, 3\pi/4, 5\pi/4$  and  $7\pi/4$ ).

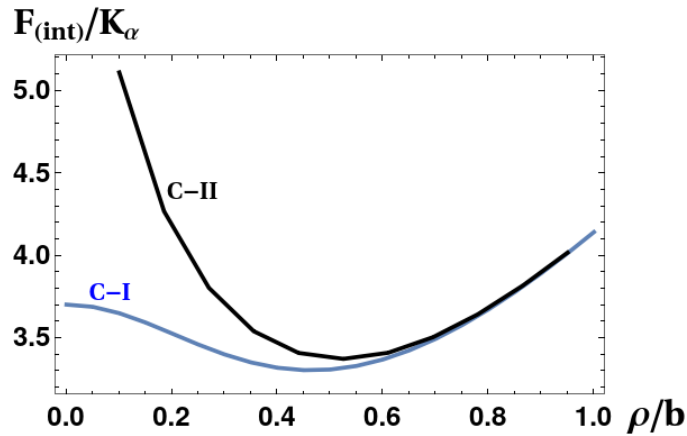


**Figure 4.5:** Interaction potential energy plots of tetratic order : Blue and black color curves represent the Configuration-I (C-I) and Configuration-II (C-II) respectively. It indicates that configuration-I with  $\rho \simeq 0.475 b$  has the minimum interaction energy.

has minimum interaction energy.

### 4.3 Wall disclinations

In Chapters 2 and 3, we established a general procedure to get  $\alpha$ -field for wall disclinations (solve for the compatibility condition). In this section we make

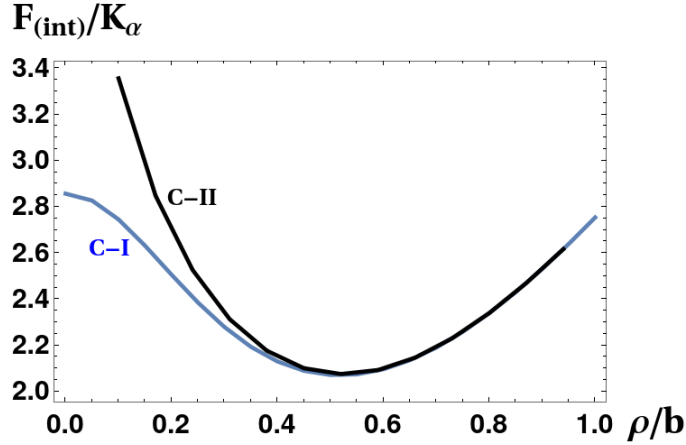


**Figure 4.6:** Interaction potential plots for hexatic order : Twelve point disclinations of  $-1/4$  each. Blue and black color curves represent the configuration-I (C-I) and configuration-II (C-II) respectively. It indicates that configuration-I with  $\rho \simeq 0.5 b$  has the minimum interaction energy.

use of isometric mapping between a helicoid and a catenoid to study the wall disclinations on helicoids. The isometric transformation of a helicoid of one pitch (pitch length  $2\pi b$ ) to catenoid (of neck radius  $a$ ) and is given by [20, 21]

$$\begin{aligned}
 b &\rightarrow a \\
 r &\rightarrow a \sinh\left(\frac{z}{a}\right) \\
 \phi &\rightarrow \phi
 \end{aligned} \tag{4.5}$$

The parametrisation of helicoid after the transformation is

$$\mathbf{R}(\phi, z) = \{ a \sinh(z/a) \cos \phi, a \sinh(z/a) \sin \phi, a\phi \} \tag{4.6}$$

In this parametrisation, the metric ( $g_{\mu\nu}$ ), mean ( $H$ ) and Gaussian ( $K$ ) curvatures take the same form as that for catenoid (See Appendix B).

To understand the transformation effects on  $\alpha$ -field, we consider two point disclinations of index  $s = -1$ . Under the isometric mapping,  $\alpha_h^{(2p)}$  transforms to

$$\begin{aligned} \alpha_h^{(2p)}(\phi, z) &= \arctan(\tan \phi \tanh(z/a)) \\ &= \begin{cases} \pi/2 - \arctan(\cot \phi \coth(z/a)), & \text{if } \cot \phi \coth(z/a) > 0 \\ -\pi/2 - \arctan(\cot \phi \coth(z/a)), & \text{if } \cot \phi \coth(z/a) < 0 \end{cases} \quad (4.7) \\ &= \pm \frac{\pi}{2} + \alpha^{(2p)} \end{aligned}$$

where  $\alpha^{(2p)} = -\arctan(\cot \phi \coth(z/a))$  is the  $\alpha$ -field for two  $s = -1$  point disclinations on catenoid (see Eq. 3.2). Thus  $\alpha$ -field acquires constant angle which manifests conformal nature of the mapping.

Recall that the optimal positions of point disclinations for tetratic order on catenoid is Configuration-I with  $d \simeq 0.45 a$ . With the transformation we get  $\rho = b \sinh(0.45) = 0.465 b$ , which is close to the value from the potential plots of tetratic order on helicoid with Configuration-I ( $\rho \simeq 0.475 b$ , see Fig. 4.5).

For more general cases, we consider new parametrisation (Eq. 4.6) of helicoid that is isometric to catenoid. We take orthonormal coordinates  $\hat{\mathbf{e}}_1(\phi, z) = \hat{\mathbf{t}}_\phi(\phi, z)$  and  $\hat{\mathbf{e}}_2(\phi, z) = \hat{\mathbf{t}}_z(\phi, z)$ . The spin connection is  $\mathbf{A} = (A_\phi, A_z) = (\tanh(z/a), 0)$ . Thus a tangent vector  $\hat{\mathbf{m}}(\phi, z)$  on helicoid is  $\hat{\mathbf{m}}(\phi, z) = \cos \alpha(\phi, z) \hat{\mathbf{e}}_\phi + \sin \alpha(\phi, z) \hat{\mathbf{e}}_z$ . As the mapping is isometric and conformal, we take  $\alpha$ -field of different configurations on catenoid and use them directly onto helicoid. For example,  $\alpha^{(2p)}$  represents orientational field for two  $s = -1$  disclinations at  $z = 0$  ( $\rho = 0$ ) and  $\phi = \{\pi/2, 3\pi/2\}$  on a helicoid. Similarly, Eq. 3.10 represents  $\alpha$ -field for the single wall (at  $z = 0$ ) of index  $s = -2$  (Fig. 4.7(a)). The two wall-, four wall-configurations on a helicoid is depicted in Fig. 4.7.

## 4.4 Stability analysis of point- and wall disclinations

Preceding sections discuss the interaction potentials for point and wall disclinations. In what follows, we take into account of core energy calculations and minimise the total free energy. To address the stability analysis of point disclinations and equilibrium core sizes on helicoid, we use the isometric transformation

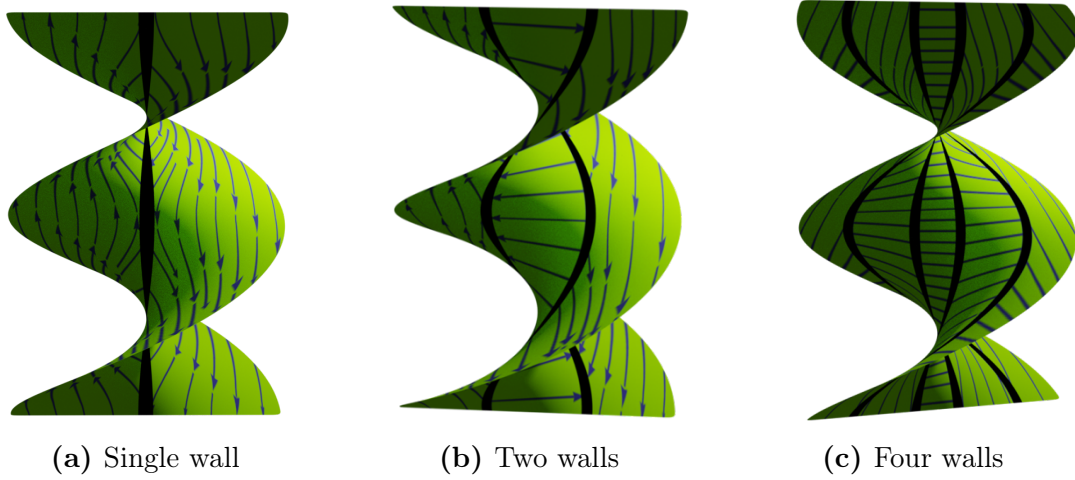


**Figure 4.7:** Streamlines of wall disclination(s) on a helicoid:(a) Single wall disclination with index  $s = -2$  placed on the axis of helicoid. (b) Two wall disclinations of index  $s = -1$  each. (c) Four wall disclinations of index  $s = -1/2$  each. The shaded regions in these figures depict core regions.

between helicoids and catenoids. Note that the metric, spin connection term and  $\alpha$ -field is the same as that for a catenoid (See Appendix B). Therefore free energy expressions, core calculations are identical to that of catenoid configuration. As the results for catenoid are discussed in the previous chapter, the transformation ensures that helicoid results are mapped to catenoid.

We begin by considering half width of helicoid  $w = a \sinh[l/a]$ , where  $l$  is the half height of the catenoid to which the helicoid is mapped. With this transformation free elastic energy of disclination-free configuration turns to

$$F_{\text{el}}^{(0)} = 2\pi K_{\alpha} \left[ \frac{l}{a} - \tanh\left(\frac{l}{a}\right) \right] \quad (4.8)$$

Note that the expression is the same as that of catenoid (See Eq. 3.1).

The  $\alpha^{(2p)}$  represents orientational field for two  $s = -1$  disclinations at  $z = 0(\rho = 0)$  and  $\phi = \{\pi/2, 3\pi/2\}$  on helicoid. The free elastic energy density is

$$f_{\text{el}}^{(2p)} = \frac{K_{\alpha} \sin^2(\phi) \operatorname{sech}^4(z/a)}{a^2 [\cosh(2z/a) + \cos(2\phi)]} \quad (4.9)$$

which exactly matches with that of catenoid. We also use the same parameter  $\eta$  as in the case of catenoid. By taking core sizes  $\zeta_z^{(2p)}$ ,  $\zeta_{\phi}^{(2p)}$  that are identical

to catenoid, we numerically obtain optimal core sizes around point disclinations (Fig 3.3). Similarly, optimal core sizes for four point disclinations ( $\zeta_z^{(4p)}$ ,  $\zeta_\phi^{(4p)}$ ) placed at  $z = 0$  and  $\phi = k\pi/4$  where  $k = \{1, 3, 5 \text{ and } 7\}$  are given in Fig 3.3. The minimised free energy plots are shown in Fig. 3.4

For wall disclinations, equilibrium positions are obtained by division of Gaussian curvature rule. The optimal cores and minimised free energy of single wall (1w), two walls (2w) and four walls (4w) configurations is shown in Fig 3.3 and Fig 3.4 respectively. We note that the wall disclinations are stable near order disorder transition. The finite size effects of helicoid follow catenoid results. For finite sized helicoid of radius  $r$ , the transformation  $r = a \sinh(\mathcal{L})$  mimics the finite sized catenoid results. Our predictions can be tested experimentally.

To summarise, Part-I studies the stability of wall disclinations on spheres, catenoids, and helicoids. Non zero Gaussian curvature is an essential feature for the stability of wall disclinations. We attribute their stability to free-energetic considerations, which override those of topological stability. We note that our model is based on mean-field theory and neglects thermal fluctuations. However, fluctuations play a vital role near the order-disorder transition, where the wall disclinations are stabilised. Investigating the stability of wall disclinations in the presence of thermal fluctuations and the role of wall disclinations in defect mediated Kosterlitz-Thouless (KT) transitions are interesting challenges. These could be possible direction for future work.



## Part II

Sector-, and tent morphologies of  
polymer crystallites



## Chapter 5

# The sector morphology of polymer crystallites

### 5.1 Introduction

Part-II of this thesis (Chapters 5, 6) discusses the role of topological defects in determining the observed sector- and tent-morphologies of polymer crystallites. This is a collaborative work with Prof. M. Muthukumar (University of Massachusetts Amherst, USA) and Dr. Jaya Kumar A (IISc, Bengaluru, India). In this chapter we review and improve the calculations of the model proposed by Jayakumar et al. for the stability of sector morphology [5]. This chapter is the foundation for the study of tent morphology in which stability analysis of sectors plays a vital role. In what follows, we begin by giving introduction to polymer crystallites.

Polymer crystals are fascinating because these are formed by long, entangled, and interpenetrating chains. There is a topological frustration that the polymer chains need to overcome for settling into crystalline order. The frustration arises from the highly entangled collection of interpenetrating, connected chains with long-ranged spatial and dynamic correlations before crystallisation begins. The chains have large free energy barriers to reorganise polymer conformations into the ordered states [50]. Interestingly, polymer crystallisation suppresses the topological frustration [51, 52]. Because of the *connectedness*, polymer crystals are different from regular atomic and molecular crystals. In contrast to regular crystals in three-dimensions, polymer crystals do not grow to an infinite extent in all three-dimensions. Due to free energetic considerations, polymer crystals are

formed as lamellae [53, 54]. The free energy minimum corresponding to finite lamellar thickness maximises configurational entropy. This is because there are numerous ways of distributing a given chain length into many loops.

Observed morphologies of polymer crystallites show spherulitic, and twisted spherulitic structures composed of helicoids, tent-like structures and scroll structures [4]. The schematics of these structures are shown in Fig. 5.1. An exciting feature of these structures is that they are lamellar in nature. The typical thickness of a single lamella is in order of 10 nanometers and lateral dimensions of about micrometers or above. Among various models, the adjacent-reentry fold model (proposed by Keller [55]) is widely accepted to explain the structure of lamella through polymer chains [The Faraday Division, Royal Society of Chemistry, London, 1979]. According to this model, parts of polymer chains form rigid stem-like structures attached to adjacent stems by flexible folds in the polymer. These stems offer crystalline order by arranging on a lattice (See Fig. 5.2). Depending on growth conditions, stems can align either along the lamellar normal or at an angle with respect to it. The lamella also comprises flexible chains like cilia and hair-like microscopic structures (See Fig. 5.2). It is the configurational entropy of the cilia structures that stabilises finite lamellar thickness.

A review of experimental and theoretical advances in polymer crystals is given in the articles by Lotz and Cheng [4], and by Crist and M.Schultz [56]. The review discusses the study of growth, branching and twisting of polymer crystals. Interestingly, polarised optical microscopic images with periodic bands of many *achiral* polymers such as polyethylene (PE) show that they crystallise into chiral structures. These chiral structures are arising from the twisting of the lamellae making up the spherulites. A theoretical study of chiral symmetry breaking of achiral polymers with a new approach involving topological defects is developed by Yashodhan Hatwalne and Muthukumar [57]. This new approach is the starting point for the work done Part-II of the thesis. Our work focuses on the morphologies of single lamellar crystallites obtained from solution-grown and melt-grown conditions. Below we give experimental facts and observations of polymer single crystallites.

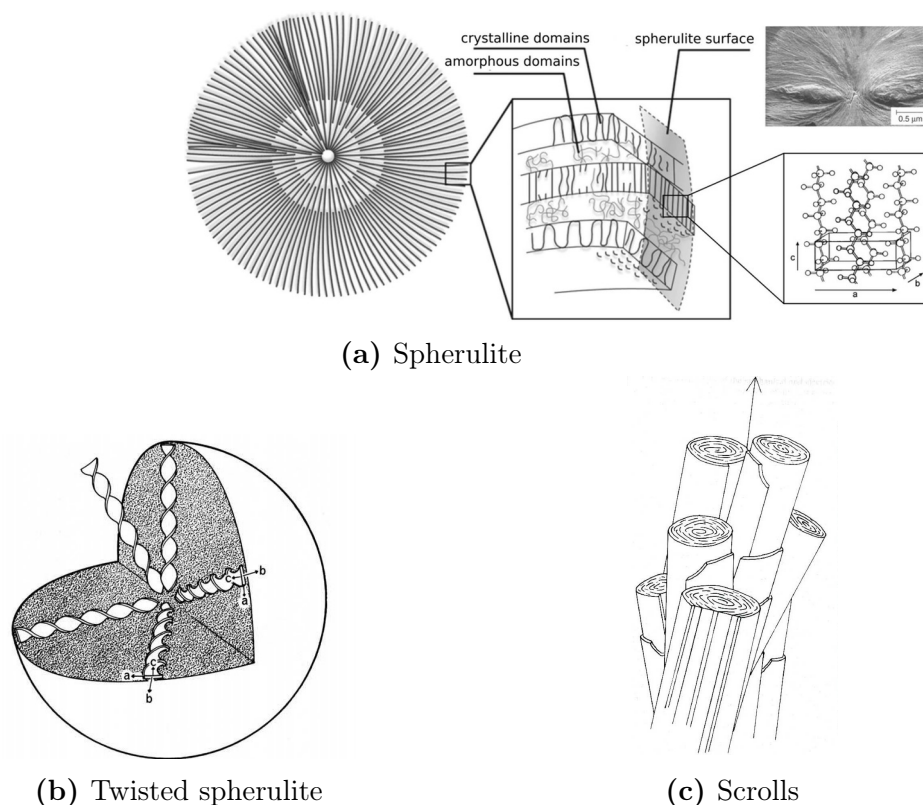


**Figure 5.1:** Morphologies of polymer crystallites. (a). Spherulite: Schematic representation of spherulite obtained by radially growing polymer lamellae. The first magnified image illustrates the lamellar structure and second magnified image shows the crystalline arrangement. Image credits: Dingler et.al, *Macromol. Rapid Commun.* 2019. (b). Twisted spherulite: Polymer lamellae twisted in the form of helicoids. (c) Scroll: Lamellae are rolled over. Images (b) and (c) are borrowed from Ref [4].

## 5.2 Experimental observations of polymer single crystallites

Crystallisation from a solution containing sufficiently long and unentangled flexible polymer molecules are observed to form diverse morphologies such as flat sectors, hollow tents, disks, onion-like scrolls, and twisted morphologies [58, 59, 60, 61]. Transmission electron microscopy (TEM) images of solution-grown single crystals are shown in Fig. 5.3. The size, shape, and regularity of sectors depend on growth conditions such as solvent, temperature, growth rate, and solution concentrations, etc. For examples, flat lozenge-shaped lamellae are formed

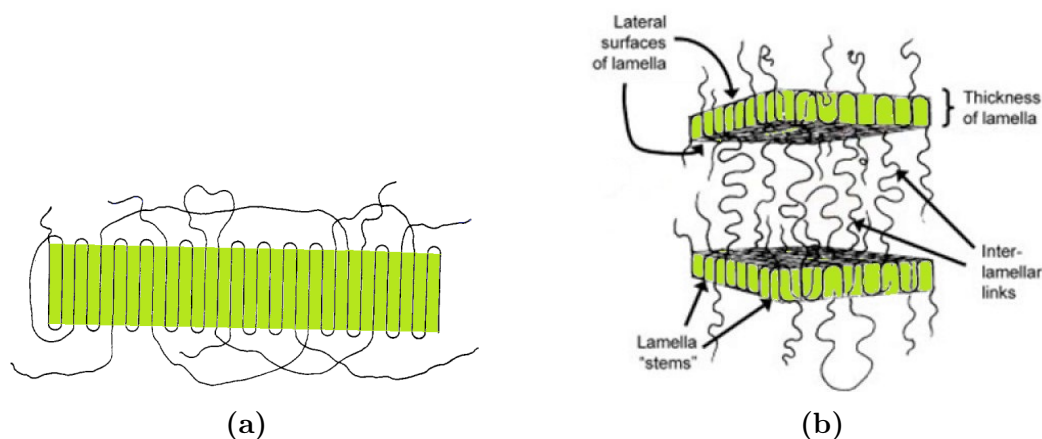


**Figure 5.2:** Adjacent re-entry model: (a) Schematic representation of adjacent re-entrant folds. The free polymer chains resemble cilia, microscopic hairlike vibrating structures (b) Schematic of lamellar stack with adjacent re-entrant folds. Images are taken from the internet.

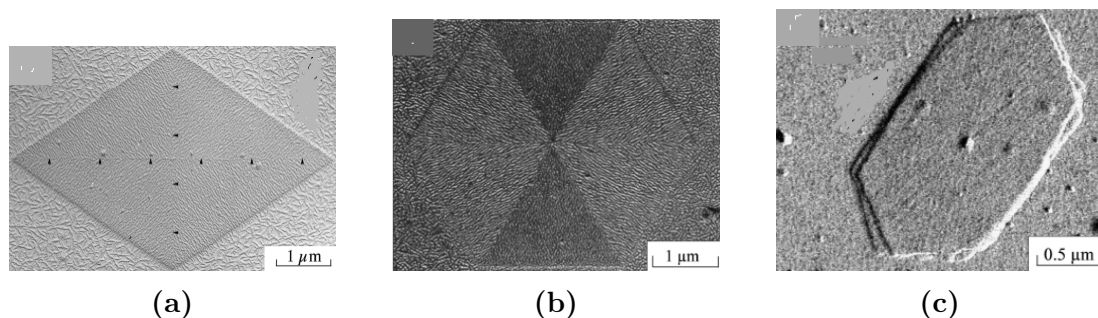


**Figure 5.3:** TEM images of solution-grown single crystals: (a) Lozenge shape sector: Linear polyethylene crystal decorated with polyethylene vapour. (b) Hexagonal sector: Polyoxymethylene single crystal decorated with polyethylene vapour. Images (a) and (b) are borrowed from Wittmann and Lotz (1985). (c) Poly( $\epsilon$ -caprolactone) crystal grown from a *n*-hexanol solution at 40C. (Image is taken from Nunez and Gedde (2005))

when polyethylene is crystallized from a mixture of tetrachloroethylene and *p*-xylene [52] and flat hexagonal-shaped lamellae are formed when polyoxymethylene is crystallized from bromobenzene [60]. Schematics of the lozenge and hexagonal morphology are depicted in Fig. 5.4. An example for temperature dependence is when polyethylene is crystallized from *p*-xylene at 70<sup>0</sup>C, lozenge-shaped lamella (with four sectors with [110] growth planes) forms and at 86<sup>0</sup>C, hexagonal-shaped lamella (with six sectors, four with [110] planes and two with [100] planes) forms. It is also known that {100} sectors have a lower melting temperature than

the  $\{110\}$  sectors.

Generally, polymer crystallites have different point group symmetries and preferred tilt and fold angles (See Fig. 5.5). In addition to this structural complexity, a finite lamella with a boundary has anisotropic line tension [9, 62]. Even though macroscopic structures such as sectors and tents are observed experimentally, there was no clear understanding of their stability till the work by Jaya Kumar et al. In this chapter, we improve the calculation presented in Jaya Kumar et al work. We use concepts borrowed from liquid-crystal physics and the physics of crystalline membranes to study the sector- and the tent morphologies. We note that our model focuses on structural, and topological aspects of the observed configurations, but does not address the detailed experimental conditions such as particular solvents, growth rate, and temperature etc. We treat the problem of the structure of polymer configurations assuming mechanical and thermodynamical equilibrium. In what follows we discuss the model for sector morphology.

### 5.3 A model for the sector morphology

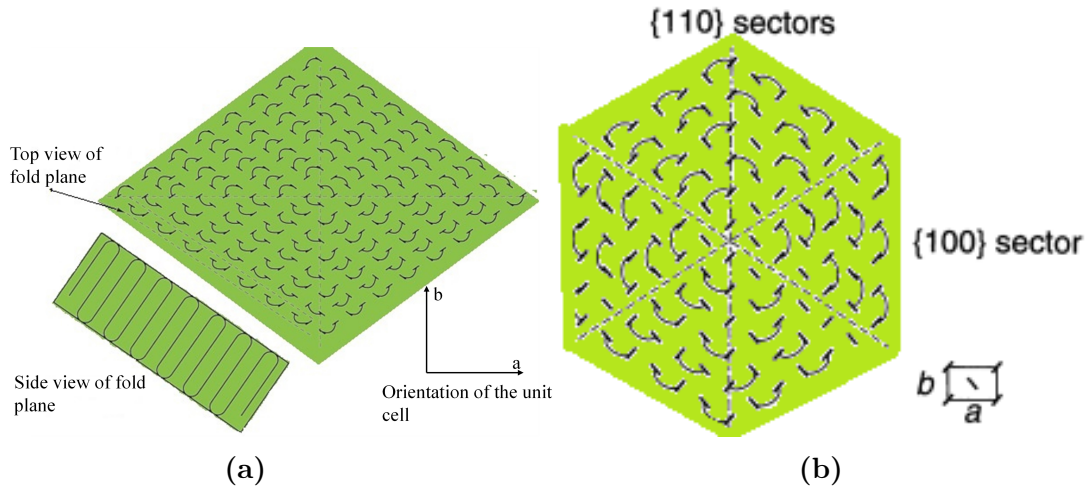


**Figure 5.4:** Schematic illustration of folds at the surface of polymer lamella in sector configuration: (a) Lozenge shaped sector: It has four  $\{110\}$  sectors. (b) Hexagonal sector: It has four  $\{110\}$  sectors and two  $\{100\}$  sectors. Here vectors  $a, b$  are the crystal axes.

For concreteness, and simplicity we begin by considering polyethylene (PE) crystallite as an example. The chemical formula for polyethylene monomer is  $C_2H_4$ . In the crystalline state, PE lamella is in base-centred orthorhombic symmetry. The stems are tilted with respect to lamella normal by about 30 degrees (See Fig. 5.5(a)). We note that the stems are in the trans-configuration, and the folds are in the gauche-configurations (See Fig. 5.5(b)). In general, a single polymer crystal has in-plane

- crystalline order from polymer stems,
- tilt order of polymer stem, and
- orientational order from the fold field.

In what follows that we discuss the elasticity theories of crystalline order and stem field, and present a phenomenological model for folds.

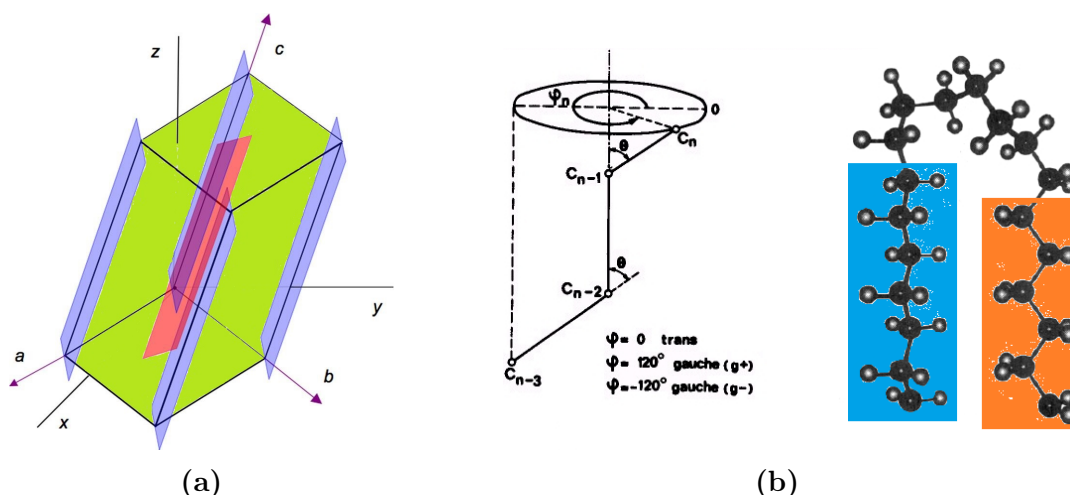


**Figure 5.5:** (a). Schematic illustration of unit cell of a crystalline polyethylene lamella. The unit cell has symmetry of base-centered orthorhombic. Here  $a$ ,  $b$  and  $c$  represent the the crystal axes and lamella is  $xy$ -plane with lamellar normal is along the  $z$  axis. Note that the  $c$  axis of the unit cell is tilted with respect to the  $z$  axis. Blue and red colored shaded strips represent oriented stems formed by the all-trans configurations. Folds are not shown. Image is taken from Ref [5]. (b) Cartoon showing trans-gauche configurations of polyethylene and fold formation. Image is taken from S.P.Schmm et al., macromolecules, (1994).

### 5.3.1 Crystalline order: Hookian elasticity

To simplify the problem, we treat polymer lamella as a thin crystalline plate, or membrane that uses continuum elastic theory (plate theory) [18]. Deformations in crystalline order of a flat lamella in  $x y$ -plane are described by two-dimensional displacement vector  $\mathbf{u}(x, y) = \{u_x(x, y), u_y(x, y)\}$ . The Hookian elastic free energy of the lamella depends on the symmetry of the point group that the underlying crystalline lattice possesses. For example, the orthorhombic symmetry of PE has nine independent elastic constants. For the sake of simplicity, we consider homogeneous and isotropic crystalline order, which has two independent elastic constants. The Hookian elastic free energy is given by

$$F_u = \frac{Y}{2(1+\nu)} \int \left( u_{ij}^2 + \frac{\nu}{1-\nu} u_{ii}^2 \right) dx dy \quad (5.1)$$

where  $Y$  and  $\nu$  are two-dimensional Young's modulus and Poisson's ratio, and  $\{i, j\} = \{1, 2\}$  such that  $x_1 = x$  and  $x_2 = y$ . Hereafter we follow Einstein's summation convention, i.e., repeated indices are summed over. The strain tensor, by definition, is

$$u_{ij} = \frac{1}{2} \left( \frac{\partial u_i}{\partial x_j} + \frac{\partial u_j}{\partial x_i} + \frac{\partial u_k}{\partial x_i} \frac{\partial u_k}{\partial x_j} \right) \quad (5.2)$$

Within the harmonic approximation, the linearised strain tensor is obtained by neglecting the third term in Eq. 5.2. For stability  $Y > 0$  and  $-1 < \nu < 1$  (two-dimensions).

### 5.3.2 Tilt order of the stems

Mathematically, tilt order  $\hat{\mathbf{s}}$  of the polymer stems is given by  $\hat{\mathbf{s}} = \hat{\mathbf{c}} - (\hat{\mathbf{c}} \cdot \hat{\mathbf{n}}) \hat{\mathbf{n}}$ , where  $\hat{\mathbf{c}}$  and  $\hat{\mathbf{n}}$  are the axis of the stem and lamellar normal, respectively. For a flat lamella with unit normal along  $z$ -axis, the projected stem field simplifies to  $\hat{\mathbf{s}} = \{s_x, s_y\}$  such that  $s_x^2 + s_y^2 = 1$ . The elastic free energy due to deformations in the stem field is given by

$$F_s = \int \left[ \frac{\tilde{K}_1}{2} (\boldsymbol{\partial} \cdot \hat{\mathbf{s}})^2 + \frac{\tilde{K}_2}{2} (\boldsymbol{\partial} \times \hat{\mathbf{s}})^2 \right] dx dy \quad (5.3)$$

where  $\tilde{K}_1$  and  $\tilde{K}_2$  are, respectively, the splay, and bend elastic constants and  $\partial = \{\partial_x, \partial_y\}$  is the flat gradient operator.

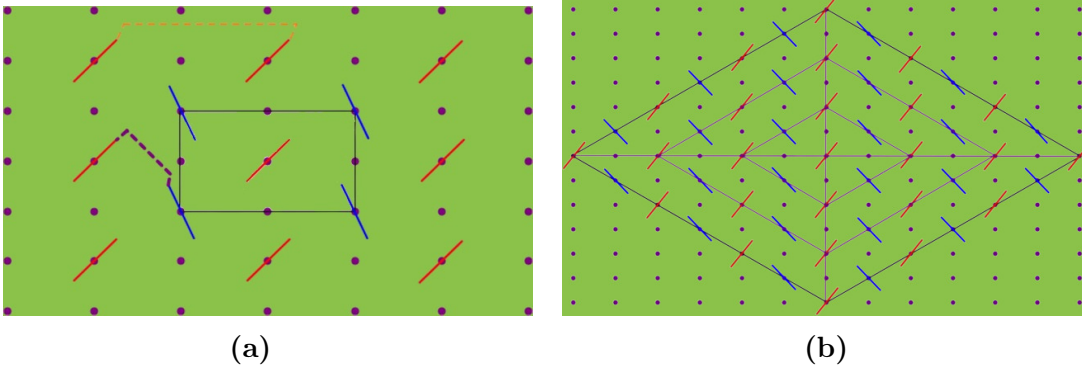


**Figure 5.6:** Surface of the PE lamella: (a) Viewed along the  $c$ -axis. The two dashed lines represent the two possible folds. Energetically the thick dashed fold is favourable. (b) Illustration of lozenge-shaped, sectored lamella. Images are taken from Ref. [5]

### 5.3.3 Fold field

We note that orientation of folds depends on the symmetry of underlying crystalline order of the polymer lamella. For PE there are two possible fold directions (See Fig. 5.6(a)). Folds along these two directions have different energy. Moreover, in the ground state configuration folds at the two fold surfaces are uniformly aligned. Thus, the ground state of a lamella has up-down symmetry. The fold direction is described by apolar vector field  $\hat{n}_f$  with  $-\hat{n}_f \equiv \hat{n}_f$  symmetry. For a flat lamella fold field is given by  $\hat{n}_f(x, y) = \{\cos \alpha(x, y), \sin \alpha(x, y)\}$ , where orientational field  $\alpha(x, y)$  is the angle made by  $\hat{n}_f$  with respect to  $x$ -axis. Because of up-down symmetry,  $\alpha$  is measured modulo  $\pi$ .

Unlike square, or perfect hexagonal shapes, the side lengths of each sector can, in general be different. Typically, sectors come in lozenge and hexagonal shapes depending on underlying crystalline order and growth conditions. A cartoon of lozenge shaped sector obtained by folds with the lowest free energy is shown in Fig. 5.6(b). In our model, we consider square-shaped sectors for the sake of simplicity. A square shape can be obtained if the two possible directions for the PE folds shown in Fig. 5.6 have the same energy. To do this, we choose a potential that stabilises square sectors. The macroscopic details of folds and shapes of the lamella are captured in the potential field. The potential that

stabilises the square sector is

$$V_\alpha(x, y) = \frac{h_4}{4} \int \cos [4\alpha(x, y)] dx dy \quad (5.4)$$

where  $h_4$  is strength of the potential.

This potential has four equal minima at  $\alpha = \pi/4, 3\pi/4, 5\pi/4$  and  $7\pi/4$  such that there are four equivalent ground states. Each ground state corresponds to a domain in the sector, and from one domain to another, the folds deform smoothly. In general, folds can deviate from the preferred direction causing deformations in the fold field. We use the standard, isotropic, two-dimensional nematic free energy to model the energetics of fold deformations. The corresponding free energy is given by

$$F_\alpha = \int \left( \frac{K_1}{2} (\boldsymbol{\partial} \cdot \hat{\mathbf{n}}_f(x, y))^2 + \frac{K_2}{2} (\boldsymbol{\partial} \times \hat{\mathbf{n}}_f(x, y))^2 \right) dx dy, \quad (5.5)$$

where  $K_1$  and  $K_2$  are, respectively, the splay, and bend elastic constants for fold field. In one constant approximation, the free energy reduces to

$$F_\alpha = \frac{K_\alpha}{2} \int |\boldsymbol{\partial}\alpha(x, y)|^2 dx dy \quad (5.6)$$

where  $K_\alpha$  is elastic constant.

It is important to note that there is a coupling between crystalline order ( $u_{ij}$ ) and fold field ( $\hat{\mathbf{n}}_f$ ) as shear deformations in crystalline order can change in fold orientation. Moreover, this coupling should be invariant under up-down symmetry (i.e.,  $-\hat{\mathbf{n}}_f \equiv \hat{\mathbf{n}}_f$ ). Keeping these considerations, the simplest coupling between  $u_{ij}$  and  $\hat{\mathbf{n}}_f$  is  $[u_{ij} - (1/2)\delta_{ij}u_{kk}]n_{f_i}n_{f_j}$  [63]. Note that this coupling is non-linear because it involves two  $\hat{\mathbf{n}}_f$  fields and one  $\mathbf{u}$  field.

To be consistent with the harmonic approximation, we consider de Gennes type coupling used in nematic elastomers [15]. We use this coupling in the context of crystalline and fold field ( $\alpha$ -field) of polymer crystals. Rotations in crystalline lattice are given by  $\Theta = (1/2)(\partial_x u_y - \partial_y u_x)$  [19]. It is a  $z$  component of  $(1/2)\nabla \times \mathbf{u}$ . For rigid rotations, changes in  $\alpha$  should match with  $\Theta$  i.e.,  $\delta\Theta = \delta\alpha$ . The elastic

free energy from non-uniform rotations in  $\Theta$  and  $\alpha$  field takes the form

$$F_{\Theta\alpha} = \frac{K_{\Theta\alpha}}{2} \int (\delta\Theta - \delta\alpha)^2 dx dy \quad (5.7)$$

where  $K_{\Theta\alpha}$  is a coupling constant. Note that  $F_{\Theta\alpha}$  is minimum for  $\delta\Theta = \delta\alpha$ . This coupling ensures  $\delta\Theta \approx \delta\alpha$  for the crystalline lamella. Therefore, disclinations in the fold field would induce disclinations in crystalline order and vice versa. It is important to note that the elastic free energy of an isolated disclination in a flat crystalline membrane diverges as the square of the system size [27]. In contrast, the elastic free energy of an isolated disclination in nematic order diverges logarithmically with the system size [2]. In what follows we ignore the coupling because of the prohibitively high elastic free energy cost for disclinations in crystalline order [5].

### 5.3.4 Surface- and line tension energies

In addition to elastic free energies and the potential energy, a polymer lamella in a solution or a melt has surface tension energy given by

$$F_{\sigma} = 2 \tilde{\sigma} \int dx dy \quad (5.8)$$

where  $\tilde{\sigma}$  is the surface tension. The factor 2 indicates contribution from the upper and lower surfaces of the lamella. For simplicity, we use the notation  $\sigma = 2 \tilde{\sigma}$  to represent total surface tension.

A sectored lamella is finite and has boundaries. Therefore, the isotropic line tension free energy is given by

$$E_{iso} = \gamma \oint dl \quad (5.9)$$

where  $\gamma$  is isotropic line tension, and  $dl$  is the length element on the boundary. The lamella is decorated with folds; it has orientational order, which gives an anisotropic contribution. The anisotropic line tension generally prefers a particular angle between the outward normal to the boundary and the field [62]. We model the anisotropic line tension as the symmetry- allowed Rapini-Papoular

form [62].

$$E_{an} = -\gamma_{an} \oint [\hat{\mathbf{n}}_f \cdot (\cos \alpha_0 \hat{\mathbf{n}}_b + \sin \alpha_0 \hat{\mathbf{t}}_b)]^2 dl \quad (5.10)$$

where  $\alpha_0$  is the preferred fold angle with boundary normal  $\hat{\mathbf{n}}_b$ ; and  $\hat{\mathbf{t}}_b$  is tangent to the boundary. To ensure  $-\hat{\mathbf{n}}_f \equiv \hat{\mathbf{n}}_f$  symmetry, the term inside integral is squared. For the square sector we choose  $\alpha_0 = \pi/2$ ; i.e. at the boundary, the fold field is aligned parallel to tangent  $\hat{\mathbf{t}}_b$ . With this choice, the anisotropic line tension is given by

$$\begin{aligned} E_{an} &= -\gamma_{an} \oint (\hat{\mathbf{n}}_f \cdot \hat{\mathbf{t}}_b)^2 dl \\ &= -\gamma_{an} \oint \cos^2(\alpha - \alpha_b) dl \\ &\equiv \gamma_{an} \oint \sin^2(\alpha - \alpha_b) dl \end{aligned} \quad (5.11)$$

where  $\alpha_b$  is the angle made by the tangent to the boundary with respect to  $x$ -axis. With this background, we discuss below the equilibrium equation that stabilises the square sector polymer lamella.

## 5.4 Equilibrium equation: An exact solution

Minimisation of total elastic free energy  $F_T$  (see below) with respect to  $\alpha$  gives equilibrium fold texture. The total free energy of the lamella, ignoring the coupling between  $\Theta$  and  $\alpha$ , is given by

$$F_T = F_u + F_s + F_\alpha + V_\alpha + F_\sigma. \quad (5.12)$$

The equilibrium equation corresponding to  $\alpha$ -field takes the form

$$\frac{\delta F_T}{\delta \alpha} = -K_\alpha \nabla_{xy}^2 \alpha - h_4 \sin(4\alpha) = 0 \quad (5.13)$$

where the two-dimensional Laplacian operator  $\nabla_{xy}^2 = \partial_x^2 + \partial_y^2$ . Note that the equation is a non-linear partial differentiation equation in  $\alpha$  because of the  $\sin(4\alpha)$  term. Such type of equations are known as sine-Gordon equations [3]. The one-dimensional solution to sine-Gordon equation gives a wall or soliton solution.

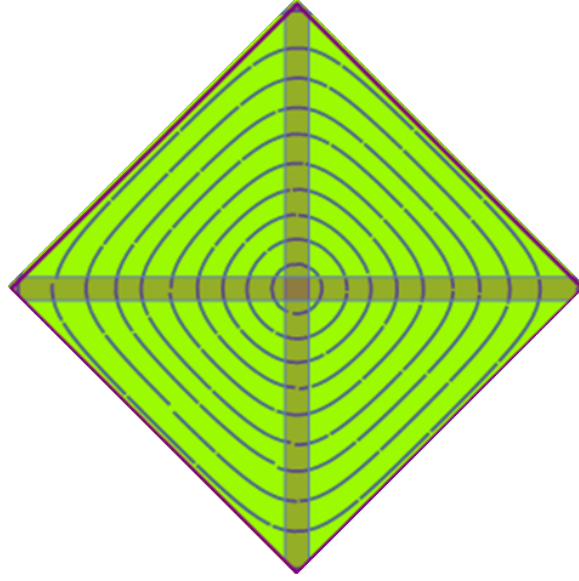


**Figure 5.7:** Square sector: Texture of fold field obtained from the exact solution  $\alpha_s(x, y)$ . Two shaded lines represent the soliton type walls of wall width  $w$ . The fold field follow stream lines of +1 disclination and the disclination core is located at the center of the square.

For the square sector, the exact solution to Eq. 5.13 is [5]

$$\alpha_s(x, y) = \arctan \left[ \frac{\tanh(y/w)}{\tanh(x/w)} \right] - \frac{\pi}{2}, \quad (5.14)$$

where the length scale  $w = \sqrt{K_\alpha/h_4}$ . Subtraction of  $\pi/2$  in the solution ensures that the boundary condition that fold field  $\hat{\mathbf{n}}_f$  is parallel to tangent to the boundary ( $\hat{\mathbf{t}}_b$ ). The streamlines of fold field in the square sector are depicted in Fig. 5.7. We note that the streamlines form a +1 disclination in fold field with two intersecting walls, of wall width  $w$  each, along  $x$ - and  $y$ - axes, the point of intersection being the core of the disclination.

Having obtained the exact solution for square sector, we investigate the stability analysis by comparing the free energetics of the square sector to the uniform fold configuration.

## 5.5 Energetics

We now discuss the energetics of a square sector and a square polymer lamella of uniform fold field (See Fig. 5.8(a)). Side length of both squares are set to be equal, say  $l$ , such that surface and isotropic line tensions for both configurations are the same. In calculating the total free energy, we assume that crystalline and tilt orders are identical in both sector- and uniform configurations. Therefore only the fold energetics plays important role in the stability analysis.

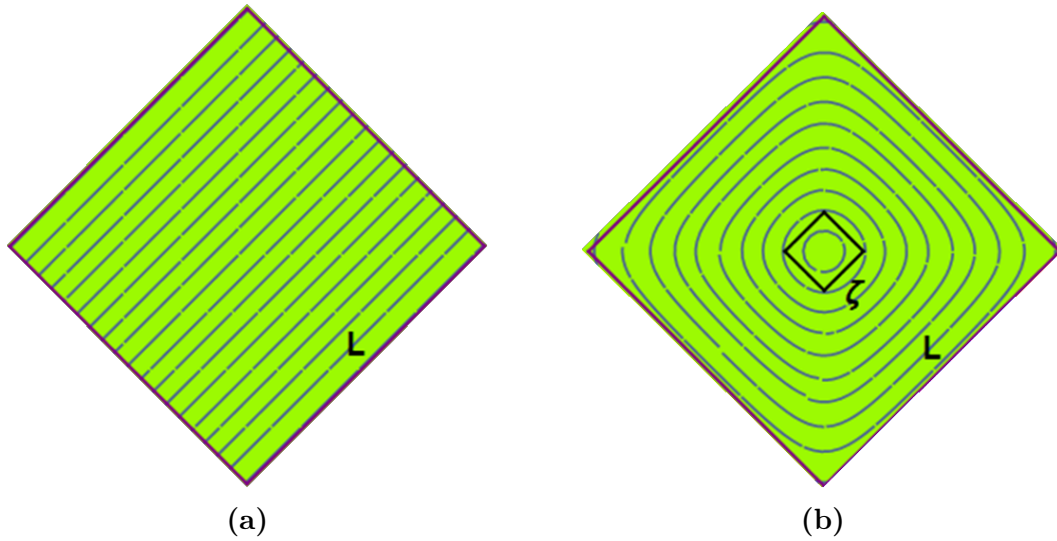


**Figure 5.8:** (a) Uniform fold field: Squared shaped lamella with side length (in  $w$  units)  $L$ . (b) Sector: Square shaped sector with side length (in  $w$ ) units  $L$ . Shape of the core is symmetrical to the sector and has side length (in  $w$ )  $\zeta$ .

### A square lamella with uniform fold field

We begin by considering an uniform fold field in square shaped lamella with side length  $l$  (See Fig. 5.8(a)). For this case  $\alpha = \pi/4$ , and satisfies the equilibrium equation 5.13. Since the fold field is uniform,  $F_\alpha = 0$ . Contribution from the potential is given by

$$V_\alpha^{(\text{Uni})} = -\frac{h_4}{4} l^2 \quad (5.15)$$

where the superscript (Uni) indicates the uniform configuration. The surface, isotropic and anisotropic tensions take the form

$$\begin{aligned} F_\sigma &= \sigma l^2, \\ E_{iso} &= 4 \gamma_{iso} l, \\ E_{an}^{(\text{Uni})} &= 2 \gamma_{an} l. \end{aligned} \tag{5.16}$$

We note that surface and line tensions are the same for the square sector of side length  $l$ , thus we omit the superscript (Uni). The factor 4 in  $E_{iso}$  is due to four sides of the boundary, and for  $E_{an}^{(\text{Uni})}$  only two sides of the boundary follow the boundary condition leaving out free energy cost for the remaining two sides.

For mathematical simplifications, we define dimensionless fold free energy  $\mathcal{E} = (F_\alpha + V_\alpha + E_{an})/K_\alpha$ . The dimensionless fold free energy for the uniform configuration is given by

$$\begin{aligned} \mathcal{E}^{(\text{Uni})} &= 2\Gamma L - \frac{L^2}{4} \\ &\equiv \mathcal{E}^{(\text{Uni})}(\Gamma, L) \end{aligned} \tag{5.17}$$

where, dimensionless side length  $L = l/w$  and parameter  $\Gamma = (\gamma_{an}w)/K_\alpha$ . Recall that wall width  $w = \sqrt{K_\alpha/h_4}$ .

## A square sectored lamella

In this section, we consider a square sectored lamella with side length  $l$  (same as for the uniform case) in  $x y$ -plane such that the walls coincide with the coordinate axes (See Fig. 5.7). We bear in mind that the fold field has a point disclination at the center i.e., the origin. Thus, we need to use cut offs for calculating  $F_\alpha$  and  $V_\alpha$  to avoid the singularities arising from the core of the disclination. Following the symmetry of the square shaped lamella, we choose a square shaped core with side length  $\xi$  (See Fig. 5.8(b)). Therefore the core area is  $\xi^2$ .

Upon substituting the exact solution for  $\alpha$  (Eq. 5.14) in  $F_\alpha$  with appropriate core gives the elastic free energy cost due to deformations in the fold field. However, the integrals are not analytically tractable. We use a numerical approach with the transformations  $x \rightarrow w x'$  and  $y \rightarrow w y'$  such that the integrals become dimensionless. The free energy due to deformations in fold field, in the units of  $K_\alpha$ , is then given by

$$\begin{aligned} \frac{F_\alpha^{(\text{Sec})}}{K_\alpha} = 4 \times \frac{1}{2} & \left[ \int_0^{\zeta/\sqrt{2}} dx' \int_{-x'+\zeta/\sqrt{2}}^{-x'+L/\sqrt{2}} dy' |\partial\alpha_s(x', y')|^2 \right. \\ & \left. + \int_{\zeta/\sqrt{2}}^{L/\sqrt{2}} dx' \int_0^{-x'+L/\sqrt{2}} dy' |\partial\alpha_s(x', y')|^2 \right] \end{aligned} \quad (5.18)$$

where the superscript (Sec) indicates the sector configuration, the dimensionless core size  $\zeta = \xi/w$ , and dimensionless side length  $L = l/w$ . The factor of 4 in the expression above covers the full area of the square. Following the same procedure, we obtain the potential energy (in  $K_\alpha$  units) takes the form

$$\begin{aligned} \frac{V_\alpha^{(\text{Sec})}}{K_\alpha} = 4 \times \frac{1}{4} & \left[ \int_0^{\zeta/\sqrt{2}} dx' \int_{-x'+\zeta/\sqrt{2}}^{-x'+L/\sqrt{2}} dy' \cos(4\alpha_s(x', y')) \right. \\ & \left. + \int_{\zeta/\sqrt{2}}^{L/\sqrt{2}} dx' \int_0^{-x'+L/\sqrt{2}} dy' \cos(4\alpha_s(x', y')) \right] \end{aligned} \quad (5.19)$$

The anisotropic line tension contribution, in  $K_\alpha$  units, is given by

$$\frac{E_{an}^{(\text{Sec})}}{K_\alpha} = 4 \Gamma \int_0^{L/\sqrt{2}} dx' \sin^2 \left[ \alpha_s(x', -x' + \frac{L}{\sqrt{2}}) - \frac{3\pi}{4} \right]. \quad (5.20)$$

We note that the factor 4 is for four sides of the boundary and that  $\alpha_b = 3\pi/4$  in the first quadrant. The total, dimensionless fold free energy of the square sector is given by

$$\begin{aligned} \mathcal{E}^{(\text{Sec})} &= \frac{F_\alpha^{(\text{Sec})}}{K_\alpha} + \frac{V_\alpha^{(\text{Sec})}}{K_\alpha} + \frac{E_{an}^{(\text{Sec})}}{K_\alpha} \\ &\equiv \mathcal{E}^{(\text{Sec})}(\zeta, \Gamma, L) \end{aligned} \quad (5.21)$$

With this background, we discuss the stability analysis in the next section.

## 5.6 Stability analysis: A phase diagram

To investigate the stability of the square sector, we compare its free energy to that of the uniform fold configuration. We consider  $\Delta\mathcal{E} = \mathcal{E}^{(\text{Uni})} - \mathcal{E}^{(\text{Sec})}$  which is a function of  $\zeta$ ,  $\Gamma$  and  $L$ . Note that  $\Delta\mathcal{E} > 0 \implies$  the sector configuration is energetically stable,  $\Delta\mathcal{E} < 0 \implies$  the uniform configuration is stable and  $\Delta\mathcal{E} = 0 \implies$  phase boundary that separates the two configurations. To implement

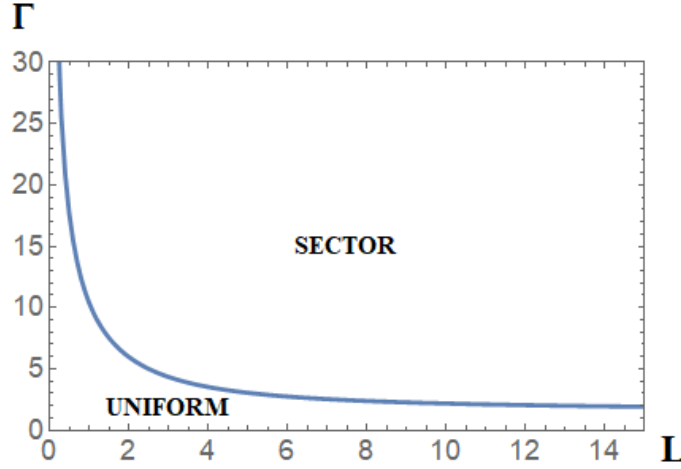


**Figure 5.9:** Phase diagram of sector and uniform configurations: The curve is a phase boundary between square sector and uniform configurations. Region below/ above the curve is the stability range for uniform/ sector configuration.

this procedure, we numerically calculate  $\Delta\mathcal{E}$  for fixed  $\zeta$ , and the given set of parameters  $\{\Gamma, L\}$ .

The typical core size is order of the thickness of the polymer lamella. In comparison to wall width  $w$ , the core size  $\xi \approx 0.01 w$ . Therefore we take dimensionless core size  $\zeta = 0.01$ , and numerically obtain a “phase diagram” that indicates the stability of the squared sector as a function of  $\{\Gamma, L\}$ . The plot is shown in the Fig. 5.9. We note that the square sector is stable for large  $\Gamma$  and  $L$ . The larger the  $\Gamma$  value, the stronger the anisotropic line tension that traps the disclination in the fold field. Hence the stability of sector configuration. For given  $\Gamma$ , there exists a critical length ( $L^*$ ) above which the sector configuration is stable.

## 5.7 Results and discussion

In this chapter we have discussed the model presented in Ref. [5] to study stability of the sector morphology and have improved the calculations for energetics, especially the core energetics. This calculation was not clear in Ref. [5]. With the modified calculations, the phase diagram plot of sector and uniform configurations is qualitatively similar to that of Ref. [5]. The results obtained in this chapter are important in studying the uniform, the sector, and the tent configurations (See

Chapter 6). We show that sectors are formed due to trapping of disclination in fold field by strong anisotropic line tension parameter  $\Gamma$  (dimensionless). We find that square sectors are stable for large  $\Gamma$  when compared to an identical square shaped uniform fold field configuration.

This model can be extended to study other morphologies such as rhombi, hexagonal sectors and tents. In the next chapter we address the stability of square shaped tent morphology.



## Chapter 6

# Tent morphology of polymer crystallites

### 6.1 Introduction

Single crystalline lamellae are observed to form hollow tent-like structures under certain growth conditions [64]. Atomic force microscopy (AFM) images of polyethylene single crystals grown from dilute xylene solution are given Fig. 6.1. In this chapter, we present a model to study the stability of tent(hollow pyramidal) morphology polymer crystalline. This model is an extension of the model of the sectored morphology discussed in the previous chapter. We note that the sectored morphology of polymer crystallites has a disclination at the centre. As discussed in Chapter 1, the disclination is capable of buckling the crystalline sector, with the disclination point at its apex. The buckling phenomenon in the presence of topological defects in crystalline membrane is discussed by Sueng and Nelson [27], and in hexatic membrane is explained by Deem and Nelson [2]. In addition to the central, point disclination, the sectored morphology also has soliton-type walls along the diagonals of the square. The crystalline membrane can also buckle along the walls [65]. Therefore we treat the tent configurations as buckled sector configurations(Fig. 6.2). Within the frame work of the model, we study the stability analysis of tent morphology in comparison with flat uniform and flat sectored morphology. Similar to the previous chapter, we obtain a “phase diagram” indicating the stability of flat uniform, flat-sectored, and tent configuration over the suitable parameters.

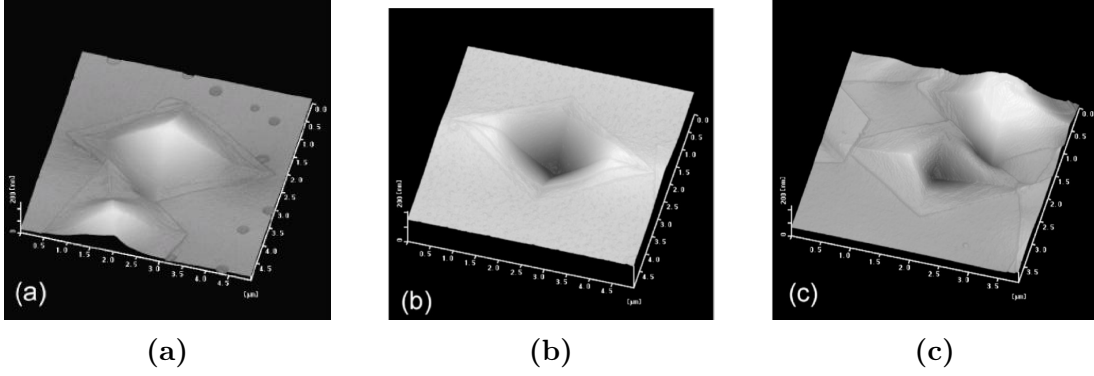


**Figure 6.1:** AFM images of solution-grown single crystals: (a) Convex hollow pyramidal type. (b) Concave hollow pyramidal type. (c) Chair type. (Image is taken from Toda group,2003 [64])

## 6.2 The model

We now consider the buckling of the flat sector morphology to study the stability of the tent morphology. We know that buckling involves bending of polymer crystalline lamellae. The free energy cost for bending of the polymer lamellae is given by the Helfrich term [28]

$$F_H = \frac{\kappa}{2} \int H^2 d\mathcal{A} \quad (6.1)$$

where  $\kappa$  is bending rigidity of the lamella and  $H$  is the mean curvature of the buckled surface with the area element  $d\mathcal{A}$ .

The free energy contributions from the Hookian elasticity ( $F_u$ ), the stem field ( $F_s$ ), the fold field ( $F_\alpha$ ) and the fold potential ( $V_\alpha$ ) are (See the previous chapter)

$$\begin{aligned} F_u &= \frac{Y}{2(1+\nu)} \int \left( u_{ij}^2 + \frac{\nu}{1-\nu} u_{ii}^2 \right) d\mathcal{A}, \\ F_s &= \int \left[ \frac{\tilde{K}_1}{2} (\nabla \cdot \hat{\mathbf{s}})^2 + \frac{\tilde{K}_2}{2} (\nabla \times \hat{\mathbf{s}})^2 \right] d\mathcal{A}, \\ F_\alpha &= \frac{1}{2} K_\alpha \int g^{\mu\nu} (\partial_\mu \alpha - A_\mu) (\partial_\nu \alpha - A_\nu) d\mathcal{A}, \\ V_\alpha &= \frac{h_4}{4} \int \cos(4\alpha) d\mathcal{A}, \end{aligned} \quad (6.2)$$

where  $A_\mu$  is the spin connection term for the buckled surface with metric tensor

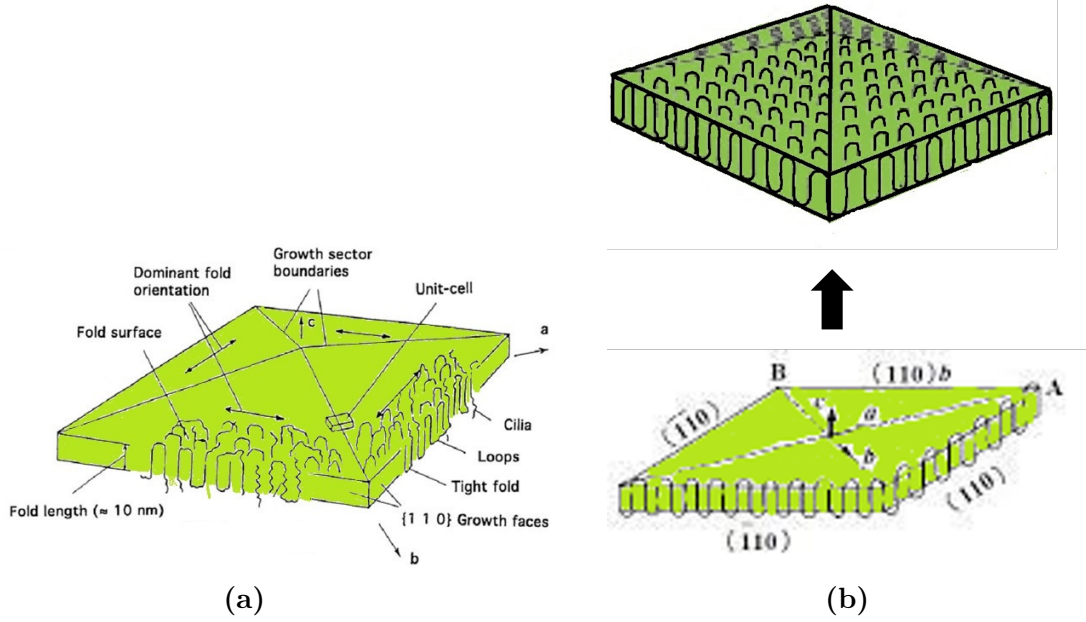


**Figure 6.2:** (a) Cartoon of tent configuration depicting essential features. (b) Illustration of buckling of a sector into tent configuration.

$g_{\mu\nu}$ . Here  $g^{\mu\nu}$  is the inverse of  $g_{\mu\nu}$  and  $\nabla$  is the covariant derivative. The elastic constants  $Y$ ,  $\nu$ ,  $\tilde{K}_1$ ,  $\tilde{K}_2$ ,  $K_\alpha$  and  $h_4$  retain the same definitions as those in the sector morphology. We note that the coupling between crystalline order and fold field is ignored for the considerations of energetics, as mentioned in the previous chapter.

In addition to these bulk free energy terms, there is an important coupling between polymer stems and curvature due to bending of polymer lamella. The bending of polymer crystalline lamella can be achieved in two possible mechanisms (See Fig. 6.3). In the first mechanism, splay-like bending, the polymer stems undergo splay deformation in order to bend the lamella; whereas in the second mechanism, slide-like bending, the polymer stems are rearranged to be along the vertical direction via sliding mechanism without having splay deformation. The coupling between polymer stem field ( $\hat{s}$ ) and curvature can be captured in McKintosh-Lubensky like term [66, 67]. The free energy term due to coupling between  $\hat{s}$  and curvature is given by

$$F_{sH} = C \int (\nabla \cdot \hat{s}) H dA \quad (6.3)$$

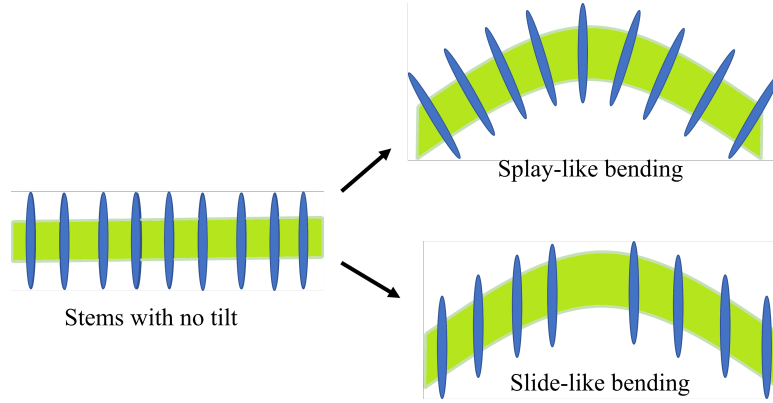


**Figure 6.3:** Schematics of bending of the polymer crystalline lamella. Two types of bending: (i) Splay-like bending in which polymer stems undergo splay deformation. (ii) Slide-like bending in which the stems point along the vertical direction via sliding mechanism.

where  $C$  is the coupling constant. We note that the transformation: normal ( $\hat{N}$ )  $\rightarrow -\hat{N}$  implies  $\hat{s} \rightarrow -\hat{s}$  and  $H \rightarrow -H$  such that the term  $(\nabla \cdot \hat{s}) H$  remains invariant (bi-layer symmetry).

The total bulk free energy ( $F$ ) of a buckled polymer crystalline lamella is

$$F = F_u + F_s + F_H + F_{sH} + F_\alpha + V_\alpha. \quad (6.4)$$

A finite sized surface has boundaries (edges) and corresponding line tension contributions to the free energy are given by

$$\begin{aligned} E_{iso} &= \gamma \oint dl, \\ E_{an} &= \gamma_{an} \oint \sin^2(\alpha - \alpha_b) dl, \end{aligned} \quad (6.5)$$

where  $\gamma$  and  $\gamma_{an}$  are isotropic and anisotropic line tensions respectively, and  $\alpha_b$  is the angle made by tangent to the boundary. In anisotropic line tension, we assume the boundary condition that the preferred fold configuration ( $\hat{n}_f$ ) is parallel to the tangent to the boundary (See the previous chapter for more details).

With this background we discuss the Euler-Lagrange equations of equilibrium for the buckled polymer lamellae.

### 6.3 Equilibrium equations

To obtain Euler-Lagrange equations of equilibrium, we minimise the total free energy ( $F$ ) with respect to stem field ( $\hat{\mathbf{s}}$ ) and fold field ( $\alpha$ ). The minimisation with respect to  $\hat{\mathbf{s}}$  gives

$$\frac{\delta F}{\delta \hat{\mathbf{s}}} = -\nabla \left( \tilde{K}_1 (\nabla \cdot \hat{\mathbf{s}}) + C H \right) - \tilde{K}_2 \nabla \times \nabla \times \hat{\mathbf{s}} = 0 \quad (6.6)$$

Above vector equation is complicated and difficult to solve in general. To simplify the problem, we consider the curl free stem configuration; that is  $\nabla \times \hat{\mathbf{s}} = 0$ . With this consideration Eq. 6.6 reduces to  $\tilde{K}_1 (\nabla \cdot \hat{\mathbf{s}}) + C H = \text{Constant}$ . Without loss of generality we take  $\text{Constant} = 0$ . Thus the simplified equilibrium equation takes the form

$$\nabla \cdot \hat{\mathbf{s}} = -\frac{C}{\tilde{K}_1} H. \quad (6.7)$$

To eliminate the explicit dependence of the stem field, we substitute the condition Eq. 6.7 in total free energy expression (Eq. 6.4). Upon substitution we get

$$F_s + F_{sH} + F_H = \frac{1}{2} \left( \kappa - \frac{C^2}{\tilde{K}_1} \right) \int H^2 d\mathcal{A}. \quad (6.8)$$

Thus modified total free energy ( $F$ ) is given by

$$F = F_u + F_\alpha + V_\alpha + \frac{1}{2} \kappa_{ef} \int H^2 d\mathcal{A}, \quad (6.9)$$

where the effective bending rigidity  $\kappa_{ef} = \kappa - (C^2/\tilde{K}_1)$ . We note that the effect of coupling between polymer stems and curvature reduces the bending rigidity.

The  $\alpha$ -equation corresponding to the equilibrium fold field on the surface is given by

$$\frac{\delta F}{\delta \alpha} = -K_\alpha \nabla \cdot (\partial \alpha - \mathbf{A}) - h_4 \sin(4\alpha) = 0 \quad (6.10)$$

where  $\nabla \cdot$  represents covariant divergence.

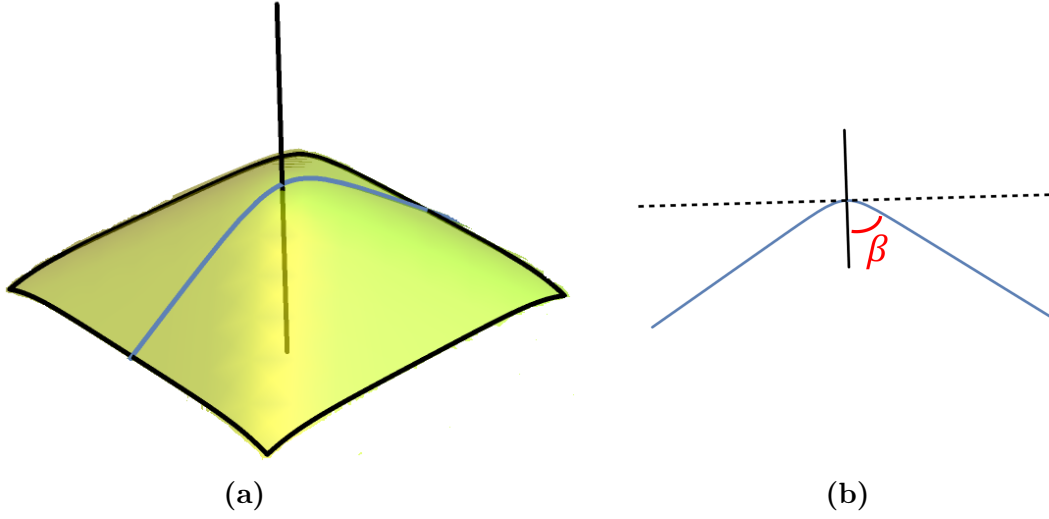


**Figure 6.4:** (a) A square pyramid (tent) surface: A plot of the height function  $h(x, y)$ . The black vertical and the blue lines represent axis and faces of the tent surface respectively. (b) Schematics of apex angle( $2\beta$ ): By definition, the angle between axis and face of the tent is  $\beta$ . The asymptotic slope of the tent face (blue line) is  $\tan(\pi/2 + \beta)$ .

## 6.4 Tent surface as an ansatz for shape equation

In order to discuss the equilibrium shape, we consider the parametrisation of the surface (Monge-representation) as  $\mathbf{R}(x, y) = \{x, y, h(x, y)\}$ , where  $h(x, y)$  is the height function. With this representation we get the metric  $g = 1 + (\nabla_{xy}h)^2$ , where  $(\nabla_{xy}h)^2 = (\partial_x h)^2 + (\partial_y h)^2$ . Within the Monge approximation, i.e.,  $(\partial_x h)^2, (\partial_y h)^2, (\nabla_{xy}h)^2 \ll 1$ , we get the spin connection

$$A_i = \frac{1}{2} \epsilon_{jk} \partial_k [(\partial_i h)(\partial_j h)] \quad (6.11)$$

where  $\{i, j, k\} = \{x, y\}$  and anti-symmetric tensor  $\epsilon_{xx} = \epsilon_{yy} = 0$ . The mean curvature simplifies to

$$H = \frac{1}{2} \nabla_{xy}^2 h \quad (6.12)$$

where the flat Laplacian  $\nabla_{xy}^2 h = \partial_x^2 h + \partial_y^2 h$ .

The general procedure for obtaining the equilibrium shape is to minimise the free energy ( $F$ ) with respect to  $h$ . However, the shape equation will be non-linear and highly difficult to solve. Therefore to simplify the problem, we surmise the height function, based on symmetries of the flat squared sector, as that of square

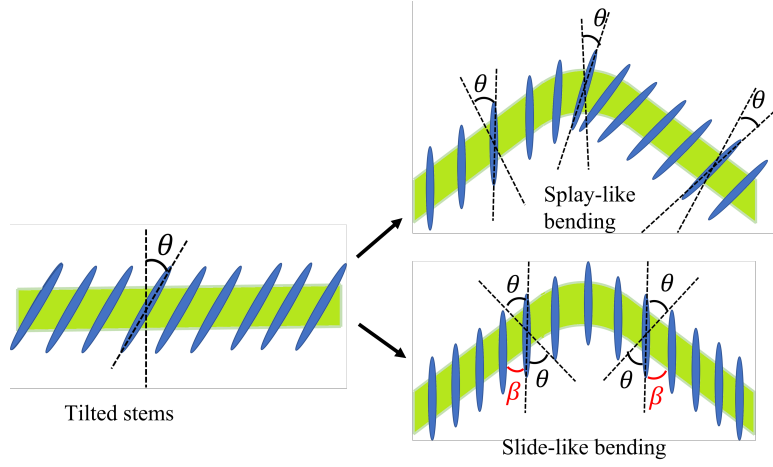


**Figure 6.5:** Cartoon of buckling of polymer lamella with tilted stem into tent configuration.

pyramid (tent configuration). The corresponding height function is given by (See Fig. 6.4(a))

$$h(x, y) = -a \log \left( \cosh \left[ \frac{x}{w} \right] \cosh \left[ \frac{y}{w} \right] \right) \quad (6.13)$$

where parameter  $a$  is “slope” of the tent and the wall width of the flat sector  $w = \sqrt{(K_\alpha/h_4)}$ . We note that the projection of edges of the tent are along the  $x$ - and  $y$ - axes respectively; and each quadrant represents the projected plane of the tent face. The asymptotic slope of tent face is  $\lim_{x \rightarrow \infty} dh(x, x)/dx = -2a/w$ . If the apex angle of the square pyramid (tent) is  $2\beta$ , the slope is given by (See Fig. 6.4(b))

$$-\frac{2a}{w} = \tan\left(\frac{\pi}{2} + \beta\right). \quad (6.14)$$

As we mentioned, the buckling of flat sector into tent configuration involves the rearrangement of polymer stems. The illustration of polymer stems in tent configuration is shown in Fig. 6.5. We believe that sliding-like bending of polymer lamella is favourable. From the geometrical arguments, we can relate the tilt angle ( $\theta$ ) of stem and apex angle ( $2\beta$ ) of the tent as follows (See Fig. 6.5)

$$\theta + \beta = \frac{\pi}{2}. \quad (6.15)$$

Upon substituting it in the slope formula (Eq. 6.14), we get a relation between the parameter  $a$  and the tilt angle as follows

$$A_w = \frac{a}{w} = \frac{1}{2} \tan(\theta). \quad (6.16)$$

This condition follows that the tilt angle of polymer stem determines the slope of tent surface.

For the equilibrium fold configuration on the tent surface  $h(x, y)$ , we need to solve the Eq. 6.10 with Monge approximation, i.e.,  $-K_\alpha(\nabla_{xy}^2 \alpha - \nabla_{xy} \cdot \mathbf{A}) - h_4 \sin(4\alpha) = 0$ . The equation is non-linear in  $\alpha$  because of the term  $\sin(4\alpha)$ . We note the term  $\nabla_{xy} \cdot \mathbf{A}$  is non-linear in the height field ( $h$ ) and difficult to solve the equation analytically. Within the linear regime of the height field, we neglect the  $\nabla_{xy} \cdot \mathbf{A}$  term. To make the analysis analytically tractable we make use of the exact solution of fold field for the flat sector,  $\alpha_s$  (Eq. 5.7). As  $\alpha_s$  satisfies the equation  $-K_\alpha \nabla_{xy}^2 \alpha_s - h_4 \sin(4\alpha_s) = 0$ , we ignore the contributions coming from spin connection. This assumption is valid for  $a \ll w$ . Thus we restrict ourselves to the tent surfaces that are almost flat. The cartoon of  $\alpha_s$  on tent surface is shown in Fig. 6.6(a). We note that the disclination core coincides with the tent apex, each tent face has uniform fold field and the adjacent face is connected by soliton type wall in fold field.

Having obtained analytical expressions for the height function and the fold field for tent configuration, we discuss the energetics below.

## 6.5 Energetics

We consider a finite sized square pyramid (tent) with base length  $l_T$ . Therefore, the boundary of the tent is a square with side length  $l_T$ . The expression for fold field  $\alpha$  on the tent surface is given by

$$\alpha_s(x, y) = \arctan \left[ \frac{\tanh(y/w)}{\tanh(x/w)} \right] - \frac{\pi}{2}. \quad (6.17)$$

We note that  $\alpha_s$  has a disclination at the center. Thus, we use cut offs for calculating  $F_\alpha$  and  $V_\alpha$  to avoid the singularities arising from the disclination.

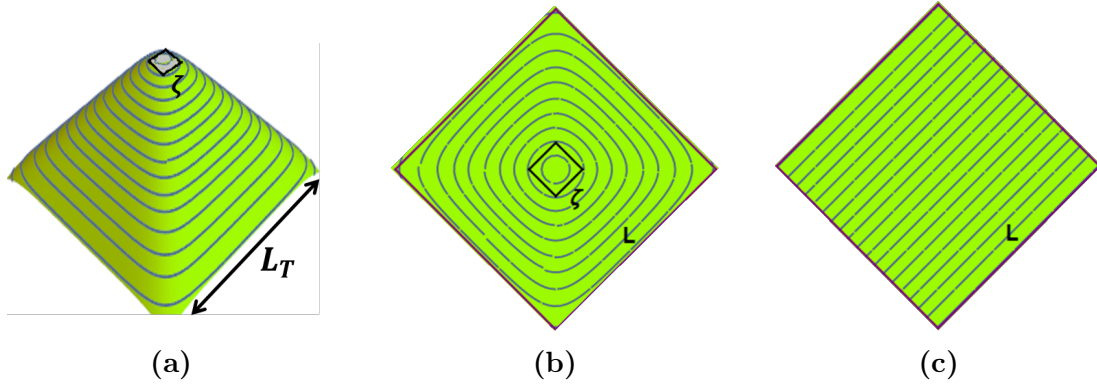


**Figure 6.6:** Schematics of the fold field: (a) On the tent surface (an exaggerated height field). Note the tent edges match with soliton-type walls in the fold field. The base length of the tent, in  $w$  units, is  $L_T$ . The black colored square represents the core with side length  $\zeta$  (in  $w$  units). (b) For flat sector of side length  $L$  (in  $w$  units). (c) For flat uniform configuration.

Following the symmetry of the square sector, we choose a square shaped core with side length  $\xi$  (See Fig. 6.6(a)).

As the integrals in free energy calculations are analytically not solvable, we use numerical approach with the transformations  $x \rightarrow w x'$  and  $y \rightarrow w y'$  such that the integral becomes dimensionless. The free energy due to deformations in fold field, in the units of  $K_\alpha$ , is given by

$$\begin{aligned} \frac{F_\alpha^{(\text{Tent})}}{K_\alpha} = & 4 \times \frac{1}{2} \left[ \int_0^{\zeta/\sqrt{2}} dx' \int_{-x'+\zeta/\sqrt{2}}^{-x'+L_T/\sqrt{2}} \sqrt{g} dy' |\partial\alpha_s(x', y')|^2 \right. \\ & \left. + \int_{\zeta/\sqrt{2}}^{L_T/\sqrt{2}} dx' \int_0^{-x'+L_T/\sqrt{2}} \sqrt{g} dy' |\partial\alpha_s(x', y')|^2 \right] \end{aligned}$$

where dimensionless length  $L_T = l_T/w$ , dimensionless core size  $\zeta = \xi/w$ , the metric  $g = 1 + (\nabla h)^2 = 1 + A_w^2(\tanh(x')^2 + \tanh(y')^2)$ . In this calculations, we ignore the coupling between curvature and fold field. The potential and bending

free energy are given by

$$\begin{aligned} \frac{V_\alpha^{(\text{Tent})}}{K_\alpha} &= 4 \times \frac{1}{4} \left[ \int_0^{\zeta/\sqrt{2}} dx' \int_{-x'+\zeta/\sqrt{2}}^{-x'+L_T/\sqrt{2}} \sqrt{g} dy' \cos(4\alpha_s(x', y')) \right. \\ &\quad \left. + \int_{\zeta/\sqrt{2}}^{L_T/\sqrt{2}} dx' \int_0^{-x'+L_T/\sqrt{2}} \sqrt{g} dy' \cos(4\alpha_s(x', y')) \right] \\ \frac{F_H}{K_\alpha} &= \frac{\kappa_d}{2} \times 4 \int_0^{L_T/\sqrt{2}} dx' \int_0^{-x'+L_T/\sqrt{2}} \nabla_{xy}^2 h \sqrt{g} dy', \end{aligned}$$

where dimensionless bending rigidity  $\kappa_d = \kappa_{ef}/(4K_\alpha)$  and mean curvature  $\nabla_{xy}^2 h = -A_w(\text{sech}^2(x') + \text{sech}^2(y'))$ .

The line tension contributions are as follows

$$\begin{aligned} \frac{E_{iso}^{(\text{Tent})}}{K_\alpha} &= 4 \Gamma_{iso} \int_0^{L_T/\sqrt{2}} dx', \\ \frac{E_{an}^{(\text{Tent})}}{K_\alpha} &= 4 \Gamma \int_0^{L_T/\sqrt{2}} dx' \sin^2 \left[ \alpha_s \left( x', -x' + \frac{L_T}{\sqrt{2}} \right) - \frac{3\pi}{4} \right] \end{aligned}$$

where the dimensionless line tension parameters  $\Gamma_{iso} = (w \gamma_{iso})/K_\alpha$  and  $\Gamma = (w \gamma_{an})/K_\alpha$ . The total free energy of the tent configuration in the  $K_\alpha$  is given by

$$\begin{aligned} \mathcal{E}_T^{(\text{Tent})} &= \frac{F_\alpha + V_\alpha + F_H + E_{an} + E_{iso}}{K_\alpha} \\ &\equiv \mathcal{E}_T^{(\text{Tent})}(\zeta, A_w, L_T, \Gamma_{iso}, \Gamma, \kappa_d). \end{aligned} \tag{6.18}$$

## 6.6 Phase diagram of tent, sector and uniform configurations

In order to study the stability analysis, we compare the total free energies of flat uniform, flat sector and tent configurations. We choose the surface areas of all three configurations such that surface tension effects do not play major role in stability. Let the side length of the flat sector (and uniform configuration) is  $l$ . The surface area of tent  $\mathcal{A}_{tent} = \int \int d\mathcal{A}$ . Upon equating areas of flat sector and

tent surface, we get relation between  $l$  and  $l_T$  as

$$\begin{aligned} L &= \sqrt{\mathcal{A}_{tent}} \\ L(A_w, L_T) \end{aligned} \quad (6.19)$$

where  $L = l/w$ .

Using this condition, we follow the procedure described in the previous chapter to obtain the total free energies of flat uniform and flat sector configurations. To make calculations simpler, we use the core size in flat sector to be same as tent's case. The total free energy (in  $K_\alpha$ ) of flat uniform and flat sector morphology are given below

$$\begin{aligned} \mathcal{E}_T^{(\text{Uni})} &= \frac{F_\alpha + V_\alpha + E_{an} + E_{iso}}{K_\alpha} \\ &\equiv \mathcal{E}_T^{(\text{Uni})}(\Gamma_{iso}, \Gamma, L(A_w, L_T)) \\ \mathcal{E}_T^{(\text{Sec})} &= \frac{F_\alpha + V_\alpha + E_{an} + E_{iso}}{K_\alpha} \\ &\equiv \mathcal{E}_T^{(\text{Sec})}(\zeta, L(A_w, L_T), \Gamma_{iso}, \Gamma) \end{aligned} \quad (6.20)$$

The procedure for obtaining the phase diagram is as follows. We numerically calculate  $\mathcal{E}_T^{(\text{Uni})}$ ,  $\mathcal{E}_T^{(\text{Sec})}$  and  $\mathcal{E}_T^{(\text{Tent})}$  for given core size  $\zeta$ ,  $A_w$  for varying values of  $\kappa_d$ ,  $L_T$ ,  $\Gamma_{iso}$  and  $\Gamma$ . For fixed  $\zeta$ , we find a minimum of  $\mathcal{E}_T^{(\text{Uni})}$ ,  $\mathcal{E}_T^{(\text{Sec})}$  and  $\mathcal{E}_T^{(\text{Tent})}$  such that the lowest energy configuration is chosen. As a concrete example, we consider polyethylene(PE) crystalline. The tilt angle for PE is  $\theta \simeq \pi/6$ , thus,  $A_w \simeq (1/2) \tan(\pi/6) = 1/(2\sqrt{3})$ . For better representation we plot the phase diagram as function of  $\Gamma_{iso}$  and  $L_T$  for various  $\kappa_d$  and  $\Gamma$ . The plots are given in Fig. 6.7 for  $\zeta = 0.01$  (same core size as the sector).

From the phase diagram (Fig. 6.7), it is clear that the tent configuration is stable for small bending rigidity ( $\kappa_d$ ), large line tension ( $\Gamma_{iso}, \Gamma$ ) values and sizes ( $L_T$ ). The sector configuration is favorable for large  $\kappa_d$  and  $L_T$ , and moderate values of  $\{\Gamma_{iso}, \Gamma\}$ . The results can be understood easily as the line tension parameters increase, trapping of disclination in the fold field becomes stronger which stabilises the sector formation. The lower bending rigidity is favorable for the sector polymer to buckle into tent configuration. We note that, depending on the parameter values, the tent configuration can be obtained directly from the

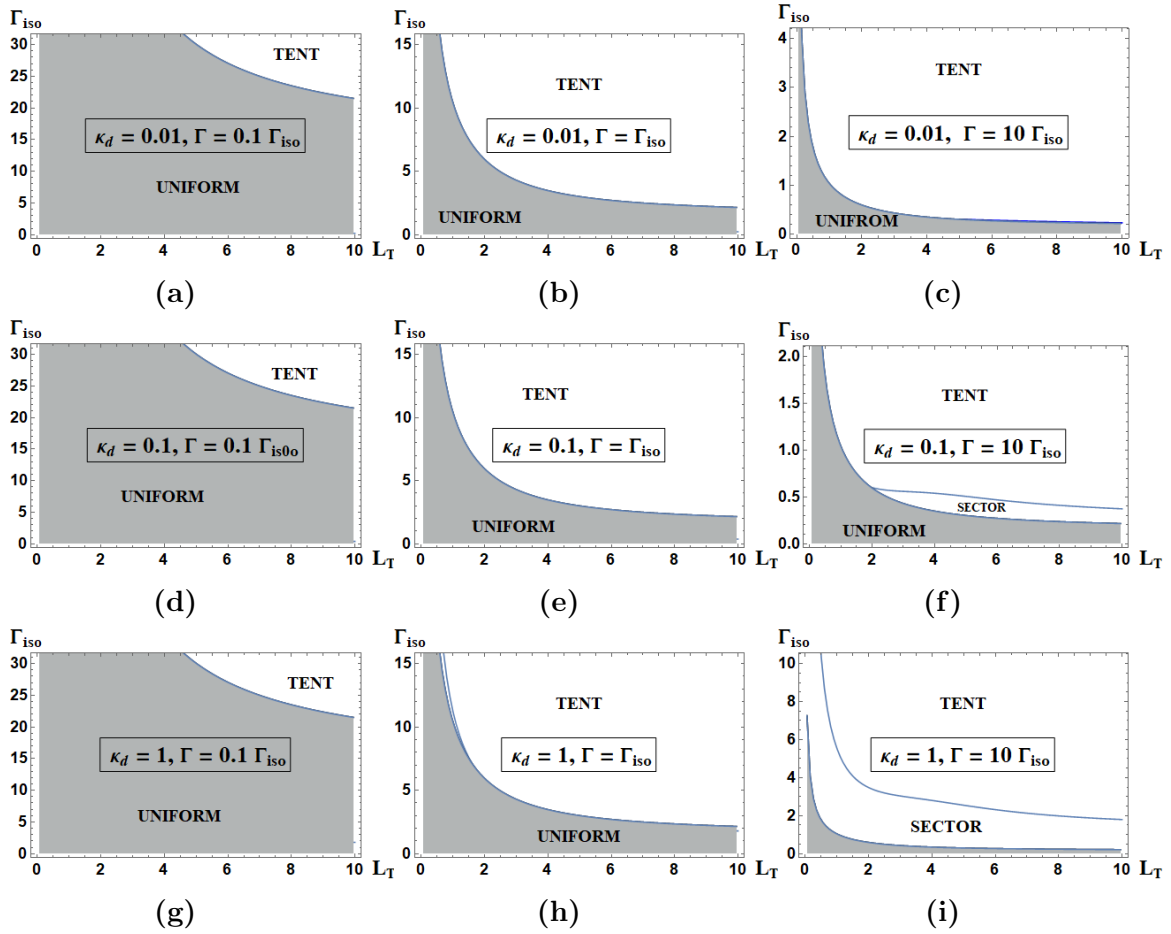


**Figure 6.7:** The phase diagram: Plots indicating stability range of the tent, the flat sector and the flat uniform.

flat uniform configuration without forming sector configuration (See Fig. 6.7(c), Fig. 6.7(g)). However, the sector configuration is stabilised for a different set of parameters and becomes an intermediate configuration in the transition from flat uniform to tent configuration(See Fig. 6.7(f), Fig. 6.7(i)).

## 6.7 Results and discussion

In this chapter we have discussed the simple model to study the stability of tent morphology. The model uses concepts from liquid crystal physics and topological defects. The central scheme of this model is that the sectors are formed due to trapping of a disclination in the fold field and the tent configurations are

---

buckled sectors. Stronger anisotropic line tension in the fold field traps a disclination more easily, and lower bending rigidity prefers the buckling of the lamellae. Within the frame work of the model, we find the solution to the tent surface with the prediction of the “slope formula” (6.14). We have shown that bending of a lamellae involves coupling between the tilt of the polymer stems and curvature of the lamellae that effectively reduces the bending rigidity. We also numerically calculated the phase diagram for polyethylene crystal that shows the stability of the tent, flat sector and flat uniform configurations. These results can be tested experimentally.

Our work can be extended to study other morphologies such as scrolls. The scroll configuration is a rolled lamella sheet in cylindrical shape. The formation of scrolls is fascinating and the study of their stability is one of our future directions for research.



## Appendix A

# Isothermal coordinates

### A.1 Isothermal coordinates

A mapping is said to be isothermal if a portion of a surface is mapped onto a portion of plane. Let  $\{x(u, v), y(u, v)\}$  be the isothermal coordinates on a surface  $\mathbf{R}(u, v)$  where  $\{u, v\}$  are the internal coordinates. By definition, the metric ( $ds$ ) on the surface with isothermal coordinates is given by

$$ds^2 = w(x, y) [dx^2 + dy^2], \quad w(x, y) > 0 \quad (\text{A.1})$$

where, the weight function  $w(x, y)$  is metric of the surface. In this new coordinate system, the Gaussian curvature ( $K$ ) of the surface reads as ( *Liouville's equation*)

$$K = -\frac{1}{2w(x, y)} \nabla_{xy}^2 \log w(x, y) \quad (\text{A.2})$$

where, Laplacian operator  $\nabla_{xy}^2 = \partial_x^2 + \partial_y^2$ .

The isothermal coordinates are locally Euclidean and conformal, i.e., angle preserving mapping. Thus, any vector field  $\hat{\mathbf{m}}(u, v)$  in the tangent plane of the surface is uniquely mapped on to the  $xy$ -plane. The corresponding field ( $\hat{\mathbf{m}}'(x, y)$ ) is given by

$$\hat{\mathbf{m}}'(x, y) = \cos \alpha'(x, y) \hat{\mathbf{x}} + \sin \alpha'(x, y) \hat{\mathbf{y}} \quad (\text{A.3})$$

where the angle  $\alpha'(x, y)$ -field with  $N$  disclinations of index  $q_k$  each placed at  $(x^k, y^k)$  is defined as,

$$\begin{aligned}\alpha'(x, y) &= \sum_k^N q_k \operatorname{Im}[\log(x + iy - x^k - iy^k)] + \text{const.} \\ &= \sum_k^N q_k \arctan\left(\frac{y - y^k}{x - x^k}\right) + \text{const.}\end{aligned}\tag{A.4}$$

The  $\alpha'$  is solution to the Laplace equation, i.e.,

$$\nabla_{xy}^2 \alpha'(x, y) = 0\tag{A.5}$$

Above equation is planar  $\alpha$ -equation (Eq. 1.13) mentioned in the previous chapter. With this background we recall the isothermal coordinates for known surfaces such as sphere, catenoid and helicoid.

### A.1.1 Stereographic Projection of a sphere

Stereographic projection is the standard method of generating isothermal coordinates for a sphere. The parametrization of the sphere with radius  $a$  is given by  $\mathbf{R}(\theta, \phi) = \{a \cos \phi \sin \theta, a \sin \phi \sin \theta, a \cos \theta\}$ ,  $0 \leq \theta < \pi$  and  $0 \leq \phi < 2\pi$ . The metric  $ds^2 = a^2 d\theta^2 + a^2 \sin^2 \theta d\phi^2$ , and the Gaussian curvature  $K = 1/a^2$ .

Let us consider a unit tangent vector field  $\hat{\mathbf{m}}(\theta, \phi) = \cos \alpha(\theta, \phi) \hat{\mathbf{e}}_\theta + \sin \alpha(\theta, \phi) \hat{\mathbf{e}}_\phi$ . The Poincaré-Hopf index theorem suggests that  $\hat{\mathbf{m}}$  must have topological defect(s) of total index “+2”. One of the configuration with two “+1” defects at poles is obtained by  $\alpha(\theta, \phi) = 0$  (See, Fig. 2.1(b)). We now discuss the stereographic projection approach to get more general  $\hat{\mathbf{m}}$  field.

A point  $P(\theta, \phi)$  on the sphere is mapped to some point on the plane  $Q = \{x, y, a\}$  such that south pole ( $S$ ), ( $P$ ) and ( $Q$ ) are collinear. Note that, in this projection, north pole ( $N$ ) maps to  $\{0, 0, a\}$  and south pole ( $S$ ) maps to infinity. Mathematically, the mapping and inverse mapping are given by

$$\begin{aligned}\{x, y\} &= \left\{2a \tan\left(\frac{\theta}{2}\right) \cos \phi, 2a \tan\left(\frac{\theta}{2}\right) \sin \phi\right\} \\ \{\theta, \phi\} &= \left\{2 \arctan\left(\frac{\sqrt{x^2 + y^2}}{2a}\right), \arctan\left(\frac{y}{x}\right)\right\}\end{aligned}\tag{A.6}$$

In terms of  $\{x, y\}$  coordinates, the parametrisation and metric of the sphere take the form

$$\begin{aligned} \mathbf{R}(x, y) &= \left\{ \frac{4a^2x}{x^2 + y^2 + 4a^2}, \frac{4a^2y}{x^2 + y^2 + 4a^2}, -a \frac{x^2 + y^2 - 4a^2}{x^2 + y^2 + 4a^2} \right\} \\ ds^2 &= \frac{16a^4}{(x^2 + y^2 + 4a^2)^2} (dx^2 + dy^2) \end{aligned} \quad (\text{A.7})$$

Here the weight function  $w(x, y) = \frac{16a^4}{(x^2 + y^2 + 4a^2)^2}$  is positive and, from the Eq. A.2 we get  $K = 1/a^2$ .

We now use the Eq. A.4 to generate defects configurations such as “+2” disclinations at north pole, two “+1” disclinations on the equator and, at south and north poles. For example,  $\alpha'$  field for “+2” disclination at north pole ( $\{\theta = 0\}$ , or  $\{x = y = 0\}$ ) and for two antipodal “+1” disclinations on the equator ( $\{\theta = \pi/2; \phi = \pi/2, 3\pi/2\}$  or  $\{x = 0; y = \pm 2\}$ ) are

$$\begin{aligned} \alpha'(x, y) &= 2 \arctan\left(\frac{y}{x}\right) \\ \alpha'(x, y) &= \arctan\left(\frac{y-2}{x}\right) + \arctan\left(\frac{y+2}{x}\right) \end{aligned} \quad (\text{A.8})$$

Notice that entire  $xy$ -plane is required to represent the full sphere. We overcome this difficulty by mapping upper hemisphere with Eq. A.6, Eq. A.7 and lower hemisphere with stereographic projection-II( in this convention,  $\{x, y, -R\}$  is the projected plane and the north pole is mapped to infinity).

Using the Eq. A.6, we map the  $\alpha'$  to  $\alpha$  field measured in  $\{\hat{\mathbf{e}}_\theta, \hat{\mathbf{e}}_\phi\}$  basis. The relation goes as follows

$$\alpha(\theta, \phi) = \alpha' - \phi \quad (\text{A.9})$$

We recall that  $\hat{\mathbf{e}}_\theta, \hat{\mathbf{e}}_\phi$  are singular at poles and the effect is manifested in  $\hat{\mathbf{m}}(\theta, \phi)$ . Even though  $\hat{\mathbf{m}}$  has defect(s) of total index “+2” away from the poles, deceivingly, there are defects of index zero at north and south poles This artefact is avoided by choosing stereographic projection which depicts true textures on sphere.

## A.2 Green's function for sphere

The Green's function  $G(\theta, \phi; \theta', \phi')$  for a spherical surface of radius  $a$  satisfies the equation

$$\nabla_{\theta, \phi}^2 G(\theta, \phi; \theta', \phi') = \frac{\delta(\theta - \theta') \delta(\phi - \phi')}{\sqrt{g}} - \frac{1}{4\pi a^2} \quad (\text{A.10})$$

Note that above equation is different from 2.7 with an additional term  $1/(4\pi a^2)$ . This is because the surface area of a sphere is finite ( $4\pi a^2$ ). The solution to the equation A.10 is [29]

$$G(\theta, \phi; \theta', \phi') = \frac{1}{4\pi} \log \left[ \frac{1 - C_\beta(\theta, \phi; \theta', \phi')}{2} \right], \quad (\text{A.11})$$

where

$$C_\beta(\theta, \phi; \theta', \phi') = \cos \theta \cos \theta' + \sin \theta \sin \theta' \cos(\phi - \phi'). \quad (\text{A.12})$$

For the azimuthal symmetry (no  $\phi$ -dependence), the Green's function satisfies the Laplace equation

$$\sin \theta \partial_\theta^2 G(\theta; \theta') + \cos \theta \partial_\theta G(\theta; \theta') + \frac{\sin \theta}{4\pi} = \frac{\delta(\theta, \theta')}{2\pi}, \quad (\text{A.13})$$

with the conditions  $G(\theta; \theta') = G(\theta'; \theta)$ , and  $G(\pi - \theta; \pi - \theta') = G(\theta; \theta')$ . The solution of the above equation is

$$G(\theta; \theta') = \frac{1}{8\pi} [\log(\sin \theta \sin \theta') + (\Theta(\theta' - \theta) - \Theta(\theta - \theta')) \log(\cot \frac{\theta}{2} \tan \frac{\theta'}{2})], \quad (\text{A.14})$$

## A.3 Magnitude of order parameter

As we mentioned, all the calculations of energetic of point and wall disclinations are based on the approximation that magnitude of order parameter is zero in the core, and non zero away from the core. There is step like discontinuity across the core. In this section, we study the magnitude of order parameter for the equatorial wall disclination. Given the  $\alpha$ -field for the equatorial wall(2.19), we numerically solve the Eq.2.4 with the boundary conditions  $\rho \rightarrow 0$  at the core ( $\theta = \pi/2$ ) and  $\rho \rightarrow 1$  far away from the core (say,  $\theta = 0, \pi$ ). Note that the solution depends on the dimensionless parameter  $\xi/a$ . Recall that  $\xi$  is the correlation length. The

plot of the solutions for different  $\xi/a$  values are given in Fig. A.1

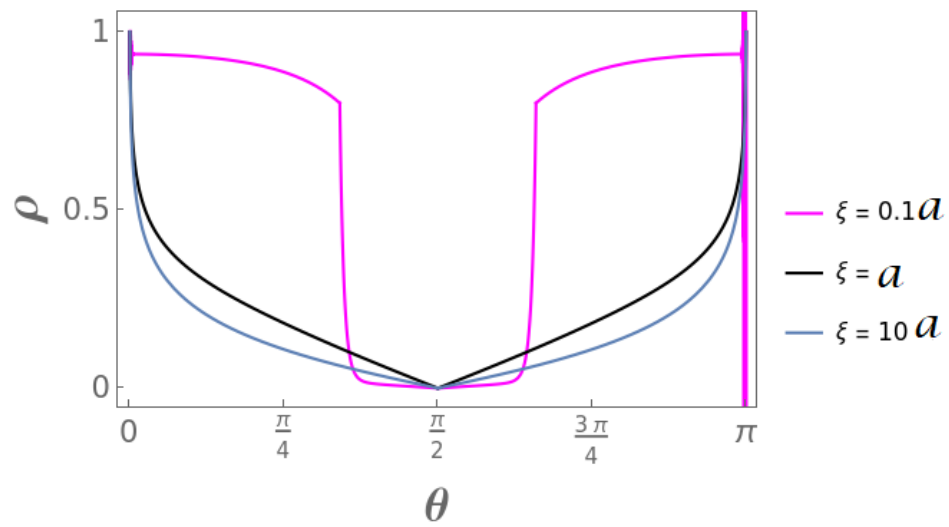


**Figure A.1:** Magnitude of order parameter around equatorial wall disclination:



## Appendix B

# Catenoid and helicoid isometry

### B.1 Isothermal coordinates on catenoid and helicoid

Parametrisation of catenoid is  $\mathbf{R}(\phi, z) = \{a \cosh(z/a) \cos \phi, a \cosh(z/a) \sin \phi, z\}$ , where  $-\infty < z < \infty$  and  $0 \leq \phi < 2\pi$ . The metric on catenoid takes the form

$$ds^2 = \cosh^2(z/a)(a^2 d\phi^2 + dz^2) \quad (\text{B.1})$$

Isothermal coordinates  $(x, y)$  on the catenoid are

$$\begin{aligned} \{x, y\} &= \left\{ a \exp\left(\frac{z}{a}\right) \cos \phi, a \exp\left(\frac{z}{a}\right) \sin \phi \right\} \\ \{z, \phi\} &= \left\{ \frac{a}{2} \log\left(\frac{x^2 + y^2}{a^2}\right), \arctan\left(\frac{y}{x}\right) \right\} \end{aligned} \quad (\text{B.2})$$

In terms of  $\{x, y\}$  coordinates, the parametrisation and metric of catenoid are

$$\begin{aligned} \mathbf{R}(x, y) &= \left\{ \frac{x(a^2 + x^2 + y^2)}{2(x^2 + y^2)}, \frac{y(a^2 + x^2 + y^2)}{2(x^2 + y^2)}, \frac{a}{2} \log\left[\frac{x^2 + y^2}{a^2}\right] \right\} \\ ds^2 &= \frac{(a^2 + x^2 + y^2)^2}{4(x^2 + y^2)^2} (dx^2 + dy^2) \end{aligned} \quad (\text{B.3})$$

We now use the Eq. A.4 to generate defects configurations. For example, the  $\alpha'$ -field for two  $s = -1$  disclinations located diametrically opposite on the neck

( $\{z = 0; \phi = \pi/2, 3\pi/2\}$  or  $\{x = 0; y = \pm a\}$ ) is

$$\alpha'(x, y)^{(2p)} = -\arctan\left(\frac{y-a}{x}\right) - \arctan\left(\frac{y+a}{x}\right) \quad (\text{B.4})$$

In terms of  $\{\phi, z\}$ ,  $\alpha$ -field is given by

$$\alpha(\phi, z) = \arctan(e^{-z} \sec \phi - \tan \phi) - \arctan(e^{-z} \sec \phi + \tan \phi) \quad (\text{B.5})$$

which has different expression from the  $\alpha$ -field obtained by intersection method (Eq. 3.2). However, the main difference is in deformation of the texture. We note that  $\alpha'^{(2p)}$  has more deformation in the texture.

## B.2 Division of total Gaussian curvature

Minimisation of elastic free energy ( $F_{\text{el}}$ ) with respect to the positions  $d_i$  of the wall leads to

$$\frac{dF_{\text{el}}}{dd_i} = K_\alpha(J_1 + J_2) = 0$$

where,

$$\begin{aligned} J_1 &= \frac{dF_{K\mathcal{S}}}{dd_i} \\ &= -\frac{4\pi^2}{n} \sum_{k=1}^n \left[ \int dz \sqrt{g} K(z) \left\{ \frac{d}{dd_i} G(z, d_k) + \frac{d}{dd_i} G(z, -d_k) \right\} \right] \\ &= -\frac{4\pi^2}{n} \int_{-d_i}^{d_i} dz \sqrt{g} K(z). \\ J_2 &= -\frac{1}{2} \frac{dF_{\mathcal{S}\mathcal{S}}}{dd_i} \\ &= -\frac{4\pi^2}{n^2} \sum_{k=1}^n \sum_{l=1}^n \left[ \frac{d}{dd_i} G(d_k, d_l) + \frac{d}{dd_i} G(d_k, -d_l) \right] \\ &= -\frac{4\pi^2}{n^2} (2i - 1). \end{aligned}$$

The minimisation of  $F_{\text{el}}$  implies that  $\int_{-d_i}^{d_i} dz \sqrt{g} K(z) = -(2i - 1)/n$ .

### B.3 Helicoid : Isomorphism to catenoid

Helicoid parametrisation is given by  $\mathbf{R}(\rho, \phi) = \{\rho \cos \phi, \rho \sin \phi, b \phi\}$  where  $-\infty < \rho < \infty$  and  $0 \leq \phi < 2\pi$ . The metric

$$ds^2 = d\rho^2 + (b^2 + \rho^2) d\phi^2 \quad (\text{B.6})$$

As we mentioned earlier, catenoid and helicoid belong to the same associate family of minimal surfaces and they are isometric to each other. By definition, two surfaces  $S$  and  $S^*$  are isometric to each other if there exists a mapping  $\mathbf{u}$  such that the coefficients of metric tensors of  $S$  and  $S^*$  are the same. i.e.,  $g_{\mu\nu}^*(\mathbf{u}) = g_{\mu\nu}(\mathbf{u})$ . In other words, one can bend  $S^*$  into a portion of  $S$  without stretching such that distance between any two points on the surface is preserved. It is important to note that isometric mapping is automatically conformal.

The transformation

$$\begin{aligned} b &\rightarrow a \\ \rho &\rightarrow a \sinh\left(\frac{z}{a}\right) \\ \phi &\rightarrow \phi \end{aligned} \quad (\text{B.7})$$

is locally isometric and maps a helicoid of one pitch length to catenoid. The parametrisation and metric of helicoid after the transformation is

$$\begin{aligned} \mathbf{R}(\phi, z) &= \{ a \sinh(z/a) \cos \phi, a \sinh(z/a) \sin \phi, a\phi \} \\ ds^2 &= \cosh^2(z/a) (dz^2 + a^2 d\phi^2) \end{aligned} \quad (\text{B.8})$$

With the new parametrisation, the components of the metric tensor are  $g_{\phi\phi} = a^2 \cosh^2(z/a)$ ,  $g_{zz} = \cosh^2(z/a)$ ,  $g_{\phi z} = g_{z\phi} = 0$  and the determinant of metric tensor  $g = a^2 \cosh^4(z/a)$ . The Gaussian and mean curvature of the catenoid, respectively, are  $K = -1/a^2 \operatorname{sech}^2(z/a)$  and  $H = 0$ . Note that they are exactly same as catenoid.



# Bibliography

- [1] D. Nelson and L. Peliti. “Fluctuations in membranes with crystalline and hexatic order”. In: *Journal de physique* 48.7 (1987), pp. 1085–1092.
- [2] M. W. Deem and D. R. Nelson. “Free energies of isolated five- and sevenfold disclinations in hexatic membranes”. In: *Physical Review E* 53.3 (1996), p. 2551.
- [3] P. M. Chaikin, T. C. Lubensky, and T. A. Witten. *Principles of condensed matter physics*. Vol. 10. Cambridge university press Cambridge, 1995.
- [4] B. Lotz and S. Z. Cheng. “A critical assessment of unbalanced surface stresses as the mechanical origin of twisting and scrolling of polymer crystals”. In: *Polymer* 46.3 (2005), pp. 577–610.
- [5] J. K. Alageshan, Y. Hatwalne, and M. Muthukumar. “Stability of the sectored morphology of polymer crystallites”. In: *Physical Review E* 94.3 (2016), p. 032506.
- [6] T. Lubensky. “Soft condensed matter physics”. In: *Solid State Communications* 102.2-3 (1997), pp. 187–197.
- [7] R. A. L. Jones, R. G. Jones, R. A. Jones, R. Jones, et al. *Soft condensed matter*. Vol. 6. Oxford University Press, 2002.
- [8] M. Doi. *Soft matter physics*. Oxford University Press, 2013.
- [9] P.-G. De Gennes and J. Prost. *The physics of liquid crystals*. Vol. 83. Oxford university press, 1993.
- [10] M. Kleman and O. D. Lavrentovich. *Soft matter physics: an introduction*. Springer Science & Business Media, 2007.
- [11] S. Ghosh, A. Ray, and N. Pramanik. “Self-assembly of surfactants: An overview on general aspects of amphiphiles”. In: *Biophysical Chemistry* 265 (2020), p. 106429. ISSN: 0301-4622. DOI: <https://doi.org/10.1016/j.bpc.2020.106429>. URL: <https://www.sciencedirect.com/science/article/pii/S030146222030137X>.

- 
- [12] R. Nagarajan. *Self-assembly: from surfactants to nanoparticles*. John Wiley & Sons, 2019.
- [13] J. P. Lagerwall and F. Giesselmann. “Current topics in smectic liquid crystal research”. In: *ChemPhysChem* 7.1 (2006), pp. 20–45.
- [14] B. Tenchov. “On the reversibility of the phase transitions in lipid-water systems”. In: *Chemistry and physics of lipids* 57.2-3 (1991), pp. 165–177.
- [15] M. Warner and E. Terentjev. *Liquid Crystal Elastomers*. Vol. 120. Oct. 2003. ISBN: 9780198527671.
- [16] J. Park, T. Lubensky, and F. MacKintosh. “N-atic order and continuous shape changes of deformable surfaces of genus zero”. In: *EPL (Europhysics Letters)* 20.3 (1992), p. 279.
- [17] M. Kleman. “Defects in liquid crystals”. In: *Reports on Progress in Physics* 52.5 (May 1989), pp. 555–654. DOI: [10.1088/0034-4885/52/5/002](https://doi.org/10.1088/0034-4885/52/5/002). URL: <https://doi.org/10.1088/0034-4885/52/5/002>.
- [18] L. D. Landau, E. M. Lifšic, E. M. Lifshitz, A. M. Kosevich, and L. P. Pitaevskii. *Theory of elasticity: volume 7*. Vol. 7. Elsevier, 1986.
- [19] M. Bowick and L. Giomi. “Two-Dimensional Matter: Order, Curvature and Defects”. In: *Adv. Phys.* 58 (Dec. 2008). DOI: [10.1080/00018730903043166](https://doi.org/10.1080/00018730903043166).
- [20] M. P. Do Carmo. *Differential geometry of curves and surfaces: revised and updated second edition*. Courier Dover Publications, 2016.
- [21] D. J. Struik. *Lectures on classical differential geometry*. Courier Corporation, 1961.
- [22] E. Kreyszig. “Differential geometry”. In: *Differential Geometry*. University of Toronto Press, 2019.
- [23] M. Deserno. *Notes on differential geometry*. 2004.
- [24] D. R. Nelson. “Order, frustration, and defects in liquids and glasses”. In: *Physical review B* 28.10 (1983), p. 5515.
- [25] R. Cooke and V. Arnold. *Ordinary Differential Equations*. Springer Textbook. Springer Berlin Heidelberg, 1992. ISBN: 9783540548133. URL: <https://books.google.co.in/books?id=JUoyq1W7PZgC>.
- [26] D. Nelson, T. Piran, and S. Weinberg. *Statistical mechanics of membranes and surfaces*. World Scientific, 2004.
- [27] H. S. Seung and D. R. Nelson. “Defects in flexible membranes with crystalline order”. In: *Phys. Rev. A* 38 (2 July 1988), pp. 1005–1018. DOI:

- [10.1103/PhysRevA.38.1005](https://doi.org/10.1103/PhysRevA.38.1005). URL: <https://link.aps.org/doi/10.1103/PhysRevA.38.1005>.
- [28] W. Helfrich. “Elastic properties of lipid bilayers: theory and possible experiments”. In: *Zeitschrift für Naturforschung c* 28.11-12 (1973), pp. 693–703.
- [29] V. Vitelli and D. R. Nelson. “Nematic textures in spherical shells”. In: *Physical Review E* 74.2 (2006), p. 021711.
- [30] B. F. Schutz and D. B. F. Schutz. *Geometrical methods of mathematical physics*. Cambridge university press, 1980.
- [31] R. Capovilla, J. Guven, and J. Santiago. “Lipid membranes with an edge”. In: *Physical Review E* 66.2 (2002), p. 021607.
- [32] J. K. Alageshan, B. Chakrabarti, and Y. Hatwalne. “Equilibrium of fluid membranes endowed with orientational order”. In: *Physical Review E* 95.4 (2017), p. 042806.
- [33] T. Lubensky and J. Prost. “Orientational order and vesicle shape”. In: *Journal de Physique II* 2.3 (1992), pp. 371–382.
- [34] D. R. Nelson. “Toward a tetravalent chemistry of colloids”. In: *Nano Letters* 2.10 (2002), pp. 1125–1129.
- [35] G. A. DeVries, M. Brunnbauer, Y. Hu, A. M. Jackson, B. Long, B. T. Neltner, O. Uzun, B. H. Wunsch, and F. Stellacci. “Divalent metal nanoparticles”. In: *Science* 315.5810 (2007), pp. 358–361.
- [36] T. Lopez-Leon, V. Koning, K. Devaiah, V. Vitelli, and A. Fernandez-Nieves. “Frustrated nematic order in spherical geometries”. In: *Nature Physics* 7.5 (2011), pp. 391–394.
- [37] H. Shin, M. J. Bowick, and X. Xing. “Topological defects in spherical nematics”. In: *Physical review letters* 101.3 (2008), p. 037802.
- [38] X. Xing, H. Shin, M. J. Bowick, Z. Yao, L. Jia, and M.-H. Li. “Morphology of nematic and smectic vesicles”. In: *Proceedings of the National Academy of Sciences* 109.14 (2012), pp. 5202–5206.
- [39] L. S. Hirst, A. Ossowski, M. Fraser, J. Geng, J. V. Selinger, and R. L. Selinger. “Morphology transition in lipid vesicles due to in-plane order and topological defects”. In: *Proceedings of the National Academy of Sciences* 110.9 (2013), pp. 3242–3247.
- [40] O. Manyuhina and M. Bowick. “Forming a cube from a sphere with tetratic order”. In: *Physical review letters* 114.11 (2015), p. 117801.

- [41] P. Cladis and M. Kleman. “Non-singular disclinations of strength  $S=+1$  in nematics”. In: *Journal de Physique* 33.5-6 (1972), pp. 591–598.
- [42] R. B. Meyer. “On the existence of even indexed disclinations in nematic liquid crystals”. In: *The Philosophical Magazine: A Journal of Theoretical Experimental and Applied Physics* 27.2 (1973), pp. 405–424. DOI: [10.1080/14786437308227417](https://doi.org/10.1080/14786437308227417). eprint: <https://doi.org/10.1080/14786437308227417>. URL: <https://doi.org/10.1080/14786437308227417>.
- [43] C. Saichand, J. K. Alageshan, A. Roy, and Y. Hatwalne. “Stability of topological wall defects on spheres with n-atic order”. In: *Physical Review Research* 2.2 (2020), p. 023215.
- [44] P.-G. De Gennes and P. A. Pincus. *Superconductivity of metals and alloys*. CRC Press, 2018.
- [45] L. Landau and E. Lifshitz. *Statistical Physics: Volume 5*. v. 5. Elsevier Science, 2013. ISBN: 9780080570464. URL: <https://books.google.co.in/books?id=VzgJN-XPTRsC>.
- [46] J.-P. Brasselet, J. Seade, and T. Suwa. *Vector fields on singular varieties*. Vol. 1987. Springer Science & Business Media, 2009.
- [47] L. Mesarec, W. Gózdź, A. Iglič, V. Kralj-Iglič, E. G. Virga, and S. Kralj. “Normal red blood cells’ shape stabilized by membrane’s in-plane ordering”. In: *Scientific reports* 9.1 (2019), pp. 1–11.
- [48] W. Luedtke and U. Landman. “Structure, dynamics, and thermodynamics of passivated gold nanocrystallites and their assemblies”. In: *The Journal of Physical Chemistry* 100.32 (1996), pp. 13323–13329.
- [49] B. L. Mbanda, G. M. Grason, and C. D. Santangelo. “Frustrated Order on Extrinsic Geometries”. In: *Phys. Rev. Lett.* 108 (1 Jan. 2012), p. 017801. DOI: [10.1103/PhysRevLett.108.017801](https://doi.org/10.1103/PhysRevLett.108.017801). URL: <https://link.aps.org/doi/10.1103/PhysRevLett.108.017801>.
- [50] M. Muthukumar. “Shifting Paradigms in Polymer Crystallization”. In: *Progress in Understanding of Polymer Crystallization*. Ed. by G. Reiter and G. R. Strobl. Berlin, Heidelberg: Springer Berlin Heidelberg, 2007, pp. 1–18. ISBN: 978-3-540-47307-7. DOI: [10.1007/3-540-47307-6\\_1](https://doi.org/10.1007/3-540-47307-6_1). URL: [https://doi.org/10.1007/3-540-47307-6\\_1](https://doi.org/10.1007/3-540-47307-6_1).
- [51] P. H. Geil. *Polymer single crystals*. Vol. 5. Krieger Publishing Company, 1963.

- [52] J. C. Wittmann and B. Lotz. “Polymer decoration: The orientation of polymer folds as revealed by the crystallization of polymer vapors”. In: *Journal of Polymer Science: Polymer Physics Edition* 23.1 (1985), pp. 205–226. DOI: <https://doi.org/10.1002/pol.1985.180230119>. eprint: <https://onlinelibrary.wiley.com/doi/pdf/10.1002/pol.1985.180230119>. URL: <https://onlinelibrary.wiley.com/doi/abs/10.1002/pol.1985.180230119>.
- [53] G. W. Greenwood, A. L. Greer, D. M. Herlach, K. F. Kelton, and M. Muthukumar. “Molecular modelling of nucleation in polymers”. In: *Philosophical Transactions of the Royal Society of London. Series A: Mathematical, Physical and Engineering Sciences* 361.1804 (2003), pp. 539–556. DOI: [10.1098/rsta.2002.1149](https://doi.org/10.1098/rsta.2002.1149). eprint: <https://royalsocietypublishing.org/doi/pdf/10.1098/rsta.2002.1149>. URL: <https://royalsocietypublishing.org/doi/abs/10.1098/rsta.2002.1149>.
- [54] M. Muthukumar. “Modeling Polymer Crystallization”. In: *Interphases and Mesophases in Polymer Crystallization III*. Ed. by G. Allegra. Berlin, Heidelberg: Springer Berlin Heidelberg, 2005, pp. 241–274. ISBN: 978-3-540-31604-6. DOI: [10.1007/12\\_008](https://doi.org/10.1007/12_008). URL: [https://doi.org/10.1007/12\\_008](https://doi.org/10.1007/12_008).
- [55] A. Keller. “A note on single crystals in polymers: Evidence for a folded chain configuration”. In: *The Philosophical Magazine: A Journal of Theoretical Experimental and Applied Physics* 2.21 (1957), pp. 1171–1175. DOI: [10.1080/14786435708242746](https://doi.org/10.1080/14786435708242746). eprint: <https://doi.org/10.1080/14786435708242746>. URL: <https://doi.org/10.1080/14786435708242746>.
- [56] B. Crist and J. M. Schultz. “Polymer spherulites: A critical review”. In: *Progress in Polymer Science* 56 (2016), pp. 1–63. ISSN: 0079-6700. DOI: <https://doi.org/10.1016/j.progpolymsci.2015.11.006>. URL: <https://www.sciencedirect.com/science/article/pii/S0079670015001288>.
- [57] Y. Hatwalne and M. Muthukumar. “Chiral symmetry breaking in crystals of achiral polymers”. In: *Physical review letters* 105.10 (2010), p. 107801.
- [58] P. Geil. “Nylon single crystals”. In: *Journal of Polymer Science* 44.144 (1960), pp. 449–458.
- [59] D. Bassett, F. Frank, and A. Keller. “Some new habit features in crystals of long chain compounds part IV. the fold surface geometry of monolayer polyethylene crystals and its relevance to fold packing and crystal growth”. In: *Philosophical Magazine* 8.94 (1963), pp. 1753–1787.

- [60] C. Garber and P. Geil. “Polyoxymethylene single crystals. I. The effect of copolymer content on morphology”. In: *Die Makromolekulare Chemie: Macromolecular Chemistry and Physics* 113.1 (1968), pp. 236–245.
- [61] R. M. Briber and F. Khoury. “The morphology of poly (vinylidene fluoride) crystallized from blends of poly (vinylidene fluoride) and poly (ethyl acrylate)”. In: *Journal of Polymer Science Part B: Polymer Physics* 31.10 (1993), pp. 1253–1272.
- [62] A. Rapini and M. Papoular. “Distorsion d’une lamelle nématique sous champ magnétique conditions d’ancrage aux parois”. In: *Le Journal de Physique Colloques* 30.C4 (1969), pp. C4–54.
- [63] D. R. Nelson and B. Halperin. “Solid and fluid phases in smectic layers with tilted molecules”. In: *Physical Review B* 21.11 (1980), p. 5312.
- [64] A. Toda, M. Okamura, M. Hikosaka, and Y. Nakagawa. “AFM observation of polyethylene single crystals: selective handedness of screw dislocations in a chair type”. In: *Polymer* 44.20 (2003), pp. 6135–6138. ISSN: 0032-3861. DOI: [https://doi.org/10.1016/S0032-3861\(03\)00592-5](https://doi.org/10.1016/S0032-3861(03)00592-5). URL: <https://www.sciencedirect.com/science/article/pii/S0032386103005925>.
- [65] C. Carraro and D. R. Nelson. “Grain-boundary buckling and spin-glass models of disorder in membranes”. In: *Physical Review E* 48.4 (1993), p. 3082.
- [66] F. MacKintosh and T. Lubensky. “Orientational order, topology, and vesicle shapes”. In: *Physical review letters* 67.9 (1991), p. 1169.
- [67] C.-M. Chen, T. Lubensky, and F. MacKintosh. “Phase transitions and modulated phases in lipid bilayers”. In: *Physical Review E* 51.1 (1995), p. 504.